THE UNIVERSITY OF CHICAGO

METAL MAPPING WITH X-RAY FLUORESCENCE EMISSION TOMOGRAPHY

A DISSERTATION SUBMITTED TO
THE FACULTY OF THE DIVISION OF THE BIOLOGICAL SCIENCES
AND THE PRITZKER SCHOOL OF MEDICINE
IN CANDIDACY FOR THE DEGREE OF
DOCTOR OF PHILOSOPHY

COMMITTEE ON MEDICAL PHYSICS

BY
HADLEY ANNA DEBROSSE

CHICAGO, ILLINOIS
JUNE 2024

To my husband, Joe.

TABLE OF CONTENTS

LIST OF FIGURES

LIST OF TABLES

LIST OF MATHEMATICAL SYMBOLS

p_{ij}	Number of fluorescent photons from object voxel i measured at detector j
p_m	Detected fluorescent photons, after re-indexing i and detector pixel j index into one $m = iN + j$
d_1	Distance from beam to slit in xy-plane
d_2	Distance from slit to detector in xy-plane
R_{ij}	Distance of object voxel i to detector pixel j
I_0	Initial pencil beam photon flux, in $\frac{1}{s\,cm^2}$
A_0	Pencil beam cross-sectional area
D_0	Detector pixel area
d_0	Length of axial beam segment that maps to one detector pixel
s	$\frac{\tau}{\rho}(E_B)\xi_K\omega_K\nu_K$
t	Pencil beam exposure time
f_i or f_m	Metal density, in $\frac{g}{cm^3}$
μ_k	Linear attenuation coefficient. $\mu_k^{(n)}$ is the attenuation estimation for the k^{th} voxel on the n^{th} iteration
$\boldsymbol{\mu}^{(E_F)}$	Discrete attenuation map vector containing attenuation coefficients $\mu_k^{(E_F)}$ at the energy of fluorescence emission
$\boldsymbol{\mu}^{(E_B)}$	Discrete attenuation map vector containing attenuation coefficients $\mu_k^{(E_B)}$ at the energy of the pencil beam
L_{mk}	Intersection lengths from the intersection of a line traveling from object pixel i to detector pixel j with the attenuation map μ_k, after consolidating detector index j and object pixel i, $m = iN + j$
β	Scalar roughness parameter

c_{rk} or c_{kr}	Elements of penalty matrix C, discussed further in [3]. This C only affects the attenuation map estimation
w_r	Weights for the difference between neighboring pixels in the roughness penalty. For vertical and horizontal neighbors, $w_r = 1$, for diagonal neighbors, $w_r = 1/\sqrt{2}$, and $w_r = 0$ otherwise
$c_m^{(n)}$	$\begin{cases} [-2\frac{h(0)-h(l_m^{(n)})+\dot{h}(l_m^{(n)})l_m^{(n)}}{(l_m^{(n)})^2}]_+ & \text{if } l_m^{(n)} \geq 0, \\ [-\ddot{h}(l_m^{(n)})]_+ & l_m^{(n)} = 0. \end{cases}$ where h, $\dot{h}$ and $\ddot{h}$ are derivatives of the log likelihood, and given below
$l_m^{(n)}$	$\sum_k L_{mk}\mu_k^{(n)}$ is the m^{th} line integral through the attenuation map at the n^{th} iteration
$h(l_m^{(n)})$	$p_m \ln(q_m'' f_m e^{-l_m^{(n)}}) - (q_m'' f_m e^{-l_m^{(n)}})$, is the log likelihood for the m^{th} measurement
$\dot{h}(l_m^{(n)})$	$q_m'' f_m e^{-l_m^{(n)}} - p_m$ is the first derivative of the log likelihood
$\ddot{h}(l_m^{(n)})$	$-q_m'' f_m e^{-l_m^{(n)}}$ is the second derivative of the log likelihood
c_r	$\sum_k c_{kr}$
L_m	$\sum_k L_{mk}$
N_Y	Number of object-detector pixel pairs
K	$N\times$ Number of neighbors considered in the penalty matrix C
A	Discrete XFET linearized forward model
$\boldsymbol{v}_r^f$	Metal component of the r^{th} right singular vector of A
$\boldsymbol{v}_r^\mu$	Attenuation component of the r^{th} right singular vector of A
H	Hessian matrix
F	Fisher information matrix
$\boldsymbol{h}_r^f$	Metal component of the r^{th} eigenvector of F

$\boldsymbol{h}_r^{\mu}$	Metal component of the r^{th} eigenvector of F
I_b	Number of photons delivered in each XFET beam location
w_{iso}	Width of a CT detector element projected to the isocenter
γ_{fan}	CT fan angle
SDD	Source-to-detector distance in CT simulations
SID	Source-to-isocenter distance in CT simulations
w_{fan}	Arc length of CT fan beam at the SDD
w	Width of a CT detector element

ACKNOWLEDGMENTS

The work presented in this dissertation would not have been possible without my advisor, Dr. Patrick La Rivière, who was a source of tireless support and invaluable guidance throughout the course of this project. I extend my upmost gratitude for his kind and concerned mentorship. I am grateful for Drs. Xiaochuan Pan, Emil Sidky, Ling Jian Meng, and Chin-Tu Chen for their time serving as members of my thesis committee.

I also thank the faculty and staff of the Graduate Program in Medical Physics that have supported my learning and professional development at the University of Chicago, including Drs. Zheng Feng Lu, Ingrid Reiser and Kevin Little. I am especially grateful for Dr. Emily Marshall for being an excellent friend and mentor. Dr. Lili Gonzalez, Chun Wai Chan, Julie Hlavaty, and Elena Rizzo have provided critical administrative and technical support.

Certain friends and colleagues deserve recognition for their assistance with my research, including Gia Jadick, Dr. Talon Chandler, and Tabitha Welch. I am also grateful for my cohort of six—Linnea Kremer, Mena Shenouda, Julian Bertini, Dr. Mira Liu, and Dr. Natalie Baughan—for their vital advice and camaraderie. I also extend thanks to friends Geneva Schlafly, Daniela Olivera Velarde, Lucas Berens, Christopher Valdes, Baiyang Dai, Joren Husic, Dr. Lindsay Douglas, Dr. Scott Trinkle, and Dr. Inna Gertsenshteyn, among others.

My immediate and extended family have been a consistent source of support. I would especially like to thank *"my parents and theirs,"* as my father once wrote. My mother, Colleen, has provided much emotional support and practical advice. My father, Howard, has motivated scientific inquiry since the beginning and has been a source of much inspiration for me. Greg has been a loving brother and curious friend through every phone call.

Above all, I thank my husband, Joe. Without him, this feat would have been much more difficult. Thank you for always standing by my side.

This work was supported by the NIH under grant number R01EB026300, the National Cancer Institute of the NIH under award number F31CA275324, the National Science Foundation Graduate Research Fellowship under grant number 2140001, and the AAPM/RSNA Graduate Fellowship. Partial funding for this work was provided by the NIH S10-OD025081, S10-RR021039, and P30-CA14599 awards.

ABSTRACT

Among other metals, gold nanoparticles (GNPs) play an important role in emerging cancer therapies. The development, safety, and efficacy of these therapies is contingent on the ability to accurately map and quantify GNPs. However, current metal-mapping modalities cannot simultaneously provide the sensitivity and tissue penetration depth necessary to image relevant metal concentrations *in vivo*. For clinical translation, these cancer therapies require a highly sensitive metal-mapping imaging modality that can image GNPs *in vivo* at relevant concentrations and depths.

This dissertation presents an optimized x-ray fluorescence emission tomography (XFET) system and novel joint image reconstruction algorithm to image trace gold for applications in these therapies. XFET is an emerging imaging modality that relies on inducing and detecting x-ray fluorescence to recover the spatial distribution and quantify the density of metal in objects. XFET has numerous advantages over conventional imaging modalities: most notably, its imaging geometry does not require tomographic image reconstruction that amplifies noise, and it does not require the full sinogram associated with conventional tomographic image reconstruction methods. Consequently, XFET's capabilities approach the sensitivity and tissue penetration depth required to map metals at concentrations and conditions used in clinical and *in vivo* studies. In light of these advantages, this dissertation improves and demonstrates XFET capabilities and discusses implications for clinical translation.

XFET's imaging mechanism is distinct from other modalities: it not only allows for direct metal measurement, but also allows for joint estimation of the attenuation map that would otherwise need to be obtained with a radiation-dose-delivering computed tomography (CT) scan. In the first chapter, we develop a novel joint algorithm to estimate both metal and attenuation maps from emission data alone and show that it outperforms a conventional approach based on linearization. We successfully extend this novel algorithm to the case of an unknown beam attenuation map, demonstrating an accurate joint reconstruction of metal

and attenuation maps from emission data alone without prior attenuation knowledge.

Image geometry optimization, most notably detector placement, is necessary to obtain accurate metal and attenuation images in XFET. In the second chapter, we use mathematical tools to investigate how detector arrangement affects image quality and joint estimation. We use the previously developed algorithm to reconstruct metal and attenuation maps using simulated datasets acquired with various detector arrangements. We demonstrate that two parallel detectors provide greatest accuracy but at the cost of reduced isotropic spatial resolution in the attenuation map, informing about optimal detector placement in an imaging task where a full-ring geometry is not feasible.

Finally, the third chapter demonstrates proof of benefit by comparing simulations of XFET to CT in the task of trace metal mapping. We performed photon-counting CT, energy-integrating CT, and Monte Carlo XFET simulations on two phantoms: the first contained a range of clinically relevant gold concentrations at varied depths in soft tissue, and the second was a realistic numerical mouse phantom. We show that for superficial depths (< 3 cm), XFET outperforms CT for imaging gold concentrations as low as 0.5% by weight. XFET's detection limit is further improved (down to 0.05%) with additional dose and with utilization of XFET's unique partial-field imaging capability. We discuss the advantages and limitations of XFET for more informed translation into preclinical and clinical use.

Ultimately, the results of this dissertation improve XFET's current capabilities and provide the information necessary to predict XFET's ability to map therapeutic GNPs *in vivo* for informed development, safer treatment, and fewer side effects of cancer therapies.

CHAPTER 1

INTRODUCTION

This dissertation presents a nascent imaging modality: x-ray fluorescence emission tomography (XFET). XFET is an x-ray-fluorescence-based imaging modality that can image the spatial distribution of low concentrations of metals within objects. Current approaches to metal mapping for certain preclinical and clinical applications are limited by sensitivity and practical constraints. XFET addresses these limitations with novel geometries and hardware, that together, have desirable implications for imaging depth and sensitivity.

This dissertation focuses on improving XFET image quality and exploring XFET's limitations and advantages within eventual preclinical and clinical spaces. Specifically, we develop XFET image reconstruction algorithms, discuss effects of geometric parameters on image quality, and demonstrate XFET's clinical feasibility compared to conventional imaging modalities. The results of this dissertation provide information necessary to predict XFET's capacity in clinical scenarios and pave the way for XFET to be used as an imaging system capable of mapping therapeutic metal nanoparticles.

In this chapter, we begin by motivating the need for metal mapping by discussing applications of metal nanoparticles in emerging preclinical and clinical therapies. We then discuss the advantages and limitations of existing approaches to metal mapping, including x-ray fluorescence computed tomography (XFCT): a modality closely related to XFET. We then introduce XFET: its geometry, imaging acquisition methods, advantages, limitations, and potential applications. Finally, we outline the remainder of this dissertation, which focuses on improving, optimizing, and demonstrating XFET imaging.

1.1 The emerging role of metal in the treatment of disease

Metals and metal-based drugs have historically played a significant role in medicine as therapeutic, diagnostic, and theranostic tools: for example, platinum-based chemotherapy agents [4], yttrium-based particles for internal radiation treatment of liver cancer [5], and iodine contrast for angiography [6]. Metal nanoparticles are increasingly being used for their therapeutic potential, and are proving especially effective in novel treatments of cancer. Among these metals, gold nanoparticles (GNPs) have particular promise due to their biocompatibility, functionalization, radiation-enhancement and photothermal properties [7][8]. This section contains descriptions of select emerging cancer therapies that incorporate gold and other metal nanoparticles.

1.1.1 Radiation therapy (RT) enhancement

GNPs have long been investigated for their radiation-enhancement properties; when GNPs are contained in a tumor, they increase the therapeutic ratio of external beam RT by enhancing the effect of radiation on cancer cells [8, 9, 10, 11]. This effect is due to GNPs and other metals of high atomic number having high absorption coefficients, namely large photoelectric cross sections at low kilovoltage (kV) x-ray energies [8, 12]. This large photoelectric cross section with high probability of secondary electrons and free radical production causes significantly increased absorbed radiation dose when using kV x-rays [13, 14, 15]. This dose enhancement has been estimated to be greater than 200% for certain gold concentrations and external beam energies [16, 17].

For megavoltage (MV) beams typically used for RT, the dominant interaction with GNPs and other metals is Compton scattering. Yet, the presence of GNPs under MV beams still increases RT sensitivity, with or without significant dose enhancement [18, 19, 20]. Dose enhancement does not necessarily predict biological effect: GNP-related radiosensitivity enhancement has been attributed to various physical, chemical, and biological mechanisms,

including mechanisms that increase oxidative stress [11, 18, 21, 22, 23]. Additionally, there is general lack of agreement between predicted degree of sensitivity enhancement and measured data, further suggesting that GNPs cause radiosensitization through biologically driven processes that cannot be predicted with beam energy and GNP concentration alone [18]. The radiosensitization by GNPs remains an active preclinical research area [23].

Regardless of the mechanism by which they increase radiosensitization, GNPs and related molecules have consistently shown *in vitro* and *in vivo* success for RT enhancement. *In vitro*, GNPs or modified GNPs enhance RT for many cell types, including MCF7 and MDA-MB-231 breast cancer cells, HeLa cells, oral epidermoid carcinoma (KB), SK-OV-3 ovarian cancer, and DU-145 prostate carcinoma [19, 20, 24, 25, 26, 27]. Studies *in vivo* also show effective radiation enhancement in mouse models that results in increased survival and significant tumor growth delay for a variety of cancers [28, 29, 30, 31, 32, 33]. This effect occurs even without direct tumor targeting of the GNPs: GNPs have enhanced permeability and retention (EPR), that, when combined with the leaky vasculature and impaired lymphatic clearance of tumors, results in preferential deposition at tumor sites [8, 34]. Beyond *in vitro* and *in vivo* studies, treatment planning simulations demonstrate the effectiveness of GNP-mediated radiation therapy in human cancers [35].

Finally, other high-Z metals besides gold have also been investigated and show promise for RT enhancement. These metals include bismuth, silver, tungsten, hafnium, and platinum [36, 37, 38]; hafnium has already been used to demonstrate the feasibility of RT-enhancement in a clinical study of pancreatic ductal adenocarcinoma [39].

1.1.2 Photothermal ablation therapy

Another advantage of gold is its tunable optical properties and resulting applications in photothermal ablation (PTA) therapy [40, 41]. PTA (also termed PTT or PPTT) involves targeting a tumor with GNPs or other selective materials, and thermally ablating the lesion

with near-infrared (NIR) light illumination [7, 10, 40, 42, 43, 44]. Thermal ablation occurs because gold is a plasmonic material that strongly absorbs NIR light, which results in the production of therapeutic doses of heat [45]. Gold is an ideal material for PTA for two main reasons. First, the NIR wavelength that gold naturally absorbs and converts to heat is desirable for this application, because this wavelength range has relative biological tissue transparency [46]. Second, GNPs have tunable optical properties: the wavelength that GNPs preferentially absorbs is tunable with the geometry and size of the nanoparticle, and GNPs are easily manufactured in various shapes and sizes [41].

The first recognized *in vivo* study to perform NIR PTA injected solid tumors with silica-gold nanoshells and exposed them to NIR light. These tumors reached temperatures associated with irreversible tissue damage within 4-6 minutes; and there was no damage to control tissue [40]. Several *in vivo* and *in vitro* studies have confirmed the feasibility of gold-mediated PTA in various cell lines and animal models (mouse, feline, and canine), with desirable ablation being achieved in 10 minutes or less [47, 48, 49, 50, 51, 52, 53]. This promise has extended to clinical trials, including one that used gold-silica nanoshells to photothermally ablate prostate lesions with success in 94% of patients without serious complications [44].

The success of PTA depends on the heat generated in a lesion, which is dependent on gold uptake and distribution [10]. Nanoparticle shape and size impacts this distribution, and affects the efficiency of heat production [54, 55]. Tumor uptake can also be improved by bonding the GNPs to various biologically useful molecules, including polyethylene glycol (PEG) and macrophages [42, 50, 51, 56]. However, these factors all impact the biodistribution of gold particles [57, 58, 59]; biodistribution and toxicity must be studied for each GNP variation to ensure safe and effective treatment with no long term negative health effects [7].

Even though the NIR wavelength range experiences relative biological tissue transparency, the light penetration is limited to depths up to a few centimeters [59]. Therefore, PTA is mostly clinically limited to superficial solid tumors, such as head and neck, breast, and

melanoma [7].

1.1.3 Photodynamic therapy

Photodynamic therapy (PDT) is an emerging, effective treatment modality used for a range of diseases [59, 60]. PDT is similar to PTA in that a photosensitizer (PS) absorbs a specific wavelength. Rather than converting light to heat, the PS can transform into an excited state which undergoes photochemical reactions with molecular oxygen to produce reactive oxygen species (ROS). These ROS induce oxidative stress which contributes to cell killing [59, 60, 61]. PDT can also be particularly effective when combined with other therapies [61]. One limitation of PDT is that PSs have a non-specific biodistribution, which can make tumor targeting difficult and can lead to unwanted side effects [60, 61]. GNPs and GNPs modified with certain molecules are suggested to address this limitation with drug delivery: acting as PS carriers, they increase the stability and improve the and non-specific biodistribution of PSs [60, 61, 62].

The wavelength of light absorbed in PDT, 650 - 850 nm, has low penetration depth in tissue [61, 63]. Thus, PDT is often used for superficial skin disease [60, 64]. However, some groups have circumvented this limitation by producing light adjacent to PSs with nanoparticle scintillators, which are activated by an external x-ray beam [65]. This approach, called x-ray-induced PDT (X-PDT) provides superior tissue penetration and therefore expands the range of clinical PDT applications beyond superficial lesions. Nanoparticle scintillators and photosensitizers investigated for X-PDT and PDT include metals such as titanium, copper, bismuth, gold, and platinum [66, 67, 68, 69]. Metal-organic frameworks are particularly useful in that they incorporate scintillators and photosensitizers in close proximity [70]. X-PDT that utilizes metal complexes or metal-based hybrid structures to generate oxygen species via energy transfer without fluorescence is often referred to as radiodynamic therapy (RDT) [71]; metal provides additional radiosensitization that also serves to damage DNA during

radiation exposure [72]. In this sense, X-PDT is a combination therapy of RT and PDT [65].

In vivo X-PDT has recently been tested in mouse models and has been shown to improve treatment efficacy and provide significant tumor reduction when compared to x-ray treatment alone [66, 68, 72]. While there is clinical promise in X-PDT, it is still in development. There is a wide range of scintillator nanoparticles that are being investigated for PDT for their appealing optical qualities. These materials require further study into their toxicity, tumor selectivity, and biocompatibility before clinical feasibility can be demonstrated [60, 65, 71].

1.1.4 Drug delivery

Drug delivery as a cancer treatment modality offers tumor targeting, which is specifically advantageous over conventional, systematic chemotherapy. During drug delivery, anticancer drugs will distribute and collect in a target via a carrier molecule. Metal nanoparticles have specific qualities that harness potential applications as drug delivery carriers for targeted delivery: increased stability and half life of drug carriers in circulation and small size for increased permeability in tissue [73]. These metals include gold, silver, platinum, zinc, and titanium, among others [73]. In particular, GNPs show promise as drug delivery systems due to their ease of surface functionalization, biocompatibility, hydrophilicity, and low toxicity [73, 74, 75, 76]. Many studies have used GNPs or related molecules for targeting anticancer drug delivery *in vitro*, including in human breast, lung, and colon cancer cell lines [74, 77, 78]. *In vivo* drug targeting with gold has also been demonstrated, with little to no accumulation of the drug in healthy organs of animals [79]. These studies have extended to clinical trials, where the potential for GNPs for drug delivery and tumor targeting is being investigated and demonstrating preliminary promise [80, 81]. As with PDT and any other injection of gold or metal nanoparticles, biodistribution, potential toxicity, and pharmacokinetics must be investigated before clinical translation [74, 76, 82].

1.2 Clinical and preclinical metal mapping

The ability to accurately map and quantify metal nanoparticles in objects is critical for many of the above emerging cancer therapies. Specifically, there are two ways in which the above therapies would benefit from quantitative metal imaging: image guidance during treatment, and *in vivo* metal biodistribution measurements during research and development.

First, in all of the above therapies, metal will result in enhanced dose to the region it occupies; therefore, the ability to image metals during or immediately before treatment is conducive to treatment efficacy and safety. For example, successful treatment with X-PDT depends on intratumoral and intracellular nanoparticle distribution; this distribution is heterogeneous and therefore has potential undesirable impacts on cytotoxicity [65, 83]. Mechanisms for tumor targeting in X-PDT is similar to the targeting methods used in RT-enhancement, drug delivery, and PTA: for example, surface functionalization with PEG [51, 58, 84, 85, 86]. Therefore, homogeneous intratumoral nanoparticle distribution is not guaranteed for these therapies. Additionally, confirmation of the appropriate intratumoral nanoparticle (NP) concentration is important prior to treatment, as different nanoparticle formulations and sizes show varying tumor uptake and renal clearances [83, 87]. With various NP sizes and surface properties being investigated, there is a strong need for imaging methods that would allow for real-time *in vivo* quantification of metal nanoparticles [71, 88].

Second, in the development of these emerging therapies, particularly in preclinical and *in vivo* stages, measuring pharmacokinetic properties is crucial to understanding toxicity and effects of the metal particles. Although gold is acutely non-toxic, its incomplete excretion from the body and its accumulation in healthy organs such as the liver and spleen is of notable concern, as long-term effects and toxicity are still being explored [81, 89]. As with any new drug, the *in vivo* pharmacokinetics must be studied in depth before regulatory approval, to assess absorption, biodistribution, metabolism, and the elimination process [82]. Therefore, there is a strong need for quantitative preclinical and *in vivo* metal imaging.

1.2.1 Relevant metal concentrations and depths

For the imaging applications discussed in Section 1.2, certain metal concentrations and imaging depths hold relevance. Both PTA and PDT suffer from low penetration depth of light and are therefore limited to treating superficial disease, up to few centimeters in depth [7, 59, 61, 63, 65, 67]. X-PDT uses x-rays as an initial source, and therefore does not suffer from this depth limitation [65]. Similarly, metal-mediated RT and drug delivery do not have depth limitations. However, metal-mediated RT and drug delivery are often used for superficial treatments. Metal-mediated RT, for example, is expected to be most effective for superficial tumors [10]. GNPs are studied for skin disease drug delivery because they increase the skin permeability of topical drugs [90, 91]. Evidently, every therapy in Section 1.1 has applications in the treatment of superficial lesions.

There is high variance in the concentrations of metal that are used in these emerging therapies, and some lack of consistent information about intratumoral concentration, especially for PDT and drug delivery studies with gold. In particular, studies about drug delivery using GNP carriers suffer from a lack of standardization. Differences in surface molecules, anticancer drugs, and particle sizes and shapes has led to a wide variety of gold concentrations across literature biodistribution studies [92]. However for metal-mediated RT enhancement and PTA, there is some consistency in reported intratumoral gold concentration.

The effective concentration of GNPs needed for significant tumor growth delay using RT enhancement is between 0.250 μg and $\sim$74 mg of gold per g of tumor (which corresponds to concentrations as little as 0.000025% to as much as 7.4% by weight) [23]. Generally however, RT enhancement has been studied at relatively high intratumoral concentrations of gold: between 0.7% and 3% by weight gold (which corresponds to between 7 mg and 30 mg of Au per g of tumor) [17, 30]. For one *in vivo* mouse model, 1.5% gold by weight corresponded to a dose enhancement factor of 3.4 [30]. While it is important to maintain adequate intratumoral gold concentrations to achieve RT enhancement, minimal dose to

background tissue is required; one study showed that 0.2% gold by weight (2 mg/g) outside the tumor resulted in an undesirable dose enhancement of 30% in the healthy tissue when using 140 kVp treatment beams [17].

In comparison to RT enhancement, PTA requires significantly lower gold concentrations for treatment efficacy, due tumors' greater sensitivity to heat compared to other tissue [93, 94]. Gold doses used for *in vitro* and *in vivo* PTA studies usually range from $\sim$ 0.00004 - 0.08 mg Au/g (up to 0.008% by weight gold) [67, 93]. A pioneering clinical trial studying gold-mediated PTA of prostate cancer measured the median gold concentration in prostate tumors as 0.00828 mg/g (0.0008% by weight, range of measured concentrations: 0.00115 to 0.03312 mg/g), and noted that healthy prostate tissue is known to accumulate nanoparticles at a minimal background concentration of 0.0004 mg /g [44].

In summary, the above gold concentrations used in RT enhancement and PTA studies indicate that the biologically relevant concentration of gold is approximately $\leq$ 1-2% gold by weight [95].

1.2.2 Advantages and limitations of current metal-mapping, non-x-ray-fluorescence-based imaging modalities

To quantify very low concentrations of non-radioactive gold discussed in Section 1.2.1, the "gold standard" modalities include instrumental neutron activation analysis (INAA) and inductively coupled plasma-mass spectrometry (ICP-MS) [92]. Both have good accuracy and benefit from a very low, 0.02-1 ppb detection limit, but are labor and time intensive and cannot perform *in vivo* imaging that is required for image guidance [92]. Although they are used in the preclinical stage for pharmacokinetic studies in animal models, this process requires repeated animal sacrifices at various time points [82, 96]. There is a need for faster determination of NP circulation times to determine NP accumulation in tumors [88]. It would also be advantageous in pharmacokinetic studies to use a mouse as its own control,

which would only be possible with repeated metal measurements *in vivo*.

Image guidance of PTA is often performed using magnetic resonance imaging (MRI) in combination with a magnetic particle that has been embedded into the gold nanoparticle or shell [47, 48]; alternatively, MRI image contrast can obtained from the temperature dependence of proton resonance [40]. However, obtaining MRI images is slow, potentially slower than PTA treatment time which is on the order of a few minutes or less [48, 40]. This slow imaging time also makes MRI prone to motion artifacts. One clinical trial of PTA of prostate cancer with GNPs used MRI-ultrasound fusion for treatment planning, trocar placement, and post-treatment biopsies, but monitored the treatment itself with needle thermocouples to avoid accidental thermal ablation of the rectal wall, urinary sphincter, and urethra [44].

Other image guidance methods also have practical concerns. Optical imaging of gold nanoparticles usually has a limited tissue penetration depth of a few 100 µm [97]. Photoacoustic imaging is a promising modality for imaging GNPs, but has practical limitations such as the direct coupling of the transducer to the body and its inability to image through the lung or air bubbles in the bowel. Its imaging depth of a few centimeters also comes with a tradeoff of limited spatial resolution [98].

Computed tomography (CT) is limited in its ability to live image low concentrations of metal. CT visualizes gold through differences in x-ray attenuation coefficients, but does not provide element-specific information, and can only image gold down to concentrations of 0.5 mg/mL in typical clinical acquisitions [8, 99]. This detection limit is equivalent to 0.05% gold by weight, which is also inadequate for imaging concentrations of gold used in PTA. Spectral photon-counting CT provides material differentiation, but its detection limit for gold is similar to conventional CT [100].

In summary, current imaging modalities have limitations that make imaging the relevant depths and concentrations of GNPs impractical.

1.3 X-ray fluorescence tomography

X-ray fluorescence imaging (XFI) is an emerging class of imaging modalities that is used to image the spatial distribution of trace metals without radioactivity or biochemical alteration. XFI exploits the high-Z nature of metals, specifically the high probability of x-ray induced photoelectric interactions and subsequent x-ray fluorescence emissions. XFI measures these monochromatic fluorescence x-rays, which have energies specific to the metal that emitted them, and can simultaneously image many different metals that may appear indistinguishable in a CT image. Therefore, XFI is best suited for metal mapping. We distinguish between two x-ray-fluorescence-based approaches to metal mapping: x-ray fluorescence computed tomography (XFCT) and x-ray fluorescence emission tomography (XFET).

1.3.1 X-ray fluorescence computed tomography (XFCT)

XFCT is an imaging modality that functionally image metal maps *in vivo*. Conventional XFCT uses a pencil x-ray beam to stimulate characteristic x-ray emissions from metals in materials. These characteristic, or fluorescent, x-rays are detected by a large energy-sensitive, non-imaging detector placed perpendicularly to the sample. In the absence of attenuation, one measurement gives a line integral through the metal density map of the material. XFCT uses first-generation CT acquisition, scanning the pencil beam and rotating the sample at each position to obtain a complete sinogram. This sinogram is used in reconstructing the spatial distribution of metal within the object [101, 102, 103].

XFCT has been used with monochromatic synchrotron radiation as the x-ray source, which benefits from reduced scatter background and high sensitivity [104, 105, 106]. But as synchrotrons are not always available, many groups developed benchtop XFCT with the conventional geometry described above [101, 102, 103]. Conventional benchtop XFCT suffers from many limitations: its sensitivity is fundamentally limited by the interaction cross section of gold, it lacks penetration depth, and forming images requires noise-amplifying to-

mographic image reconstruction. Furthermore, obtaining a full sinogram is time consuming, can limit the depth of metal that can be imaged, and is dose inefficient, which can exclude *in vivo* imaging. These factors all limit XFCT's sensitivity and potential use in biomedical applications.

To address these limitations, several groups have explored various XFCT acquisition methods that can theoretically improve scan time, dose, depth, and sensitivity limits. One "cost-free" way of improving XFCT detection limits is introducing new detector geometries, such as full ring detectors [107, 108], or detectors placed in backscatter positions to minimize scatter contamination [109, 110]. However, there are usually tradeoffs that accompany each acquisition method. For example, imaging time can be reduced and sensitivity improved with new XFCT geometries and acquisition parameters, including cone beams [95, 111, 112, 113, 114], fan or sheet beams [108, 115, 116, 117], and the detection of L-shell fluorescence instead of K-shell fluorescence [110, 115, 118]. The above time and sensitivity advantages become even more apparent when cone beams and fan beams are paired with new apertures, collimators, and pixelated, energy sensitive detectors [95, 108, 117, 119]. Yet, sheet beams are dose-inefficient and have worse sensitivity than pencil beams when directly compared [108, 115]. Detecting L-shell instead of K-shell fluorescence can lead to significant sensitivity improvements via reduced Compton scatter contamination, but is impractical for imaging metals at depths greater than 1 cm because of significant attenuation [110, 111, 116, 118]. Table 1.1 contains sensitivities and imaging doses of several XFCT acquisition methods used to detect GNPs in phantoms. Note that highly sensitive systems have low dose-detection limit products in Table 1.1.

Table 1.1: Summary of studies on K-shell XFCT sensitivity and dose

Reference	**XFCT acquisition parameters**	**Phantom material & diameter**[a]	**GNP detection limit (% by weight)**[b]	**Estimated dose**[c]	**Dose-detection limit product (%-cGy)**
Conventional XFCT					
Kuang et al. 2013 [103]	150 kVp scanning pencil beam, rotating phantom, single-crystal CdTe detector	Water (3.5 cm)	$\sim$ 0.25 % (by visibility)	77 cGy	19.25
Cheong et al. 2010 [101]	110 kVp scanning pencil beam, rotating phantom, single-crystal CdTe detector	PMMA (5 cm, 1.05 cm inserts)	$<$ 1% (by visibility)	201 cGy	$<$201
Cone and fan beam XFCT					
Jones et al. 2012 [112]	105 kVp cone beam, rotating phantom, 2 opposed CdTe detectors, 2 opposed pinhole collimators	PMMA (3 cm, 6 mm inserts)	$<$ 0.5% (by visibility)	204 mGy (3.4 mGy/proj.)	$<$10.2
Jones et al. 2011 [111]	110 kVp cone beam, pair of opposing parallel hole collimators, rotating phantom, 2 opposing energy-sensitive detectors	PMMA (5 cm, 5-10 mm inserts)	0.1% (by visibility)	30 cGy (0.5 cGy/proj.)	3
Manohar et al. 2016 [95]	*In vivo* benchtop demonstration, 125 kVp cone beam, rotating mouse model, single-crystal CdTe detector	Mouse model	0.24%	74.3 cGy/slice	17.83

Table 1.1 continued: Summary of studies on K-shell XFCT sensitivity and dose

Reference	**XFCT acquisition parameters**	**Phantom material & diameter***	**GNP detection limit (% by weight)****	**Estimated dose*****	**Dose-detection limit product (%-cGy)**
Dunning et al. 2018 (1) [115]	Monte Carlo simulation, 81 keV sheet beam, rotating phantom, parallel-hole collimator	Water (2 cm, 0.5-2 mm inserts)	0.08%	30 mGy	0.24
Manohar et al. 2018 [113]	125 kVp cone beam, rotating phantom, CdTe detector	PMMA (3 cm, 6 mm inserts)	0.03% (signal = $1.96\sigma_{bkg}$)	617 cGy (1.87 cGy/proj.)	18.51
Detectors in backscatter or full ring geometries					
Ahmad et al. 2015 [109]	120 kVp pencil beam, linear scanning and rotating phantom, CdTe detector placed in backscatter position	Water (6.4 cm, 2 cm inserts)	0.25%	14.2 mGy	0.36
Dunning et al. 2018 (2)[110]	Monte Carlo simulation, 120 kVp scanning pencil beam, rotating phantom, 8 CdTe spectrometers in backscatter position	Water (2.5 cm, 4 mm inserts)	0.055%	30 mGy	0.165
Bazalova et al. 2012 [107]	Monte Carlo simulation, 110 kVp parallel beam, rotating phantom, energy resolving detector ring	Acrylic (5 cm, 1 cm inserts)	0.061%	10 cGy	0.61

Table 1.1 continued: Summary of studies on K-shell XFCT sensitivity and dose

Reference	**XFCT acquisition parameters**	**Phantom material & diameter***	**GNP detection limit (% by weight)****	**Estimated dose*****	**Dose-detection limit product (%-cGy)**
Ahmad et al. 2014 [120]	82 KeV pencil beam, linear scanning and rotating phantom, multiple detectors placed in optimized backscatter position	Water (2.25 cm, 5 mm inserts)	0.001%	2 mGy (to phantom surface)	0.0002
Stationary phantoms & position-sensitive detectors					
Jung et al. 2017 [116]	140 kVp fan beam, pinhole aperture, stationary phantom, 2 opposing pixelated CZT gamma camera detectors	Water (5 cm, 1 cm inserts)	0.03%	26.1 mGy (average dose)	0.078
Deng et al. 2018 [117]	Monte Carlo simulation, 125 kVp fan beam, multi-pinhole collimator, stationary phantom, 2 opposing pixelated detectors	PMMA (3 cm, 3 mm inserts)	0.09% (CNR = 3.29)	100 billion particles	[*Dose not applicable*]

[a]Cylindrical phantom unless otherwise indicated. Dimensions given are diameters.
[b]Determined by Rose criterion (CNR = 4) unless otherwise indicated [121].
[c]Dose to center of phantom over course of imaging unless otherwise indicated.

1.3.2 X-ray fluorescence emission tomography (XFET)

We have previously shown that the most advantageous XFCT acquisition methods utilize slit or pinhole apertures with pencil beams or fan beams, respectively, without object rotation [108, 122]. These new geometries reduce imaging time through either increased detection efficiency or greater volume of irradiation, and have increased information content per de-

tected photon, which has the potential to greatly improve sensitivity [108, 122, 123]. We refer to this new acquisition method as x-ray fluorescence *emission* tomography (XFET), which is similar to but offers distinct advantages over conventional XFCT.

As seen in Section 1.3.1, conventional XFCT utilizes an x-ray pencil beam, rotating sample, and non-imaging detector. Figure 1.1 contrasts XFCT and XFET: XFET utilizes an x-ray pencil beam, slit (or pinhole) aperture, and a pixelated, photon-counting, energy-sensitive detector, in the geometry seen in Fig. 1.2. During XFET acquisition, the object is translated perpendicularly through the beam without rotation, and metal atoms along the illuminating beam will emit x-ray fluorescence isotropically. The slit aperture encodes spatial information by allowing a column of pixels within the energy- and position-sensitive detector to detect fluorescence only from a specific axial segment of the beam. With this geometry, XFET allows for direct measurement of the metal without the need for tomographic image reconstruction, reducing noise amplification, albeit with loss of geometric efficiency. This spatial encoding also allows for partial field-of-view imaging and quick probing of metals in regions of interest. The combination of the slit/pinhole apertures and energy-sensitive CdTe detectors limit Compton scatter contamination, providing potentially greater sensitivity than XFCT. Indeed in preliminary studies, XFET has demonstrated unprecedented detection limits in imaging Gd (0.01%) compared to studies that utilize a similar dose ($\sim$3.26 Gy) [124].

Although several distinct XFCT geometries aside from conventional XFCT have been utilized, most require object rotation and sinogram acquisition. Therefore, XFCT acquisition resembles transmission-based *computed* tomography. XFET is named for its resemblance to *emission* tomography systems such as single-photon emission computed tomography (SPECT) and positron emission tomography (PET). To our knowledge, our group was the first to consider a dose-efficient pencil beam and slit aperture geometry, but XFET bears strong resemblance to some later XFCT studies that incorporate fan beams and pin-

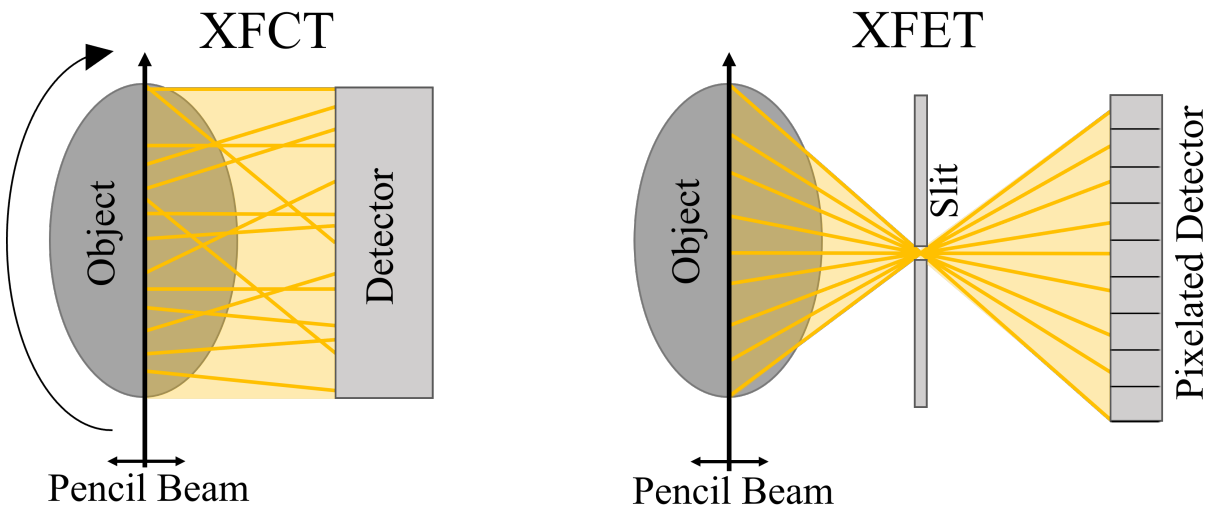

Figure 1.1: Comparison of XFCT and XFET geometry. ©2023 IEEE

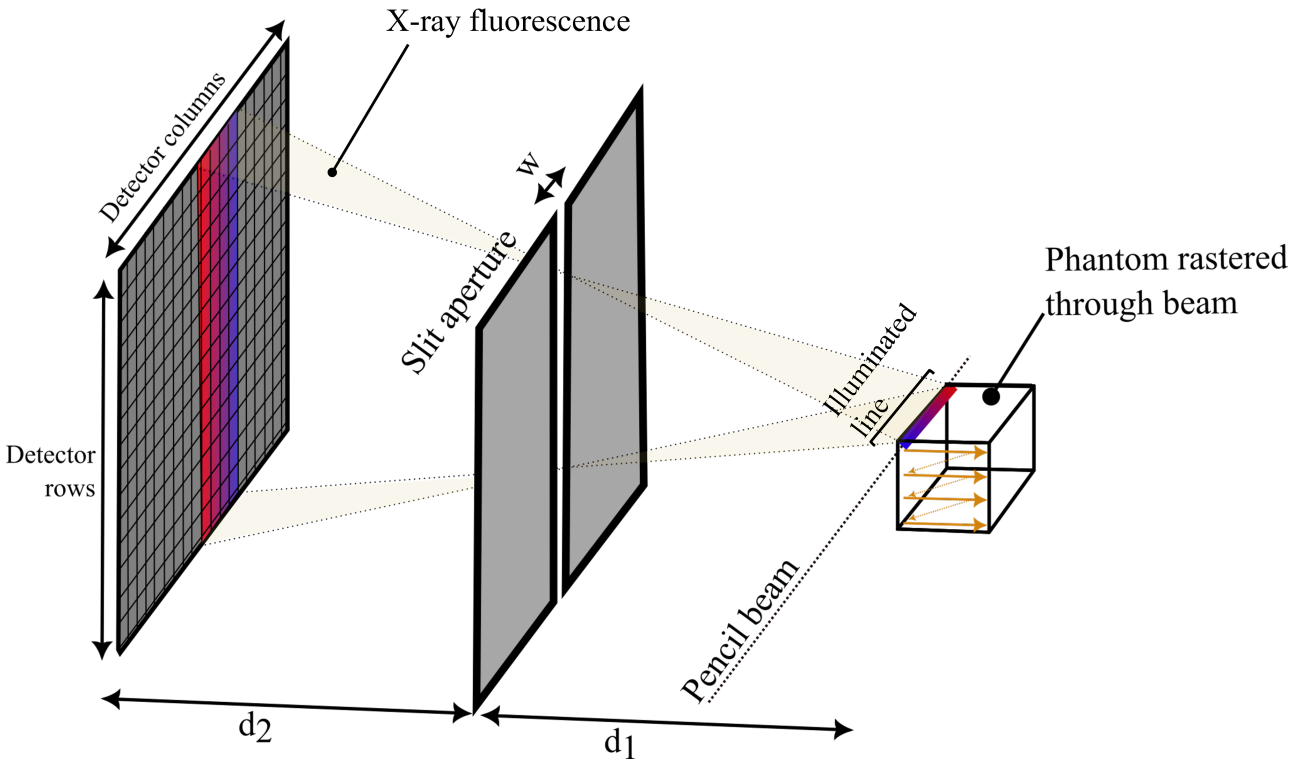

Figure 1.2: Mechanism of XFET imaging. The object is rastered through the x-ray pencil beam, resulting in fluorescent emissions along a line of illumination. Fluorescence emissions are directly mapped to the detector plane, spatially inverted, which is demonstrated by the red and blue regions in both the object and detector plane (not to scale).

hole apertures with stationary objects [116, 117]. These studies have confirmed XFET's sensitivity and dose advantages: when compared to other XFCT GNP studies, the method employed by Jung et al.—which like XFET, probes a non-rotating object—produces a very high sensitivity. With the exception of one highly optimized and clinically impractical XFCT study, which used a monochromatic beam, relatively large gold inserts, and several detectors in a full-ring-backscatter geometry [120], Jung et al.'s method produced the lowest dose-detection limit in Table 1.1 [116]. Therefore, XFET shows promise as a highly sensitive metal mapping imaging modality.

1.3.3 Applications of XFET in therapies

Because XFET has improved sensitivity, partial-field imaging capabilities, and improved tissue penetration depth due to its direct imaging, it can potentially map gold at concentrations and depths used in clinical and preclinical studies.

First, XFET has potential for image guidance for emerging cancer therapies. As discussed in Section 1.2.1, most of the discussed therapies have applications for treating superficial lesions. These superficial lesions cannot be imaged with XFCT due to the requirement of a full sinogram and the inevitable extinguishing of the fluorescent signal at certain sinogram angles. Alternatively, XFET does not require a full sinogram, can image partial fields, and therefore is more practical for imaging the distribution of metals in superficial lesions. Although the fluorescence signal will be significantly attenuated beyond a certain tissue depth, this depth is certainly greater than the depth of NIR and optical light used in PTA and PDT. X-PDT overcomes the depth limitation of PDT by using an x-ray beam for treatment, and therefore will naturally result in x-ray fluorescence emission. XFET can exploit these emissions for monitoring the location of metal-based PSs or nanoscintillators during treatment. With XFET's potential sensitivity improvements, it can certainly image the low concentrations of metals utilized in RT-enhancement therapy, if not PTA with further opti-

mization. Imaging the spatial distribution of metals with XFET before or during treatment would ensure treatment efficacy and reduce adverse effects.

Second, pharmacokinetic and biodistribution studies are crucial for drug development, including drugs delivered with GNP carriers. These studies, usually performed on mouse models, would benefit from a highly sensitive metal mapping modality that did not require repeated animal sacrifice. XFET possesses desirable qualities for this application: high sensitivity (especially for mouse-sized objects), high spatial resolution, and *in vivo* imaging capabilities. XFCT has already been utilized for *in vivo* biodistribution imaging [95, 119]; XFET would provide even greater detection limits that would improve understanding of drug toxicity and half-life. Therefore, XFET would be well suited for biodistribution studies in the preclinical stage of metal-based drug development.

1.3.4 Advancing XFET capabilities

In light of XFET's potential advantages in sensitivity, imaging depth, and imaging time, there remain open questions for further study and additional improvement.

First is the issue of varied fluorescence attenuation: fluorescence emitted from greater depths will naturally be more likely to attenuate than superficial emissions. Thus, attenuation correction is crucial for XFET to obtain accurate and quantitative metal maps. Conventionally, CT or transmission-based imaging provides an attenuation map needed for correction, but at the cost of additional dose to the object or organism. This type of measurement is unavoidable in transmission-based methods like XFCT. Alternatively, XFET's unique geometry that allows for direct fluorescence imaging also allows for a unique method of attenuation estimation. Emitted fluorescent photons probe the attenuation map on their path to a detector; the attenuation map can estimated from these emission data alone. Therefore, joint estimation of metal and the attenuation maps is one area of potential advancement, and its successful implementation would provide XFET with the distinct advantage of negating

the need for an additional, dose-delivering transmission scan.

With joint estimation comes new challenges in estimating metal and attenuation: because metal acts as the emission source in an interior-source tomography problem, its spatial distribution heavily determines what section of the attenuation map is probed and can be reconstructed. With no metal in an object, no attenuation can be recovered; with one small localized region of metal, only the attenuation that lies between this region and a detector pixel can be recovered. Therefore, accurate joint estimation depends on the spatial distribution of metal and detector placement. Of these factors, detector placement is adjustable, and it is critical to explore the effect of this placement on joint estimation.

Finally, the pencil-beam and slit-aperture geometry of XFET has yet to be directly compared to other, more conventional imaging modalities. XFET's detection limit must be quantified to demonstrate proof of benefit in a preclinical or clinical imaging application.

1.4 Dissertation overview

This dissertation focuses on an optimal XFET imaging geometry incorporating an x-ray pencil beam source and slit apertures, with potential to image gold at concentrations lower than possible with conventional XFCT and CT. With each chapter, we provide information necessary to make predictions about XFET's metal mapping capabilities in eventual preclinical and clinical scenarios.

Chapter 2 develops and compares an algorithm to jointly reconstruct metal and attenuation maps in XFET. For attenuation correction, sinogram-based XFCT requires an additional transmission scan at the energy of the fluorescent rays to measure the attenuation map necessary for attenuation correction. Alternatively, XFET's ability to directly image metal allows for the estimation of attenuation along the path of fluorescence emission. Therefore, XFET allows for joint metal and attenuation estimation using emission data alone. This chapter develops a realistic forward model and a joint reconstruction algorithm for numerical gold

and iron phantoms. This reconstruction method is shown to be advantageous over a more conventional algorithm.

Chapter 3 explores the effect of detector count and placement on joint estimation. Image geometry optimization is necessary to obtain accurate metal and attenuation images in XFET. Detector number and placement is one of the most flexible and influential components of XFET geometry. This chapter uses mathematical methods—singular value decomposition (SVD) and eigendecomposition of the Fisher information matrix (FIM)—to determine the effect of detector placement on image quality. Further image reconstructions for various detector arrangements are performed to demonstrate the limitations and capabilities of each arrangement. Implications for XFET's preclinical and clinical capabilities are discussed.

Chapter 4 compares simulations of XFET and CT in the task of mapping various concentrations of gold in numerical contrast and mouse phantoms. This chapter studies the effect of gold concentration and imaging depth on contrast-to-noise ratios (CNRs) achieved by each modality. We also demonstrate XFET's ability to image partial fields, demonstrate feasibility in a preclinical context, and quantify the detection limit of XFET. The results of this chapter inform about the depth and sensitivity limits of XFET compared to CT, and guide discussion about potential clinical and preclinical applications of XFET.

Chapter 5 summarizes the previous chapters and proposes potential directions for additional research.

CHAPTER 2

JOINT ESTIMATION OF METAL DENSITY AND ATTENUATION MAPS WITH PENCIL BEAM XFET

2.1 Introduction

Due to XFET's potential applications for preclinical and clinical metal mapping, its primary aim is reconstructing accurate metal density maps. In the absence of attenuation, obtaining accurate metal maps is straightforward, as XFET is a direct imaging modality with a closed-form solution. However attenuation information, when present, must be estimated to reconstruct accurate metal densities. In this chapter, we build an algorithm for XFET that uses emission data alone to simultaneously estimate the metal density map and the attenuation map needed for correction.

2.1.1 Previous attenuation correction approaches

In XFET, attenuation maps can be viewed as nuisance parameters: parameters not of immediate interest, but that must be estimated to analyze the parameter of primary interest. Attenuation must be corrected for in both XFET and XFCT, especially for high metal densities that cause significant self-absorption. At least two attenuation maps are needed for attenuation correction: one at the beam energy and one at the energy of the emitted fluorescent rays. If there are many elements being imaged simultaneously, there are potentially many attenuation maps that are needed at various fluorescent x-ray energies. Although XFCT allows for reconstruction of the beam attenuation map through the use of simultaneous transmission measurement, it is tedious and difficult to obtain attenuation maps at the characteristic x-ray energies. Previous attempts at image reconstruction in XFCT without pre-measured fluorescent attenuation maps include correcting for uniform attenuation of known materials [101, 110, 125], using transmission information to correct for self-absorption

[126], using iterative algorithms [127, 128, 129], and expressing the unknown attenuation map in terms of known quantities and the unknown element densities [130]. In our previous work, we showed that an alternating approach that makes use of separable paraboloidal surrogates to update the attenuation map outperforms filtered backprojection (FBP) in XFCT image reconstruction [131]. XFCT attenuation correction is an ongoing research problem with no single conventional approach, but a commonly used iterative method is a conjugate gradient method: Schroer used a conjugate gradient approach for XFCT image reconstruction [127], and Shi et al. examined a nonlinear conjugate gradient method with regularization and found that it outperformed both maximum likelihood expectation maximization (MLEM) and FBP algorithms [132].

Similar problems arise in emission tomography, and in time-of-flight positron emission tomography (PET), attenuation sinograms can only be determined up to a constant [133]. Previous attempts at reconstructing attenuation maps with emission data include using iterative methods [134, 135, 136, 137], approaches based on consistency conditions [138, 139, 140], and an inverted Radon transform followed by iterative refinement [141]. In PET joint estimation, several approaches have been developed to overcome the scale problem, including the use of information from scatter coincidences [142, 143], MR-based priors [144] and transmission sources[145].

2.1.2 XFET attenuation correction

Because XFET measures fluorescent emissions directly, emission data alone can potentially be used to reconstruct the attenuation map. In the XFET geometry, one or more pixelated detectors are placed parallel to the beam. During measurement, fluorescent emissions probe a variety of line integrals through the attenuation map, as visualized in Fig. 2.1, where metal along the line of illumination allows for a large number of attenuation line integrals to be measured. Fluorescence measurements can therefore provide an estimated attenuation map,

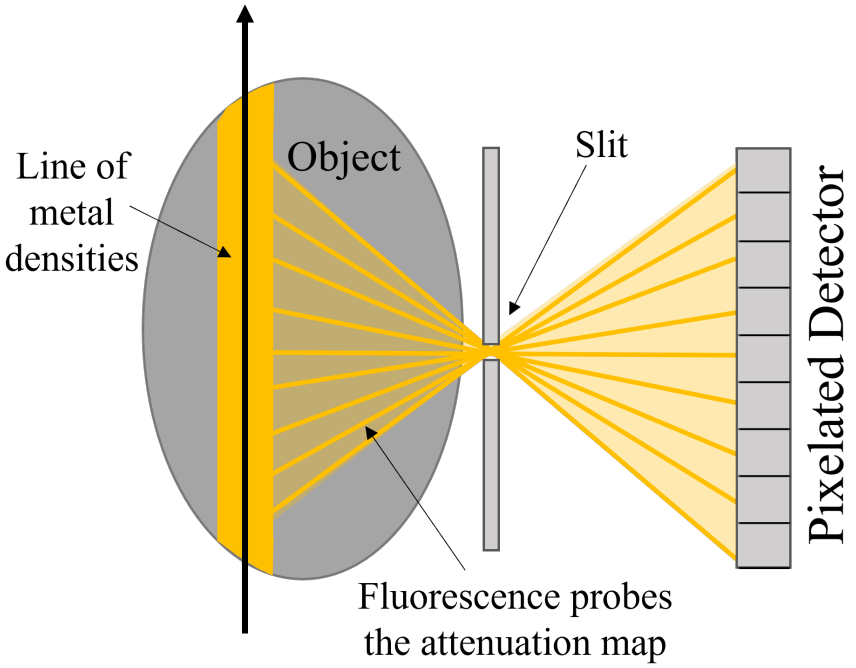

Figure 2.1: Object containing a line of metal opposing an XFET detector, illustrating the possibility of joint estimation: measured fluorescent emissions probe the attenuation map of the object. ©2023 IEEE

which can be used for attenuation correction and estimation of accurate metal maps.

We have previously shown the proposed pencil-beam geometry to be feasible in imaging element maps with attenuation corrections obtained through CT transmission scans [122] or through estimation based on updated element densities [123], but it remains to be seen if accurate density and attenuation maps can be reconstructed without previously obtained transmission measurements.

2.1.3 Chapter summary

In this chapter, we build an alternating algorithm for pencil-beam XFET that simultaneously estimates the metal density map and the attenuation map at the fluorescent energy, without transmission measurements or previous knowledge of an attenuation map at any energy. We then perform this joint estimation using a simplified discrete forward model and

simulated data, to demonstrate the feasibility of XFET geometry and the proposed image reconstruction method.

To solve the inverse problem, we develop and compare two iterative image reconstruction methods to jointly estimate metal and attenuation maps: 1) a simultaneous joint estimation with conjugate gradient based on linearization, and 2) an alternating joint estimation without linearization. Although we have previously used an alternating approach for XFCT attenuation correction [131], the present work includes the first alternating approach to incorporate a closed-form solution for the metal density map. The use of a closed-form solution in this chapter incorporates a direct solution to half of the reconstruction problem and decreases computation time. The conjugate gradient method is a more conventional approach to XFCT attenuation correction, motivating its comparison to our novel alternating approach.

We performed reconstructions of metal density and attenuation maps for two numerical phantoms representing a geological iron sample and a soft tissue sample with gold. We used qualitative and normalized root mean squared error (NRMSE) comparisons to evaluate performance of the two algorithms. We present a final demonstration of the alternating approach for an $(8\text{ cm})^3$ object containing concentrations of gold as low as 5 mg/cm^3; this reconstruction was performed without transmission measurements and without knowledge of an attenuation map at any energy.

2.2 Methods

2.2.1 Forward model

Figures 2.2 and 2.3 display the imaging geometry of XFET. XFET can use one or more detectors; in this chapter, we considered a pair of opposing detectors placed on either side of the object. First, the monochromatic x-ray pencil beam of photon flux I_0 and area A_0 travels

through the object with a beam attenuation map $\boldsymbol{\mu}^{(E_B)}$. Here, the discrete attenuation map vector $\boldsymbol{\mu}^{(E_B)} \in \mathbb{R}^N$, where N is the number of attenuation voxels, contains elements of linear attenuation coefficients, $\mu_k^{(E_B)}$, for each object voxel indexed by k. X-rays of energy E_B will interact with metal of density f_i, primarily through photoelectric interactions. Isotropically emitted fluorescent photons with energy E_F travel through the attenuation map at their energy, $\boldsymbol{\mu}^{(E_F)} \in \mathbb{R}^N$, and are measured at one or more opposing energy-sensitive detector planes behind central slits. The presence of the slit for a fixed pencil beam location encodes spatial information: a given column of pixels on the detector receives photons from a specific axial segment of the pencil beam of length d_0. The slit also limits the angular range for measurement and therefore limits Compton scatter contamination. For simplicity of the model, we choose d_1 to be equal to d_2, and slit width to be half the object voxel width, to allow for a 1:1 mapping between each object voxel and detector column. The object is translated perpendicularly through the fixed x-ray pencil beam to acquire data for the entire object.

The fluorescence from object voxel i measured at detector j, p_{ij}, can be modeled as

$$p_{ij} = \frac{(d_1 + d_2)}{R_{ij}^3} I_0 A_0 D_0 d_0 s t f_i \exp\left(-\sum_k L_{ijk}\mu_k^{(E_F)}\right) \exp\left(-\sum_k L'_{ik}\mu_k^{(E_B)}\right). \tag{2.1}$$

R_{ij} is the distance from the object voxel i to detector pixel j. The cubing of this distance incorporates $1/r^2$ falloff and the obliquity factor, $\frac{d_1+d_2}{R_{ij}}$. D_0 is the area of detector pixel j. t is the exposure time, and

$$s = \frac{\tau}{\rho}(E_B)\xi_K\omega_K\nu_K \tag{2.2}$$

is the product of $\frac{\tau}{\rho}(E_B)$, the photoelectric cross section at the beam energy E_B; ξ_K, the probability that the photoelectric interaction will occur within the K shell; ω_K, the fluorescent yield of the K shell; and ν_K, the branching ratio of the K_α line. The factor $\exp\left(-\sum_k L_{ijk}\mu_k^{(E_F)}\right)$ describes attenuation of the fluorescent rays, where L_{ijk} denotes the

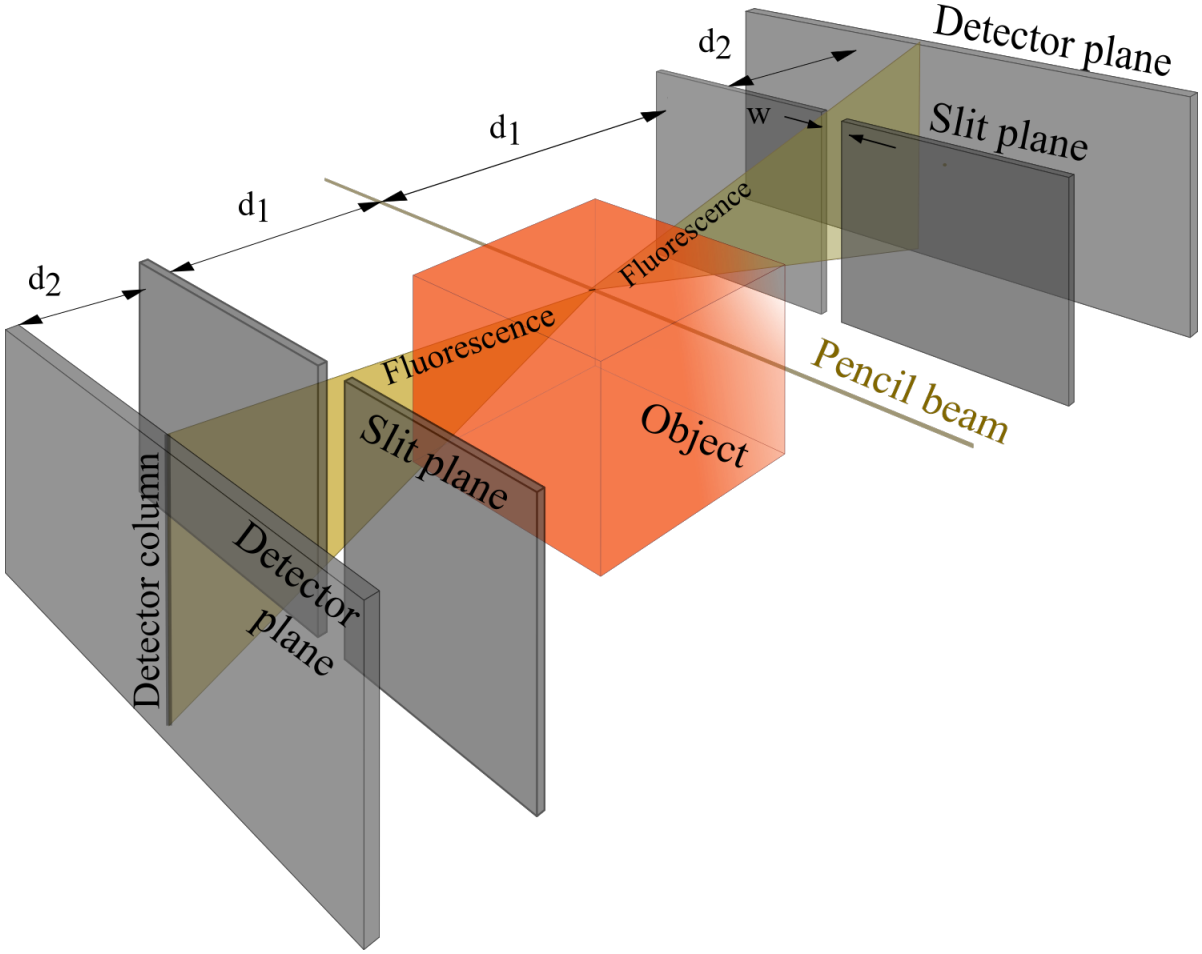

Figure 2.2: Three-dimensional pencil beam XFET geometry using two opposing detectors. ©2023 IEEE

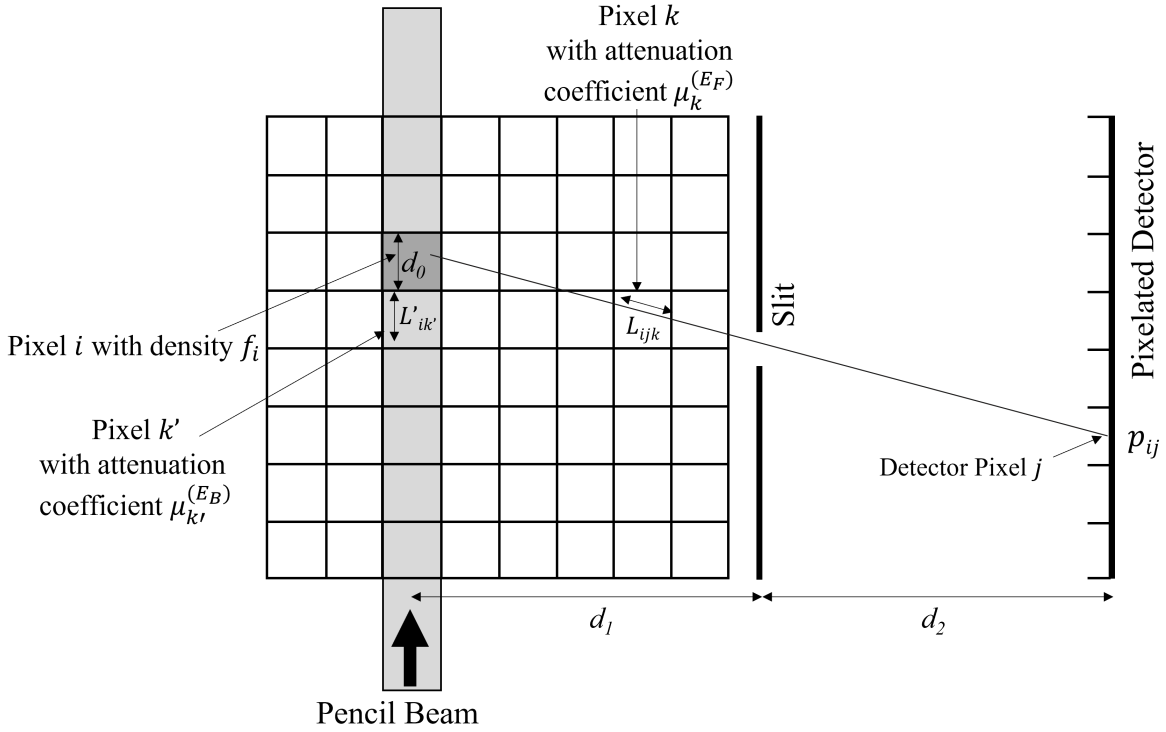

Figure 2.3: Illustration of XFET imaging geometry and term definitions, showing only one detector in two dimensions. Note that the index k' is used in this figure instead of k to distinguish between attenuation at the beam energy and attenuation at the fluorescence energy.

intersection length of the line connecting object voxel i to detector pixel j with the pixel k. The attenuation of the x-ray beam is accounted for in the term $\exp\Big(-\sum_k L'_{ik}\mu_k^{(E_B)}\Big)$, where L'_{ik} denotes the intersection length of the line connecting the object face (where the beam is incident on the object for voxel i) and voxel i with voxel k of $\boldsymbol{\mu}^{(E_B)}$.

We can combine some known terms of (2.1) into a single term, $q_{ij} \equiv \frac{(d_1+d_2)}{R_{ij}^3} I_0 A_0 D_0 d_0 s t$, which leads to the forward model

$$p_{ij} = q_{ij} f_i \exp\Big(-\sum_k L_{ijk}\mu_k^{(E_F)}\Big) \exp\Big(-\sum_k L'_{ik}\mu_k^{(E_B)}\Big). \tag{2.3}$$

This equation represents fluorescent measurements, $\boldsymbol{p} \in \mathbb{R}^{MN}$, (where M is the number of detector pixels) in terms of the unknown metal density map $\boldsymbol{f} \in \mathbb{R}^N$ and unknown attenuation maps $\boldsymbol{\mu}^{(E_F)}$ and $\boldsymbol{\mu}^{(E_B)}$.

2.2.2 Linearization

The forward model in (2.1) can also be reformulated by defining two new unitless terms,

$$q'_{ij} \equiv \frac{(d_1+d_2)}{R_{ij}^3} I_0 A_0 D_0 t \exp\left(-\sum_k L'_{ik}\mu_k^{(E_B)}\right), \tag{2.4}$$

and

$$n_i \equiv d_0 s f_i, \tag{2.5}$$

such that (2.1) becomes

$$p_{ij} = q'_{ij} n_i \exp\Big(-\sum_k L_{ijk}\mu_k^{(E_F)}\Big). \tag{2.6}$$

Both sides of (2.6) can be divided by q'_{ij}, and if $n_i \neq 0 \ \forall \ i$, this new forward model can be linearized,

$$\ln\left(\frac{p_{ij}}{q'_{ij}}\right) = \ln(n_i) - \sum_k L_{ijk}\mu_k. \tag{2.7}$$

Then, defining $y_{ij} \equiv \ln\left(\frac{p_{ij}}{q'_{ij}}\right)$ and $g_i \equiv \ln(n_i)$, (2.7) becomes

$$y_{ij} = g_i - \sum_k L_{ijk}\mu_k. \tag{2.8}$$

In order to reexpress (2.8) as a matrix vector equation, we introduce data vector $\boldsymbol{y} \in \mathbb{R}^{NM}$ with elements y_m, where $m = iN + j$. Likewise, we introduce a matrix L of size $NM \times N$ with elements L_{mk}. g_i has no j dependence, so a repetition matrix R is introduced, also of size $NM \times N$,

$$R = \begin{pmatrix} \boldsymbol{r_0} & 0 & 0 & \cdots & 0 \\ 0 & \boldsymbol{r_0} & 0 & \cdots & 0 \\ 0 & 0 & \boldsymbol{r_0} & \cdots & 0 \\ \vdots & \vdots & \vdots & \ddots & \vdots \\ 0 & 0 & 0 & \cdots & \boldsymbol{r_0} \end{pmatrix}, \tag{2.9}$$

where $\boldsymbol{r_0}$ is a $M \times 1$ vector of ones. When $N \times 1$ vector $\boldsymbol{g}$ is multiplied by R, the resulting vector will be the same dimension as $\boldsymbol{y}$, with repeated values of $\ln(n_i)$ for every j. The vector $\boldsymbol{q'} \in \mathbb{R}^{MN}$ containing elements q'_{ij} incorporates the term L'_{ik}, which becomes extended in a similar way as $\boldsymbol{g}$. (2.8) can now be rewritten in matrix notation as

$$\boldsymbol{y} = R\boldsymbol{g} - L\boldsymbol{\mu}, \tag{2.10}$$

where $\boldsymbol{g} \in \mathbb{R}^N$ is a vector that includes linearized metal densities, and $\boldsymbol{\mu} \in \mathbb{R}^N$ is a vector of attenuation coefficients, both indexed lexicographically. To avoid scale-variance in the imaging model, we normalize L by voxel size, $L_{\max}$, and define $\boldsymbol{\mu'} \equiv \boldsymbol{\mu} L_{\max}$, such that (2.10) becomes

$$\boldsymbol{y} = R\boldsymbol{g} - \frac{L}{L_{\max}}\boldsymbol{\mu'}. \tag{2.11}$$

This can be written as

$$\boldsymbol{y} = A\boldsymbol{x}, \tag{2.12}$$

where the block matrix $A = [R \,|\, -\frac{L}{L_{\max}}]$, with $A \in \mathbb{R}^{NM \times 2N}$, combines the repetition matrix

and the matrix of normalized intersection lengths, and $\boldsymbol{x} \in \mathbb{R}^{2N}$ is a vector concatenating terms that contain all unknown metal densities and attenuation coefficients: $\boldsymbol{x} = \begin{bmatrix} \boldsymbol{g} \\ \boldsymbol{\mu'} \end{bmatrix}$.

2.2.3 Inverse model algorithms

In the absence of attenuation, a column of detector measurements can be averaged to obtain one fluorescent measurement per object voxel, which gives a direct measurement of metal in the object without tomographic image reconstruction. The estimates from multiple detectors can be averaged to improve noise and perhaps reduce the effect of attenuation. However, this approach will underestimate the metal density of an attenuating object. Therefore, we use the mean of opposing views as a point of comparison for our more complete joint estimation algorithms, discussed in this section.

This section first considers reconstruction in the case of a known beam and fluorescent attenuation map. We then consider the case of an unknown fluorescent attenuation map and a known beam attenuation map, and finally consider a case in which neither map is known.

Known beam and fluorescence attenuation maps

If both the attenuation map at the beam energy and fluorescent energy are known, there is a closed-form solution for the metal densities. First, the known term q_{ij} in (2.3) can be combined with the known beam attenuation factor to form a new known term,

$$q''_{ij} \equiv q_{ij} \exp\left(-\sum_k L'_{ik} \mu_k^{(E_B)} \right). \tag{2.13}$$

(2.3) becomes:

$$p_{ij} = q''_{ij} f_i \exp\left(-\sum_k L_{ijk} \mu_k^{(E_F)} \right). \tag{2.14}$$

Assuming that p_{ij} are Poisson random variables, this model will have a Poisson likelihood function,

$$\mathcal{L}(\boldsymbol{p}\,;\,\boldsymbol{f},\boldsymbol{\mu}) = \sum_{i,j}\Big\{\, p_{ij}\,\ln\Big[q''_{ij}f_i\,\exp\Big(-\sum_k L_{ijk}\mu_k\Big)\Big]\,-\,q''_{ij}f_i\,\exp\Big(-\sum_k L_{ijk}\mu_k\Big)\,\Big\}, \quad (2.15)$$

where $\boldsymbol{\mu}$ is shorthand for $\boldsymbol{\mu}^{(E_F)}$, $\boldsymbol{f}$ is the metal density map, and $\boldsymbol{p}$ is the vector of measurements. In Appendix A, we take the derivative of the Poisson likelihood function and reveal a closed-form solution for the metal densities,

$$\hat{f}_i = \frac{\sum_j p_{ij}}{\sum_j q''_{ij}\exp(-\sum_k L_{ijk}\mu_k)}. \quad (2.16)$$

This result states that to obtain the maximum likelihood estimate for the metal map in (2.16), columns of detector pixels should be summed and divided by the column sum of their associated attenuation factors, $\exp(-\sum_k L_{ijk}\mu_k)$, multiplied by the known term q''_{ij}.

Known beam attenuation map, unknown fluorescence attenuation map

For the case of a known attenuation map at the beam energy, which can be obtained through previous transmission measurements, we develop and compare two iterative algorithms to jointly estimate the metal map $\boldsymbol{f}$ and the fluorescent attenuation map $\boldsymbol{\mu}$.

a) Linearized conjugate gradient approach:

For the linearized imaging model developed in (2.12), we choose the likelihood function $\mathcal{L}(\boldsymbol{x};\boldsymbol{y})$ to be a least squares objective function, and the total objective function as

$$\begin{aligned}\phi(\boldsymbol{x};\boldsymbol{y}) &= \mathcal{L}(\boldsymbol{x};\boldsymbol{y}) + \gamma\boldsymbol{x}^T\boldsymbol{x} \\ &= (\boldsymbol{y}-A\boldsymbol{x})^T(\boldsymbol{y}-A\boldsymbol{x}) + \gamma\boldsymbol{x}^T\boldsymbol{x}, \end{aligned} \quad (2.17)$$

where γ is the regularization parameter associated with Tikhonov regularization. Tikhonov

regularization was used to aid in the reconstruction of this ill-conditioned problem. We chose to minimize this objective function with a conjugate gradient method. First, we constructed a vector $\mathbf{\Gamma} \in \mathbb{R}^{2N}$ that contained elements equal to γ, so that the regularization term could be applied to the attenuation portion of $\boldsymbol{x}$ alone. Because the conjugate gradient approach relies on a symmetric imaging matrix and because we applied Tikhonov regularization, we define $H \equiv A^T A + \mathbf{\Gamma}^{\boldsymbol{T}} I$ and $\boldsymbol{y'} \equiv A^T \boldsymbol{y}$ for use as the system matrix and data vector, respectively, in the conjugate gradient algorithm.

b) Non-linear alternating approach: The second image reconstruction method avoids linearization and alternates between updating 1) the attenuation map at the fluorescence energy with a separable paraboloidal surrogates (SPS) algorithm, and 2) the metal map with the closed form solution of (2.16). This alternating approach monotonically increases the objective function, which is the Poisson likelihood function with an additional quadratic roughness penalty function weighted by roughness parameter β,

$$\phi(\mathbf{p}\,;\,\mathbf{f},\boldsymbol{\mu}) = \sum_m \Big\{ p_m \,\ln\Big[q''_m f_m \exp\Big(-\sum_k L_{mk}\mu_k\Big)\Big] - q''_m f_m \exp\Big(-\sum_k L_{mk}\mu_k\Big)\Big\} \\ -\beta \sum_r \frac{1}{2} w_r \Big(\sum_k c_{rk}\mu_k\Big)^2. \quad (2.18)$$

(2.18) uses the combined index $m = iN + j$. Remaining terms used in (2.18) are defined in the List of Mathematical Symbols. The alternating approach begins with an initial estimate of the density map $\boldsymbol{f}^{(0)}$ equaling the mean of opposing views, and a constant fluorescence attenuation map $\boldsymbol{\mu}^{(0)} = 0$ for the first iteration. It also assumes a known beam attenuation map, incorporated into term q''_m. While holding the current estimate of $\boldsymbol{f}$ fixed, the attenuation map at the fluorescent energy is updated with (2.19), which is the SPS algorithm

derived in Appendix B and Fessler [3] with a roughness penalty,

$$\mu_k^{(n+1)} = \left[\mu_k^{(n)} + \left(\frac{\sum_m^{N_Y} L_{mk} q''_m f_m^{(n)} \exp\left(-\sum_{k''} L_{mk''}\mu_{k''}^{(n)}\right)}{\sum_{m=1}^{N_Y} L_{mk} L_m c_m^{(n)} + \beta \sum_{r=1}^{K} |c_{rk}| c_r w_r} \right.\right.$$
$$\left.\left. \frac{-\sum_m^{N_Y} L_{mk} p_m - \beta \sum_{r=1}^{K} c_{rk} w_r \sum_{k''=1}^{N} c_{k''r}\mu_{k''}^{(n)}}{\sum_{m=1}^{N_Y} L_{mk} L_m c_m^{(n)} + \beta \sum_{r=1}^{K} |c_{rk}| c_r w_r}\right)\right]_+ . \tag{2.19}$$

The $[]_+$ enforces non-negativity. All remaining variables used in (2.19) are defined in the List of Mathematical Symbols.

Holding $\boldsymbol{\mu}^{(n+1)}$ fixed, the closed-form solution found in (2.16) can be used to update the metal density map. Rewriting (2.16) for clarity with original indices i and j, the metal densities will be updated with

$$\hat{f}_i^{(n+1)} = \frac{\sum_j p_{ij}}{\sum_j q''_{ij} \exp\left(-\sum_k L_{ijk}\mu_k^{(n+1)}\right)}. \tag{2.20}$$

The metal density elements $\hat{f}_i$ in (2.20) become f_m in (2.19) by the index transformation $m = iN + j$. In each iteration of this algorithm, (2.19) and (2.20) are alternated.

Unknown beam and fluorescence attenuation maps

For an unknown beam and fluorescent attenuation map, the two-step alternating approach can still be employed for the gold object: for a pencil beam energy at the K-edge of the metal, Fig. 2.4 shows that $\mu_k^{(E_B)}$ is related approximately to $\mu_k^{(E_F)}$ by a simple linear transformation,

$$\mu_k^{(E_B)} \approx b\mu_k^{(E_F)} + a, \tag{2.21}$$

for gold concentrations between 0 and 2% by weight in soft tissue. a and b are constants that are known *a priori* for a given beam energy. Using (2.21), $q''_m = q_m \exp\left(-\sum_k L'_{mk}\mu_k^{(E_B)}\right)$

becomes

$$q''_m = q_m \exp\left[-\sum_k L'_{mk}\left(b\mu_k^{(E_F)} + a\right)\right]. \tag{2.22}$$

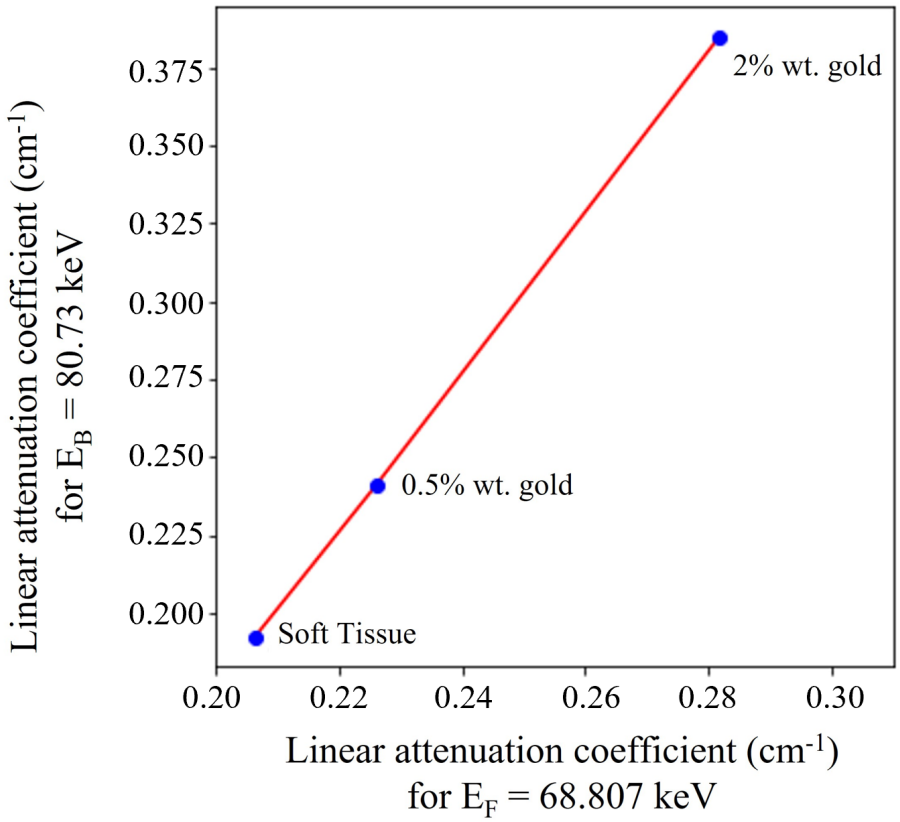

Figure 2.4: The attenuation map at the beam energy displays a linear relationship with the attenuation map at the fluorescent energy for concentrations of gold in soft tissue. The linear fit has a slope of $b = 2.5556$ and a y-intercept of $a = -0.3355$. (Data source: [1] and [2]).

When the beam attenuation map is unknown, we first assume a known density map and constant fluorescent attenuation map. Then, (2.19) and (2.20) are alternated to update the attenuation map and density map respectively, using (2.22) for q''_m terms everywhere they appear (see Appendix B).

When transmission measurements are available, it is simple to acquire a beam attenuation map and use (2.21) to solve for a fluorescent attenuation map. However our ultimate aim

is to build an algorithm that jointly estimates the metal and attenuation maps without previous knowledge of attenuation maps at any energy, to save time and dose.

2.2.4 Gold and iron phantoms

Two 20×20×20 numerical phantoms were constructed. The first was a 4 µm voxel size iron phantom with densities of 0.01, 0.70, and 1.05 g/cm^3 in a background of a carbon, oxygen, and silicon mixture, meant to represent a geological sample. The second was a 4 mm voxel size gold phantom with densities of 0.0005, 0.0050, and 0.0220 g/cm^3 in a soft tissue background, meant to resemble a biological sample similar to those used in preclinical imaging. Voxel sizes were chosen to maintain similar relative attenuation levels between the two phantoms, while keeping both phantoms at size 20×20×20. The metal map for the gold object is shown in Fig. 2.5; both iron and gold objects had the same shape, an adaptation of the phantom considered in Golosio et al. [128], but contained varying levels of their respective metals. The physical factors in (2.2) are given in Table 2.1 below for both objects.

Table 2.1: Physical factors of (2.2) for iron and gold objects

	Iron	***Gold***
$\frac{\tau}{\rho}(E_B)[cm^2/g]$	405.9	8.5
ξ_K	0.88	0.82
w_K	0.36	0.96
ν_K	0.60	0.50

Data were taken from [2], [146], [147], and [148]

We calculated attenuation maps for iron (6.4 keV) and gold (68.8 keV) K_{α_1} energies. We constructed additional attenuation maps for the K-edge energies of gold (80.7 keV) and iron (7.11 keV) to simulate attenuation maps at the pencil beam energy to account for beam attenuation. We will extend these benchtop monochromatic sources at 80.7 keV and 7.11 keV, respectively, to realistic, polychromatic sources in future work. In realistic

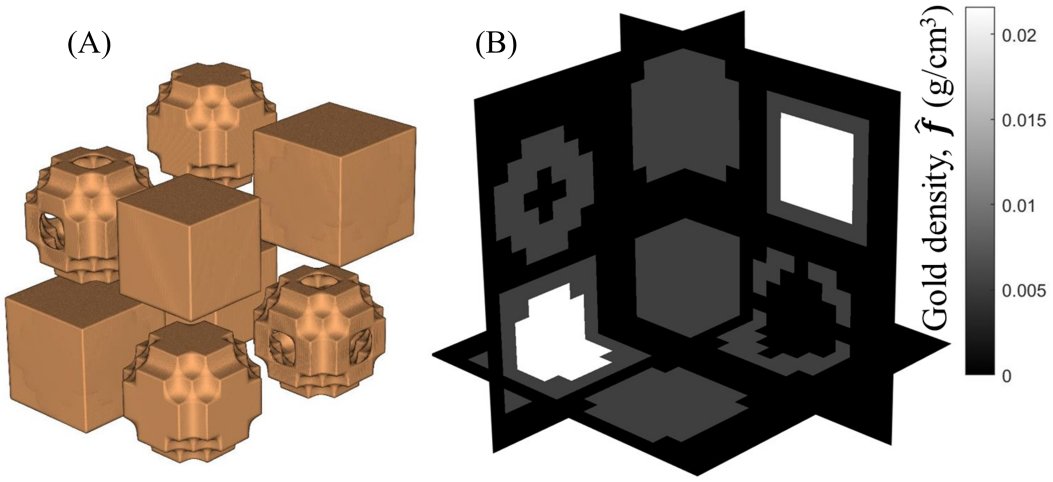

Figure 2.5: Gold object used for joint estimation. A) volumetric view of gold densities, B) slices of gold density object showing buried regions of dense gold. The attenuation map is not shown, but resembles the shape of this object and includes a cubic soft tissue background. ©2023 IEEE

data collection, the energy of the beam and the fluorescence x-rays are known, allowing for the linear relationship in (2.21) to be utilized. We assumed a Poisson noise model when simulating XFET data for these objects. Compton scatter was initially considered negligible due to the combination of using a monochromatic source, energy-sensitive detectors, and the limited angular range provided by the slit. However Compton scatter is modeled in Chapter 4.

2.2.5 Simulation studies

After simulating data collection with the discrete forward model given in (2.1), for both iron and gold numerical phantoms, we reconstructed both objects using the linearized approach assuming a known beam attenuation map. Reconstructions with the conjugate gradient method used 250 iterations for both iron and gold objects, and convergence was verified by the magnitude of the gradient of the objective function, (2.17), reaching zero within numerical precision. The regularization vector $\mathbf{\Gamma}$ was nonzero only for the attenuation portion of the

unknown vector in the conjugate gradient method, since empirically, regularization helps stabilize that estimate. We first empirically optimized γ, the elements of $\mathbf{\Gamma}$, to 1000 for both phantoms; we minimized this value while still avoiding the checkerboard effect seen when γ was too small. A vector of ones was the initial estimate for the conjugate gradient algorithm for both iron and gold, and any negative values in the final attenuation map reconstructions were clipped and set to zero.

We also reconstructed iron and gold objects using the penalized alternating approach ((2.19) and (2.20)), assuming a known beam attenuation map. Iterations continued until the root mean square relative change in the density map fell below 5E−4, that is,

$$\sqrt{\frac{\sum_i \left(f_i^{(n+1)} - f_i^{(n)}\right)^2}{\sum_i \left(f_i^{(n)}\right)^2}} < 0.0005. \tag{2.23}$$

This criterion resulted in 20 iterations for gold and 91 iterations for iron. We first optimized β empirically to 1E−6 for iron and 1E−4 for gold. We compared the results from the alternating approach to the results from the linearized approach. The mean of opposing views was used as the initial density map estimation, and a vector of zeros was used as the initial attenuation map estimation for all alternating reconstructions. For the iron object reconstructed with the alternating approach, we also report attenuation factor maps consisting of the average attenuation factor, $\exp(-\sum_k L_{ijk}\mu_k)$, seen by all detectors for a given object voxel.

Finally, we reconstructed the gold object with the alternating approach ((2.19) and (2.20)), using the convergence criterion given in (3.14), assuming unknown beam and fluorescent attenuation maps. We first optimized β to 1E−4.

Additional factors in the forward model included the beam photon flux (10^{18} photons/cm^{2}s for iron, 10^{12} photons/cm^{2}s for gold), beam cross sectional area and detector pixel area (both (4 µm)^2 for iron, (4 mm)^2 for gold), exposure time (1.0 s for iron, 0.1 s for gold), fluorescence

yield, probability, and other physical parameters outlined in (2.1). d_1 and d_2 were set to 80 µm, and slit width was 2 µm for iron. For gold, d_1 and d_2 were set to 8 cm, and slit width was 2 mm. NRMSE between reconstructed and true objects, as well as qualitative comparisons, were used to evaluate the accuracy of each method. NRMSE was defined to be the RMSE divided by the mean of the true object.

2.3 Results

2.3.1 Comparison of algorithms with known beam attenuation

Figure 2.6 compares reconstructions of the iron metal map for four slices of the 3D object. Slices are normal to the illumination beam's propagation direction. Included in Fig. 2.6 is the arithmetic mean of the opposing detectors' views, without beam attenuation correction. NRMSE values calculated for each reconstruction are listed in Table 2.2. The penalized alternating approach outperformed the linearized approach visually and quantitatively for both the iron and gold objects. The NRMSE values of the iron and gold maps estimated with the linearized approach were 196% and 438% greater, respectively, than the values obtained with the alternating approach.

Similarly, Fig. 2.6 compares reconstructions of the attenuation map for the iron object, for four slices of the 3D object. The alternating approach visually outperformed the linearized approach, and the linearized approach resulted in NRMSE values 39% and 278% greater than those from the alternating approach for iron and gold, respectively. The linearized approach generally underestimated the attenuation maps. The attenuation maps reconstructed with both approaches are oversmoothed and are not as qualitatively accurate as the reconstructed density maps. However, the attenuation map is a nuisance parameter that serves only to enable accurate density reconstructions. So while the oversmoothing itself is not a critical issue, it could cause inaccuracies in the metal density estimate. The

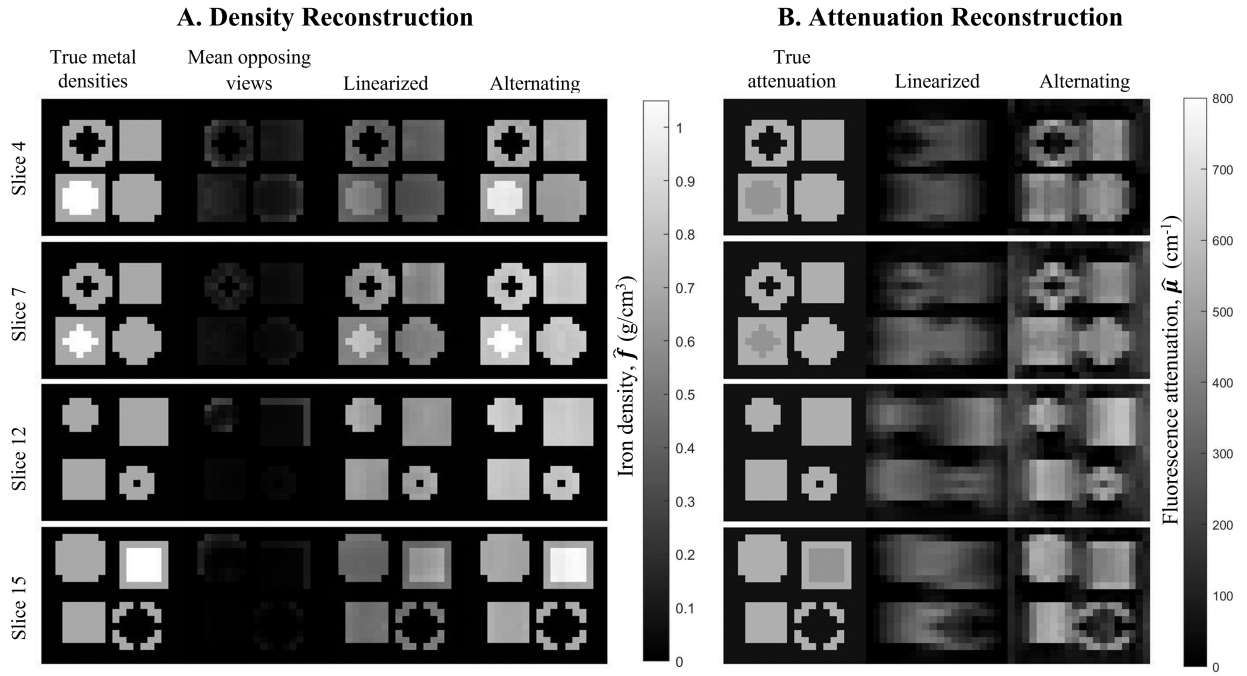

Figure 2.6: A). Slices through reconstructed density maps and true iron object. From left to right: true density map, mean of opposing views without attenuation correction, linearized approach (250 iterations, $\lambda = 1000$), alternating approach (penalized, 91 iterations, $\beta = 1\text{E}{-}6$). B). Slices through reconstructed iron attenuation maps and true attenuation map. From left to right: true attenuation map, linearized approach, alternating approach. From top to bottom: slice 4 of 20, slice 7 of 20, slice 12 of 20, slice 15 of 20. ©2023 IEEE

attenuation reconstruction with the alternating approach still provided accurate values for the average attenuation factors seen by each detector, as evident in the attenuation factor map slices in Fig. 2.7.

2.3.2 Demonstration of alternating approach with unknown beam attenuation and noise

Figure 2.8 displays the density and attenuation alternating reconstructions of the gold object with an unknown beam attenuation map. The alternating approach provided accurate metal densities, resulting in NRMSE values similar to those for the alternating approach with a known beam attenuation map. The attenuation map was not as visually accurate as

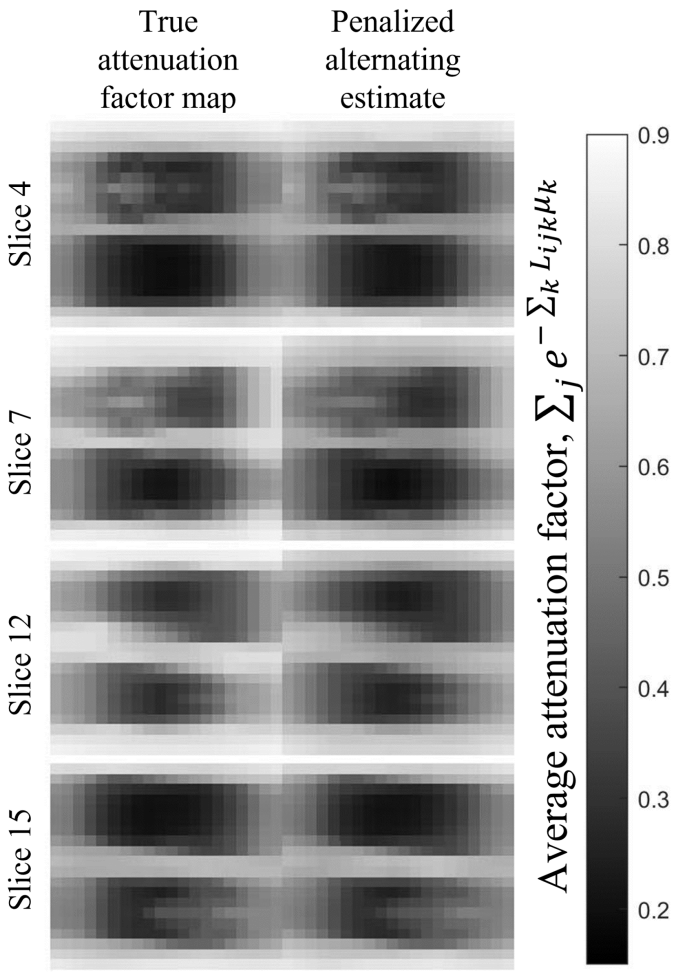

Figure 2.7: Slices through true and estimated average attenuation factor maps. Each displayed voxel contains the average attenuation factor, $\exp(-\sum_k L_{ijk}\mu_k)$, seen by every detector for that emission voxel. Reconstructions were completed with the penalized alternating approach ($\beta = 1\text{E}{-6}$, 91 iterations). From top to bottom: slice 4 of 20, slice 7 of 20, slice 12 of 20, slice 15 of 20.

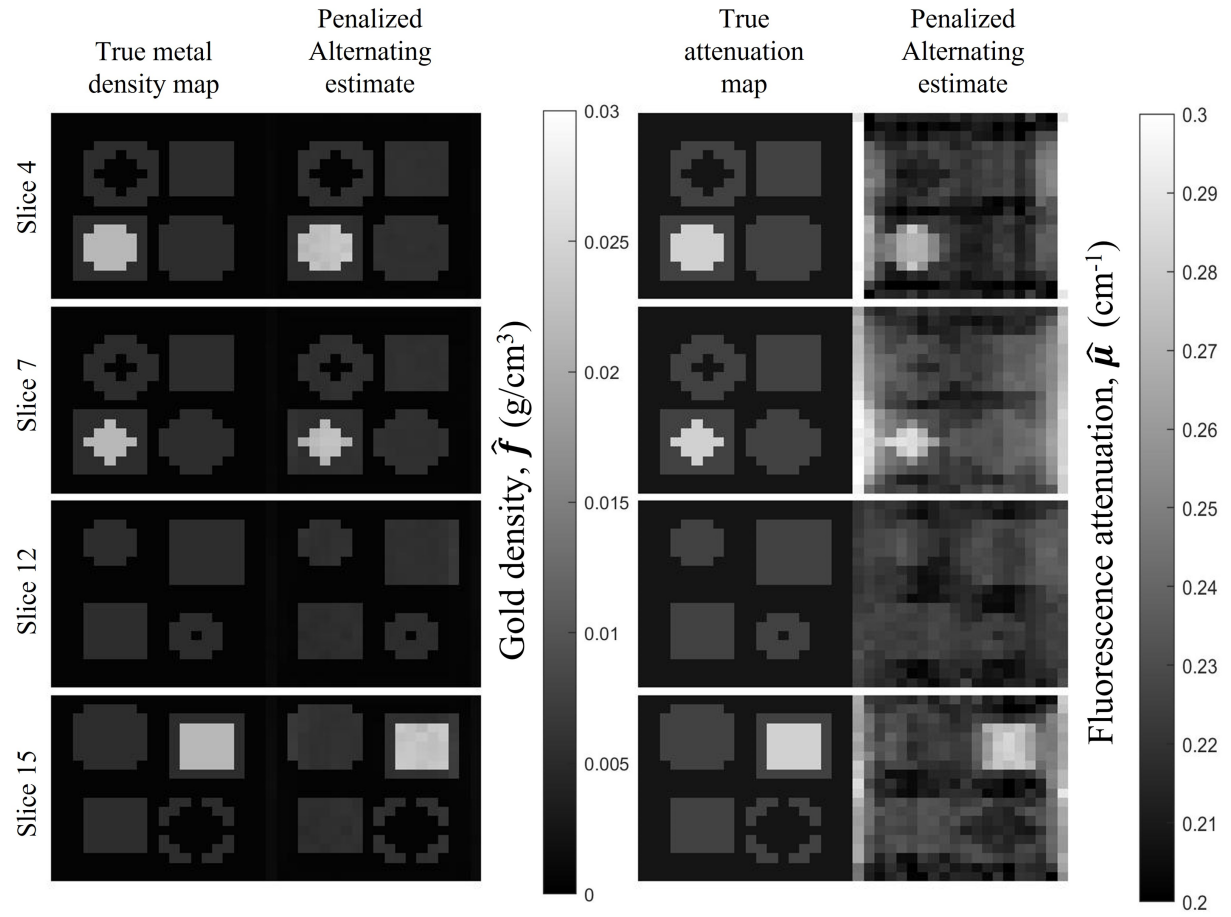

Figure 2.8: Left: Slices through reconstructed gold metal maps and true metal maps. Right: slices through reconstructed and true attenuation maps. All reconstructions were completed with the penalized alternating approach (β = 1E−4, 78 iterations). From top to bottom: slice 4 of 20, slice 7 of 20, slice 12 of 20, slice 15 of 20.

the density map reconstruction, but still provided NRMSE values similar to those for the alternating approach with a known beam attenuation map.

2.4 Discussion and Conclusions

During XFET imaging, only attenuation voxels that lie between a point of fluorescence emission and detection will be probed and have the potential to be recovered. Therefore, the spatial distribution of metal heavily impacts what portion of the attenuation map can be recovered. Given this limitation, it is straightforward to recognize the difficulty in recovering

Table 2.2: NRMSE values for iron and gold density and attenuation maps for compared reconstruction methods

Object	NRMSE	
	Linearized	***Alternating***
Iron object, known beam attenuation		
Density Map	0.77	0.26
Attenuation Map	1.04	0.75
Gold object, known beam attenuation		
Density Map	0.70	0.13
Attenuation Map	0.68	0.18
Gold object, unknown beam attenuation		
Density Map	-[a]	0.19
Attenuation Map	-[a]	0.14

[a]Dashes indicate reconstructions not explored.

the metal and attenuation maps in XFET. Therefore, it is significant that we are able to jointly and accurately reconstruct both maps with our newly developed alternating approach.

The alternating approach outperformed the linearized approach for both the iron and gold objects, evident qualitatively in Fig. 2.6 for the iron object and in calculated NRMSE values for both iron and gold objects. Furthermore, the attenuation estimate of the linearized approach produced non-physical negative values, which were clipped in the final step, as enforcing non-negativity in the conjugate gradient method is nontrivial. As previously discussed, attenuation correction is critical to obtain accurate metal maps. However exact attenuation map accuracy depicted in Fig. 2.6 is desirable but not required: attenuation maps are nuisance parameters, serving mainly to reconstruct accurate metal density maps. As evident in the attenuation factor maps for the iron object (Fig. 2.7), the attenuation map reconstruction still provided accurate values for the average attenuation factor seen by each detector, which is the critical piece of information needed to reconstruct accurate density maps. So while the attenuation map itself can be regarded as a nuisance parameter, its estimation heavily aids the performance of the density reconstruction.

Linearizing the model is not ideal for implementation, as one cannot take the natural log of an object containing voxels of zero metal. Taking the log transform of the data moves zeros to $-\infty$, which could be accounted for by artificially setting those values to very large negative numbers. However, this numerical manipulation destabilizes the conjugate gradient algorithm. The alternating approach does not rely on linearizing the imaging model, which is advantageous, and further emphasizes the superiority of the alternating approach for image reconstruction in pencil beam XFET.

The reasons for the alternating approach outperforming the linear approach are multi-fold. First, the two approaches assume different models: the conjugate gradient approach is linear with a least squares objective function, and the alternating approach is non-linear with a Poisson likelihood function. These inherent differences lead to a contrast in performance, especially considering the information lost with linearizing (namely, zeros in the metal density map). Second, we use different image reconstruction algorithms in each approach. In the linearized approach, we are not maximizing our knowledge of *a priori* information, as some known parameters (s and d_0) must be included in the estimated term for mathematical consistency. The alternating algorithm not only maximizes our knowledge of *a priori* information, but also incorporates a direct solution for half the reconstruction problem.

In this model, there is a potential for cross-talk between the metal density and attenuation map, as these variables are dependent. However, the density map reconstruction demonstrates stability in the face of error in the attenuation map, as seen by Fig. 2.6. In our future investigations, we will study the extent of this cross-talk and its impact on the accuracy of the joint reconstruction.

We also observe that with a known beam attenuation map, most attenuation reconstructions were qualitatively more accurate towards the axial center of the objects compared to the outer slices. This is likely because ray paths pass through central object voxels more frequently than outer ones, providing more information about central voxels. The results of

the SVD also support the explanation that these outer-slice voxels, which are more distant from the detector, are more difficult to reconstruct. However, if metal were placed in these outer slices, the number of x-rays passing through outer-slice voxels will increase, increasing the ability for these voxels to be recovered, so long as the fluorescence emitted from those voxels is not fully attenuated. Furthermore, as long as fluorescence x-rays are not fully attenuated, XFET is robust to imaging all attenuation structures, and is not limited to imaging geometrically matched attenuation and metal maps like those included here.

Using the alternating reconstruction approach on a dataset without knowledge of the beam attenuation map resulted in surprisingly accurate reconstructions. The NRMSE of the reconstructed attenuation and density maps were similar to the NRMSE values produced by the alternating approach with a known beam attenuation map. Instead of impairing the reconstruction, accounting for beam attenuation possibly provides valuable axial information about the attenuation map at the fluorescent energy, since the two attenuation maps are coupled in our formulation. By solving for the attenuation map at the beam energy in every iteration, more information was obtained about the attenuation map at the fluorescent energy, making the inverse problem better determined.

One limitation of this chapter was the use of a monochromatic beam and the lack of consideration of scatter. First, monochromatic beams at lower energies have been used for XFCT in benchtop settings [123], and we have previously demonstrated the functionality of this geometry with monochromatic synchrotron radiation [122]. Polychromatic beams at energies necessary to cause K fluorescence in gold will be considered in future investigations, as these sources may affect our ability to reconstruct the attenuation map without any priors; this study was an introductory demonstration of the feasibility of our geometry and image reconstruction methods. Second, when using a monochromatic source, energy-sensitive detectors, and a slit with limited angular range, scatter should be minimal for our system. With the transition to polychromatic sources in future work, it will be necessary to

model Compton scatter contamination to ensure its negligibility, especially for large objects. In preliminary Monte Carlo studies using a 120 kVp polychromatic source spectrum, we observe that the x-ray fluorescence signal is easily distinguished from the Compton scatter background. Additionally, in our future simulations, we intend to use mismatched voxel sizes in the forward and inverse models to better model the continuous-to-discrete mapping of a real system. Finally, we recognize that the beam flux used for the iron object would give prohibitive dose to the object in a medical context, however this object does not model an organism. Rather, the gold and soft tissue object is more representative of a phantom that could be used in a clinical context, and the beam flux used for this object was much lower and would likely not be dose limited. Our preliminary studies show that a beam flux an order of magnitude lower still provide accurate metal map estimates.

In summary, this chapter compared two image reconstruction methods: 1) a simultaneous joint estimation with a conjugate gradient method based on linearization, and 2) an alternating joint estimation without linearization. Because the alternating approach outperformed the linearized approach for both iron and gold objects, and because linearizing the data posed additional problems for implementation, the alternating approach was considered superior for XFET image reconstruction. Final reconstructions with the alternating approach of a noisy $(8\text{ cm})^3$ object containing concentrations of gold as low as 5 mg/cm^3 resulted in very accurate gold maps, with NRMSE values on the same order of magnitude as the model that considered a known beam attenuation map. This simulation demonstrates a successful joint reconstruction of metal and attenuation maps, using emission data only and without previous knowledge of the beam or fluorescent attenuation map.

CHAPTER 3
EFFECT OF DETECTOR PLACEMENT ON JOINT ESTIMATION IN XFET

3.1 Introduction

In Chapter 2, we developed an image reconstruction algorithm that allows for the joint estimation of both metal and attenuation maps using x-ray fluorescence emission data alone. This joint estimation was performed for two opposing detectors. However, for pencil-beam XFET to be translated into preclinical and clinical applications as a metal mapping modality, some flexibility in detector placement is required. A full-ring geometry would provide the greatest sensitivity, however this geometry is impractical for some of the clinical imaging applications discussed in Chapter 1. Fortunately, XFET is advantageous in that it does not require a full sinogram; this allows for flexibility of detector placement such that sensitivity and spatial resolution can be optimized within the limits of available geometries. However, given the task of joint estimation, this optimization is not trivial. During XFET imaging, the metal within an object acts as an x-ray source in an interior-source tomography problem, and therefore its spatial distribution heavily determines what section of the attenuation map is probed and can be reconstructed. This attenuation estimate then impacts the accuracy of metal quantification. This chapter explores this joint estimation problem: specifically, the effect of detector placement on joint estimation in pencil-beam XFET.

3.1.1 Utility of mathematical tools for geometry optimization

Many mathematical tools have been used to study and optimize imaging components such as detector number and placement. Singular value decomposition (SVD) is a commonly used method of decomposing a linear imaging model into sets of bases that conveniently map between input and output space. By computing SVD for a linear imaging model,

one can deduce the null space of the imaging system, which input-space basis vectors are poorly preserved in imaging, and which input-space basis vectors are well preserved in imaging. Similarly, the Fisher information matrix (FIM) is useful for optimizing experimental design [150], improving convergence of optimization algorithms [151], and investigating impact of variables on unknown parameters of interest [151]. Computing the eigenvectors and corresponding eigenvalues of the FIM is also informative: vectors corresponding to large eigenvalues correspond to steep slopes in search space [150]. Eigenvectors of the FIM have previously been used to efficiently navigate large search spaces [152, 153]. In the context of the present work, the parameters being estimated are pixel values, and eigenvectors of the FIM show patterns of pixels that can be grouped when considering estimator variance and information content. Eigenvectors corresponding to small eigenvalues show patterns of pixels that would be difficult to recover with precision in image reconstruction.

3.1.2 Chapter summary

In this chapter, we investigate the impact of detector number and placement on the uncertainty and conditioning of estimating metal and attenuation pixel values, as well as on the image quality of XFET. We use two mathematical methods to investigate the effects of detector placement: first, we perform SVD on a linearized XFET imaging model for four different detector arrangements to understand which vectors are well-preserved and which are poorly preserved in imaging with various geometries. Second, we compute the eigenvectors and eigenvalues of the FIM for the four geometries. The results of this analysis inform us about which combinations of pixels can be estimated with low variance. Finally, using the four detector geometries, we perform joint image reconstructions for a three-dimensional gold and soft tissue phantom. The results of these reconstructions are consistent with our mathematical investigations of detector arrangement impact on image quality and inform about optimal detector position. This chapter is a critical investigation to explore the limitations

and capabilities of XFET before translation into preclinical applications.

3.2 Methods

3.2.1 Mathematical investigation into effect of detector placement on joint estimation

In Chapter 2, we introduced a discrete forward model for three dimensional XFET imaging:

$$p_{ij} = \frac{(d_1 + d_2)}{R_{ij}^3} I_0 A_0 D_0 d_0 s t f_i \, \exp\left(-\sum_k L_{ijk} \mu_k^{(E_F)}\right) \times \exp\left(-\sum_k L'_{ik} \mu_k^{(E_B)}\right). \quad (3.1)$$

The terms in (3.1) are explained fully in Chapter 2, are included in the List of Mathematical Symbols, and displayed in Fig. 3.1. This expression gives the fluorescence emitted from object voxel i measured at detector pixel j, p_{ij}, in terms of the unknown metal density in that voxel, f_i, the unknown attenuation map at the fluorescence energy, $\boldsymbol{\mu^{(E_F)}}$, and the unknown attenuation map at the monochromatic beam energy, $\boldsymbol{\mu^{(E_B)}}$. The model in (3.1) and the following derivations are general for a 3D object. We will also be applying this model to a 2D slice of an object, as shown in Fig. 3.2.

For the following mathematical investigations, we use a 2D object slice with a thickness of one resolution unit (d_0). X-ray fluorescence, assumed to be emitted from the center of each voxel, passes through a slit of width $d_0/2$ and intersects with one column of detector pixels on each detector plane. Each detector pixel in a column has area D_0.

We first study the conditioning of the joint estimation problem with SVD. This section derives a linearized imaging model from the nonlinear model given in (3.1), and performs SVD for four varied detector arrangements, shown in Fig. 3.3. Singular values and vectors are used to determine what vectors are well preserved in imaging and to identify any null space for the various imaging geometries. Additionally, the degree of decline in the singular value spectrum

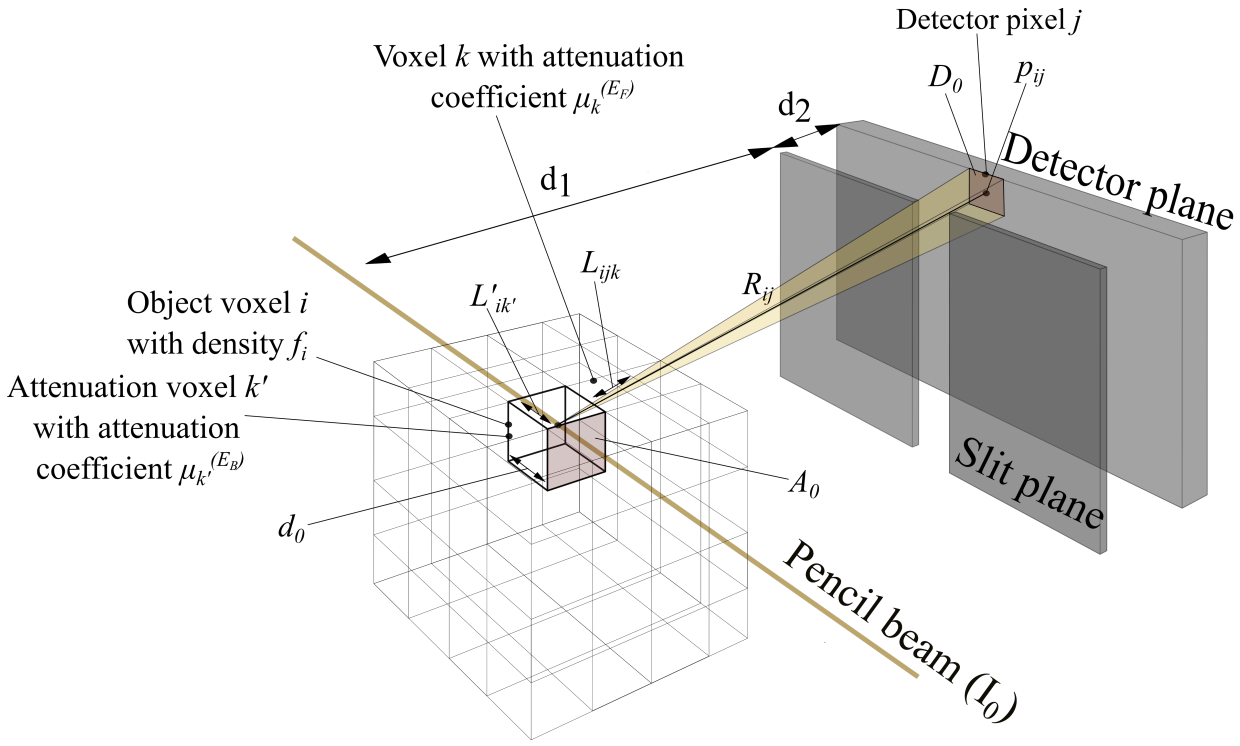

Figure 3.1: Illustration of imaging geometry using one detector with definitions of notations listed in the List of Mathematical Symbols. Note that in this figure, the index k' is used instead of k to distinguish between attenuation at the beam energy and attenuation at the fluorescence energy.

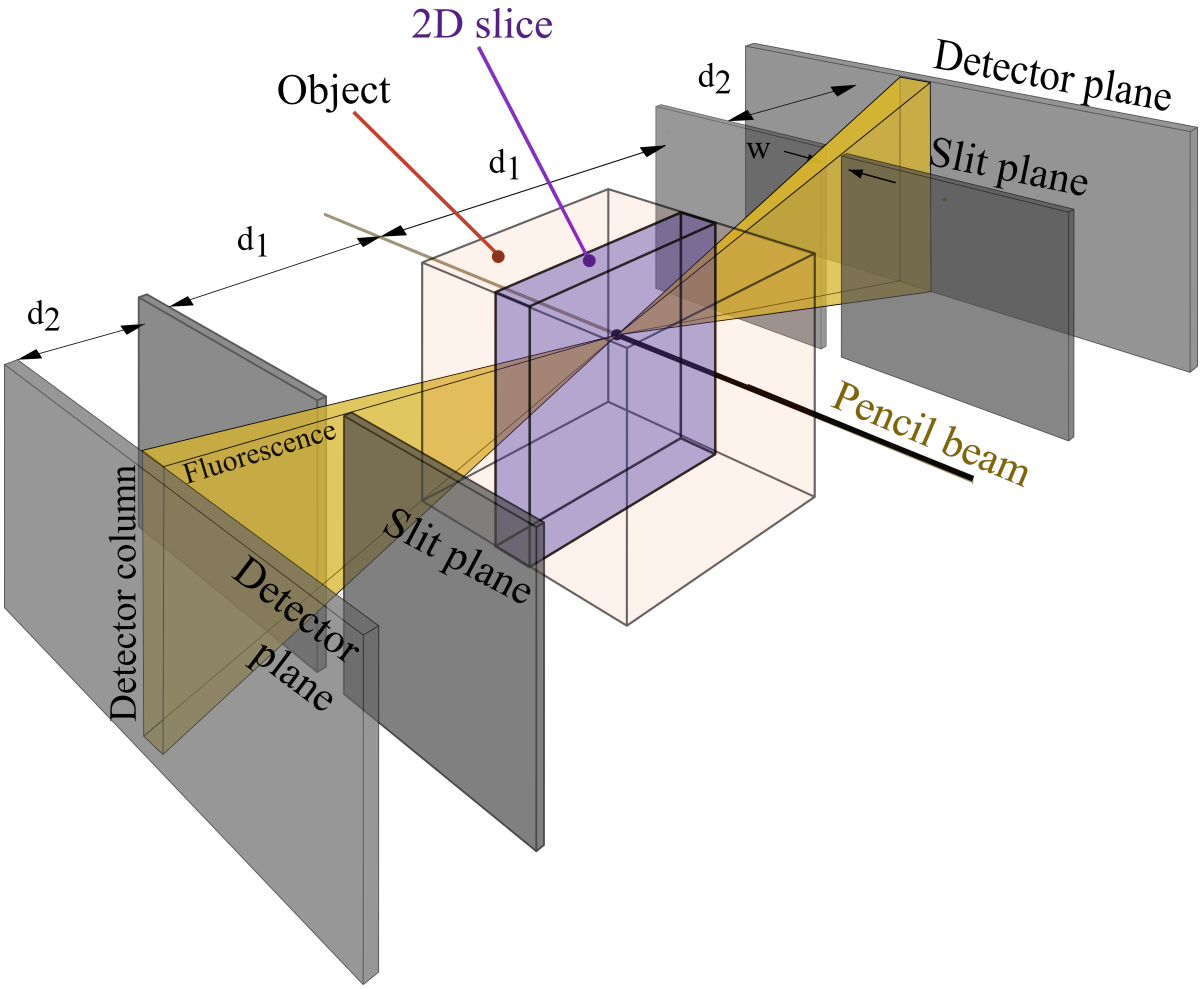

Figure 3.2: XFET geometry utilizing two parallel detectors, with a 2D object slice and detector columns highlighted. The object is rastered through the stationary pencil beam such that all object voxels are illuminated. ©2024 IEEE

gives the degree of ill-conditioning of the problem. A large condition number (i.e., the ratio of the largest to smallest singular values) indicates that the problem is ill-conditioned. An ill-conditioned matrix cannot be inverted easily and requires the use of inverse methods such as regularized iterative algorithms. The four detector arrangements are also considered when performing eigendecomposition of the FIM to study uncertainty and variance in the estimation task. Examining the FIM eigenvectors and eigenvalues reveal patterns of pixels that can be estimated with varying precision in the joint estimation problem.

Singular value decomposition

In Chapter 2, we showed how the forward model in (3.1) can be re-written as

$$\boldsymbol{y} = A\boldsymbol{x}, \tag{3.2}$$

where the block matrix $A = [R \,|\, -\frac{L}{L_{\max}}]$ combines a repetition matrix, defined by (2.9), and the matrix of normalized intersection lengths, and $\boldsymbol{x}$ is a vector concatenating terms that contain all unknown metal densities and attenuation coefficients: $\boldsymbol{x} = \begin{bmatrix} \boldsymbol{g} \\ \boldsymbol{\mu'} \end{bmatrix}$. Note that $\boldsymbol{y} \in \mathbb{R}^{MN}$, where N is the number of object pixels, $\boldsymbol{x} \in \mathbb{R}^{2N}$, and $A \in \mathbb{R}^{NM \times 2N}$.

To understand how detector placement impacts the preservation of metal and attenuation voxels in imaging, we constructed A for each of the two-dimensional detector arrangements shown in Fig. 3.3, for a generic 40×40 object. Object size and discretization impacts the dimensions of A but the SVD of A is general for any object of the same dimension, regardless of metal and attenuation content. Pathlengths through voxels, L_{ijk}, were computed with an algorithm developed by Siddon [154].

We performed SVD on the linearized imaging model A for each of the four detector arrangements. The decomposition $A = UD(\sqrt{\lambda})V^T$ gave singular values λ and corresponding left and right singular vectors. Because XFET image reconstruction is a joint estimation

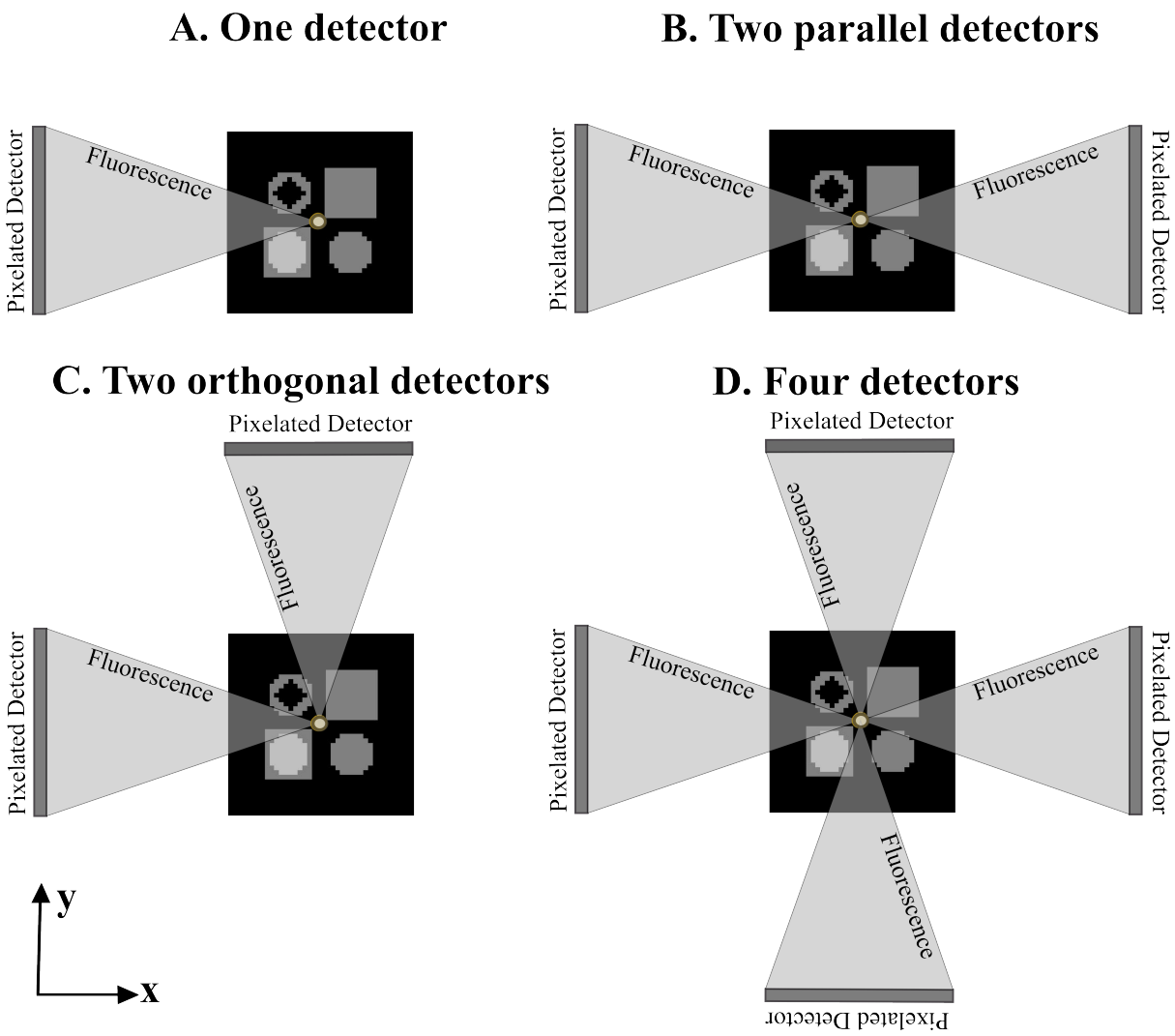

Figure 3.3: Four detector arrangements compared in this chapter. A) one detector; B) two parallel detectors; C) two orthogonal detectors, left and top; and D) four detectors in a full ring geometry. ©2024 IEEE

problem, the attenuation and metal density singular vectors are coupled: the right singular vectors $\boldsymbol{v}_r$ (the columns of V, where r indexes the column) each contain elements v_{rk} relating to both the metal and attenuation mapping. We split each right singular vector into its metal $\boldsymbol{v}_r^f$ and attenuation $\boldsymbol{v}_r^\mu$ components, which were the first and second half of each vector respectively:

$$\boldsymbol{v}_r^f = [v_{r1}, v_{r2}, v_{r3}...v_{rN}], \tag{3.3}$$

and

$$\boldsymbol{v}_r^\mu = [v_{r(N+1)}, v_{r(N+2)}, v_{r(N+3)}...v_{r(2N)}]. \tag{3.4}$$

We reshaped $\boldsymbol{v}_r^f$ and $\boldsymbol{v}_r^\mu$ into 2D arrays and examined them and their associated singular values to understand which combinations of metal and attenuation voxels were well preserved in imaging with various detector combinations. We examined the singular values for the presence of a null space and ill-conditioning for each detector geometry. Before examination, each $\boldsymbol{v}_r^f$ was normalized and exponentiated to bring it from linear space to object space.

Fisher information matrix

Eigenanalysis of the FIM is similar to the SVD analysis in that it gives information content about orthogonal basis vectors. Whereas SVD analysis gives generic information about our linear imaging system, the FIM is object-specific and can give insight into how metal arrangement impacts precision in estimating object parameters. Specifically, for one parameter, Fisher information gives the variance of score functions for various observations evaluated at the true parameter. It is a measure of the amount of information an observation contains about a parameter. Greater Fisher information, or a greater variance in score functions, indicates sharp maximums in the log likelihood function, lower estimator variance, and higher precision in the estimation task. In N-dimensions, the FIM is a symmetric matrix containing covariances of score functions for N parameters. In this chapter, pixel values

serve as the parameters. When performing eigendecomposition of general covariance matrices, the eigenvector of the largest eigenvalue gives the orientation of largest variance in the data under consideration. Therefore, for the FIM, the largest-eigenvalue eigenvectors give patterns of pixels that can be estimated with low variance because these vectors correspond to a direction in likelihood space with the largest variance of score functions.

To derive the FIM for a general 3D case, we first assume that the attenuation map at the beam energy, $\boldsymbol{\mu}^{(E_B)}$, is known and define a new known term,

$$q''_{ij} = \frac{(d_1 + d_2)}{R_{ij}^3} I_0 A_0 D_0 d_0 st \exp\Big(-\sum_k L'_{ik} \mu_k^{(E_B)}\Big), \tag{3.5}$$

to rewrite the model shown in (3.1),

$$p_{ij} = q''_{ij} f_i \exp\Big(-\sum_k L_{ijk} \mu_k\Big), \tag{3.6}$$

where μ_k is shorthand for $\mu_k^{(E_F)}$.

Assuming that the photon counts p_{ij} are Poisson random variables, the model shown in (3.6) follows a Poisson log likelihood function,

$$\begin{aligned}\mathcal{L}(\boldsymbol{p}\,;\,\boldsymbol{f},\boldsymbol{\mu}) = \sum_{i,j}\Big\{ p_{ij} \ln\Big[q''_{ij} f_i \exp\Big(-\sum_k L_{ijk}\mu_k\Big)\Big] \\ - q''_{ij} f_i \exp\Big(-\sum_k L_{ijk}\mu_k\Big)\Big\}.\end{aligned} \tag{3.7}$$

The Fisher information matrix, F, is given by the expectation of the negative Hessian matrix, which is a block matrix for joint problems similar to this one [137]:

$$F = E\{-H\} = \begin{pmatrix} E\{-\frac{\partial^2 \mathcal{L}}{\partial f_n \partial f_m}\} & E\{-\frac{\partial^2 \mathcal{L}}{\partial f_n \partial \mu_m}\} \\ E\{-\frac{\partial^2 \mathcal{L}}{\partial \mu_n \partial f_m}\} & E\{-\frac{\partial^2 \mathcal{L}}{\partial \mu_n \partial \mu_m}\} \end{pmatrix}, \tag{3.8}$$

which gives

$$F = \begin{pmatrix} \sum_j \frac{\bar{p}_{mj}}{f_m^2}\delta_{mn} & -\sum_j \frac{\bar{p}_{nj}}{f_n} L_{njm} \\ -\sum_j \frac{\bar{p}_{mj}}{f_m} L_{mjn} & \sum_i \sum_j \bar{p}_{ij} L_{ijn} L_{ijm} \end{pmatrix}. \tag{3.9}$$

The complete derivation of 3.9 can be found in Appendix C. Using the above method, we constructed F for the isolated, specific 2D iron object shown in Fig. 3.4 and for each of the detector geometries shown in Fig. 3.3. As with SVD analysis, a 2D object was chosen to study effects of detector arrangement in the plane perpendicular to pencil beam propagation, and therefore beam attenuation was not applicable. Fig. 3.4 displays the object used, which was a numerical 40×40 iron phantom meant to represent a geological sample. This phantom contained iron densities of 0.01, 0.70, and 1.05 g/cm^3 in a background of a carbon, oxygen, and silicon mixture, and each voxel was a square with side length 2 µm. Mean photon counts, $\bar{p}_{mj}$, were first calculated by simulating our forward model for each geometry without noise, utilizing a beam flux of $I_0 = 10^{18}$ photons/cm^{2}s, a beam time of 1s per line, and other physical factors outlined in Chapter 2.

Eigenvectors $\boldsymbol{h}_r$ and eigenvalues λ were computed for each F. Like the singular vectors of the imaging model, each eigenvector of F contain elements h_{rk} relating to both the metal and attenuation mapping, and must be split into metal density and attenuation components:

$$\boldsymbol{h}_r^f = [h_{r1}, h_{r2}, h_{r3}...h_{rN}], \tag{3.10}$$

and

$$\boldsymbol{h}_r^\mu = [h_{r(N+1)}, h_{r(N+2)}, h_{r(N+3)}...h_{r(2N)}]. \tag{3.11}$$

Each $\boldsymbol{h}_r^f$ and $\boldsymbol{h}_r^\mu$ was reshaped into a 2D array and displayed to examine patterns of pixels that can be estimated with varying precision for each detector arrangement. For visualization purposes, vectors were first normalized to unit length. For the eigenanalysis, F was assumed to be Hermitian; however for some detector geometries, a few eigenvalues were negative

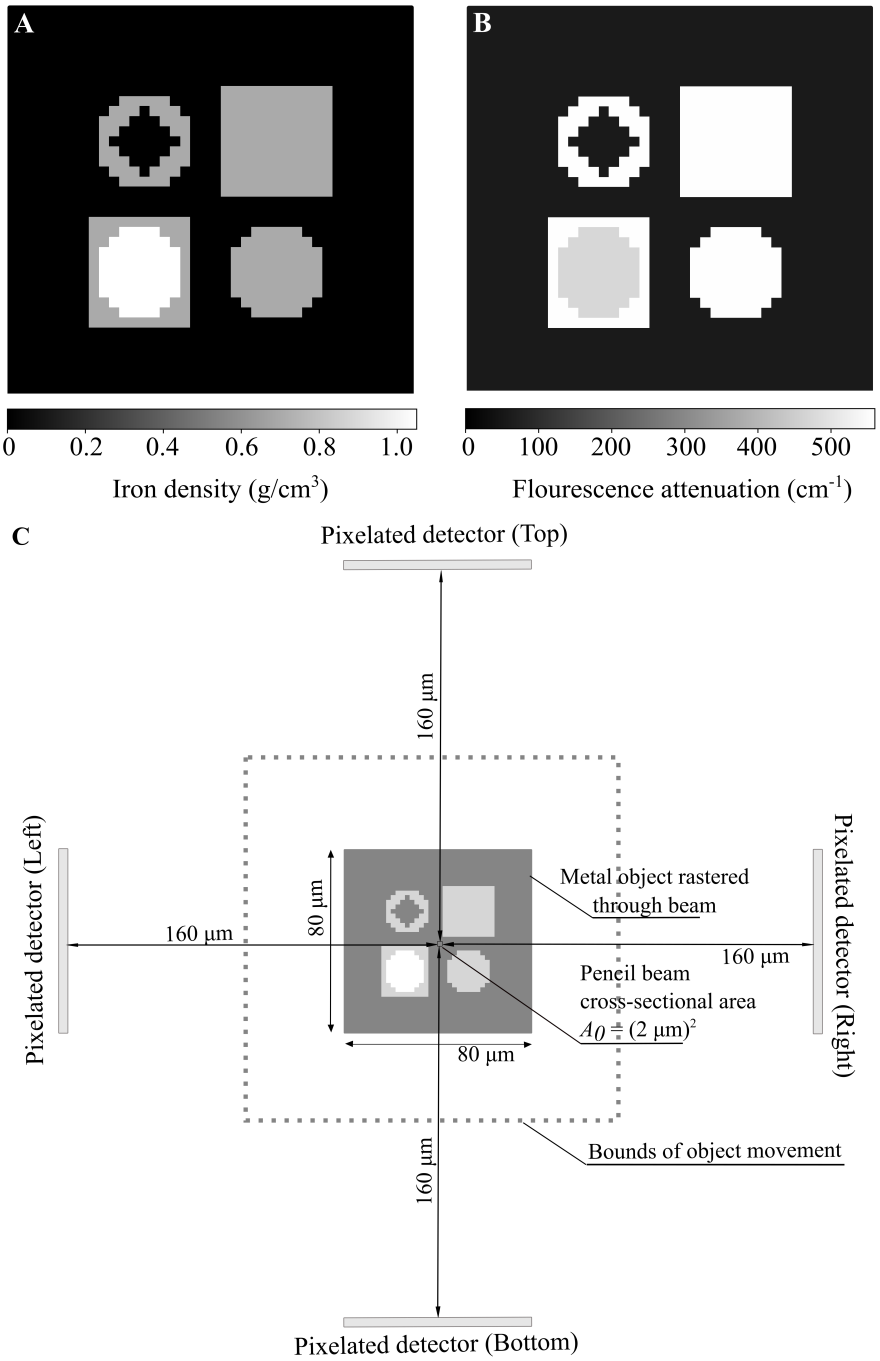

Figure 3.4: Iron numerical phantom used for Fisher information matrix study: A) iron density map of phantom, B) attenuation map of phantom at the K_{α_1} energy of iron (6.4 keV), C) four detector configuration and object support. Note that the pencil beam remains stationary at the isocenter and the object is rastered through the beam, within the bounds shown.

but small enough for this to be attributed to numerical precision. These small negative eigenvalues were artificially set to be 1×10^{-12} for the purposes of displaying eigenvalue spectra on a log scale.

3.2.2 Numerical simulations

In addition to the mathematical investigations, we performed image reconstructions of a 3D gold numerical phantom. This phantom had a 4 mm voxel size, on a 20×20×20 grid, which allowed for minimal computation time yet provided reliable results that are expected to apply to higher-resolution phantoms. The phantom contained gold densities of 0, 0.005, and 0.022 g/cm^3 in a soft tissue background, meant to represent a biological sample similar to those used in preclinical imaging. This gold phantom was similar to the iron phantom used in the FIM investigation in that both were adaptations of the phantom considered in Golosio et al. [128]. Physical factors for this gold phantom can be found in Chapter 2.

For XFET data collection, we performed a forward model simulation using (3.1) and adding in Poisson noise. This simulation was completed a total of five times per detector arrangement with different noise realizations in each simulation. We used a beam flux of $I_0 = 10^{12}$ photons/cm^{2}s and a 0.1 s exposure time per beam position. For simplicity, d_1 and d_2 were both 8 cm, and the slit width was 2 mm. Attenuation maps that were used for data simulation were constructed for a beam energy at the K-edge of gold, 80.7 keV, to ensure characteristic x-ray production. The fluorescence energy was therefore the gold K_{α_1} energy, 68.8 keV; attenuation coefficients at this energy were used for the fluorescent attenuation map.

To perform image reconstruction, we used our previously developed alternating approach, which is outlined in detail in Chapter 2. Briefly, this joint image reconstruction approach alternates between 1) updating the attenuation map with an iterative separable paraboloidal surrogates algorithm,

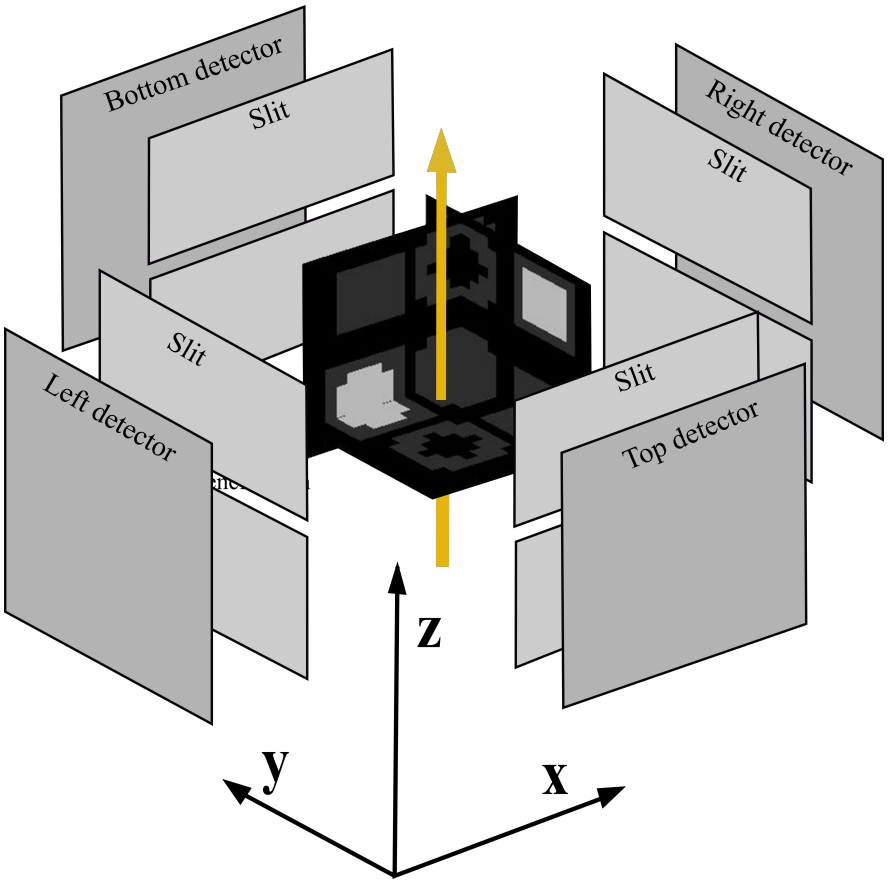

Figure 3.5: Orientation of four detectors around gold object used for numerical simulations (not to scale). ©2024 IEEE

$$\mu_k^{(n+1)} = \left[\mu_k^{(n)} + \left(\frac{\sum_m^{N_Y} L_{mk} q''_m f_m^{(n)} \exp\left(-\sum_{k''} L_{mk''}\mu_{k''}^{(n)}\right)}{\sum_{m=1}^{N_Y} L_{mk} L_m c_m^{(n)} + \beta \sum_{r=1}^{K} |c_{rk}| c_r w_r} \right.\right.$$
$$\left.\left. \frac{-\sum_m^{N_Y} L_{mk} p_m - \beta \sum_{r=1}^{K} c_{rk} w_r \sum_{k''=1}^{N} c_{k''r}\mu_{k''}^{(n)}}{\sum_{m=1}^{N_Y} L_{mk} L_m c_m^{(n)} + \beta \sum_{r=1}^{K} |c_{rk}| c_r w_r} \right)\right]_+, \tag{3.12}$$

(where $[]_+$ enforces non-negativity), and 2) updating the metal density map with a closed-form solution,

$$\hat{f}_i^{(n+1)} = \frac{\sum_j p_{ij}}{\sum_j q''_{ij} \exp\left(-\sum_k L_{ijk}\mu_k^{(n+1)}\right)}. \tag{3.13}$$

In (3.12) and (3.13), the index m is a linear combination of indices i and j. Derivation of the closed-form solution are given in Appendix A and additional term definitions are given in the List of Mathematical Symbols. As in Chapter 2, this iterative algorithm assumed an unknown beam attenuation map by using Equation 2.22 for every q''_m term in (3.12). After empirically optimizing our penalty factor β to 1E$-$4, (this penalty term applied only to the attenuation portion of the estimate), we alternated between (3.12) and (3.13) until the root mean square relative change in the density map fell below 5E$-$4:

$$\sqrt{\frac{\sum_i \left(f_i^{(n+1)} - f_i^{(n)}\right)^2}{\sum_i \left(f_i^{(n)}\right)^2}} < 0.0005. \tag{3.14}$$

We completed this joint image reconstruction for four detector geometries, each of which utilized a different combination of the four detectors shown in Fig. 3.5. The "one-detector" geometry used only the left detector. The "two-parallel-detector" geometry used the right and left detector, and the "two-orthogonal-detector" geometry used the left and top detector. Finally, the "four-detector" geometry used all four detectors.

We compared the resulting reconstructions from each of the four detector arrangements. These comparisons were made qualitatively by comparing the resulting metal and attenuation

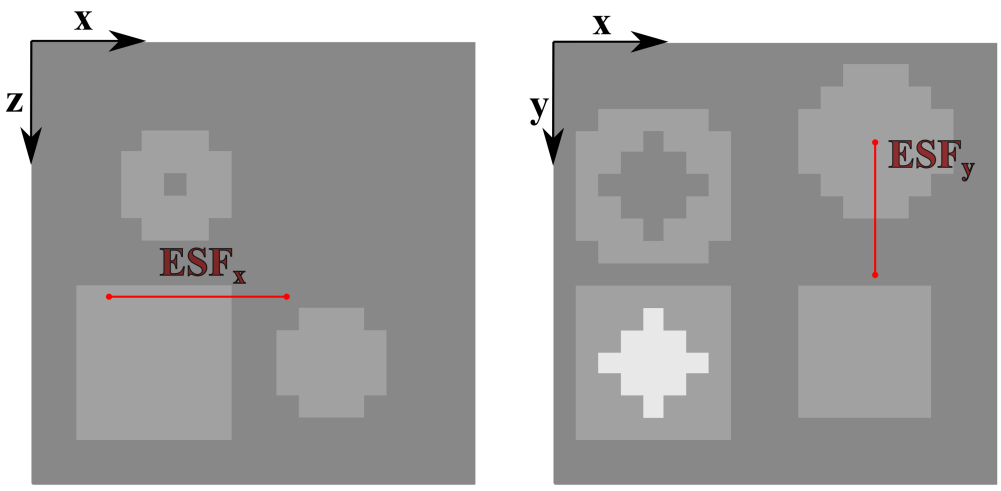

Figure 3.6: Select slices through the xz plane (left) and xy plane (right) of gold object, displaying how ESFs were sampled. ©2024 IEEE

maps, and quantitatively by computing the normalized root mean square error (NRMSE) for each map. Qualitative images of the metal and attenuation reconstructions are shown with the orientation displayed in Fig. 3.5. We also report attenuation factor maps consisting of the average attenuation factor, $\exp(-\sum_k L_{ijk}\mu_k)$, seen by all detectors for a given object voxel; these attenuation factor maps were compared to expected maps for each detector geometry.

Finally, we perform the above-described image reconstruction for noiseless data to obtain a quantitative measure of spatial resolution. We extract x and y line profiles through the attenuation map across the edge of a gold structure within the image. The method of sampling these edge spread functions (ESFs) can be seen in Fig. 3.6. After doubling the spatial resolution of the ESFs with linear interpolation, we fit them with an error function parameterized by σ, which indicates the degree of blurring [155]. We report σ values in the x- and y-dimension for each detector arrangement.

3.3 Results

3.3.1 SVD

Figure 3.7 displays right singular vectors corresponding to the density and attenuation maps, reshaped into 2D arrays. These singular vectors span the space of recoverable objects when the data have no noise and we use no priors. Singular vectors are presented for all four detector geometries, and their corresponding singular value spectra are also displayed above; the singular values indicate how well these vectors are preserved in the XFET imaging system. The singular vectors are constructed with a pixel basis and are normalized for display with a gray-value color scheme. The extremes of the color scheme, i.e. black and white, highlight the directions of greatest magnitude within the vector. The combination of pixels displayed with the greatest magnitude (black or white) displays the vector either well- or poorly preserved in imaging, depending on the magnitude of the associated singular value. These patterns of metal and attenuation pixels indicated by the singular vectors vary with detector geometry.

The singular value spectrum associated with a four-detector geometry has the smallest condition number; likewise, the spectrum for one detector arrangement has the largest. The last 500 singular values of the one-detector spectrum trend downward two orders of magnitude, indicating poor conditioning. However none of the spectra contain zero singular values (within numerical precision), indicating that null spaces do not exist for these discrete-to-discrete models.

Four detectors

Singular vectors corresponding to large singular values appear as a broad uniform area across the object plane. The singular vectors associated with smaller singular values appears as high-frequency checkerboard patterns in both the metal and attenuation maps. The vectors

associated with the smallest singular value appear as broad central metal and attenuation regions, both containing high-frequency pixel patterns in the four corners of the square object.

Two parallel detectors

Singular vectors corresponding to large singular values appear as a broad uniform area in the center of the object, with attenuation pixels equidistant to both left and right detectors. The attenuation vector corresponding to the smallest singular value appears as a high spatial frequency in the x-axis.

Two orthogonal detectors

Singular vectors corresponding to large singular values again appear as a broad uniform area in the center of the object, but the attenuation portion of the vector has a preferential orientation; the uniform area is concentrated in the region of object space that is close to the left and top detectors. The vectors associated with the smallest singular value (which trends down two orders of magnitude) show a high-frequency pixel pattern in the furthest corner from the two orthogonal detectors.

One detector

Singular vectors corresponding to large singular values appear as a broad uniform area across object space, with attenuation pixels close to the one-sided left detector. The vector corresponding to the smallest singular value appears as a high-frequency pattern oriented perpendicularly to the detector, far from the detector.

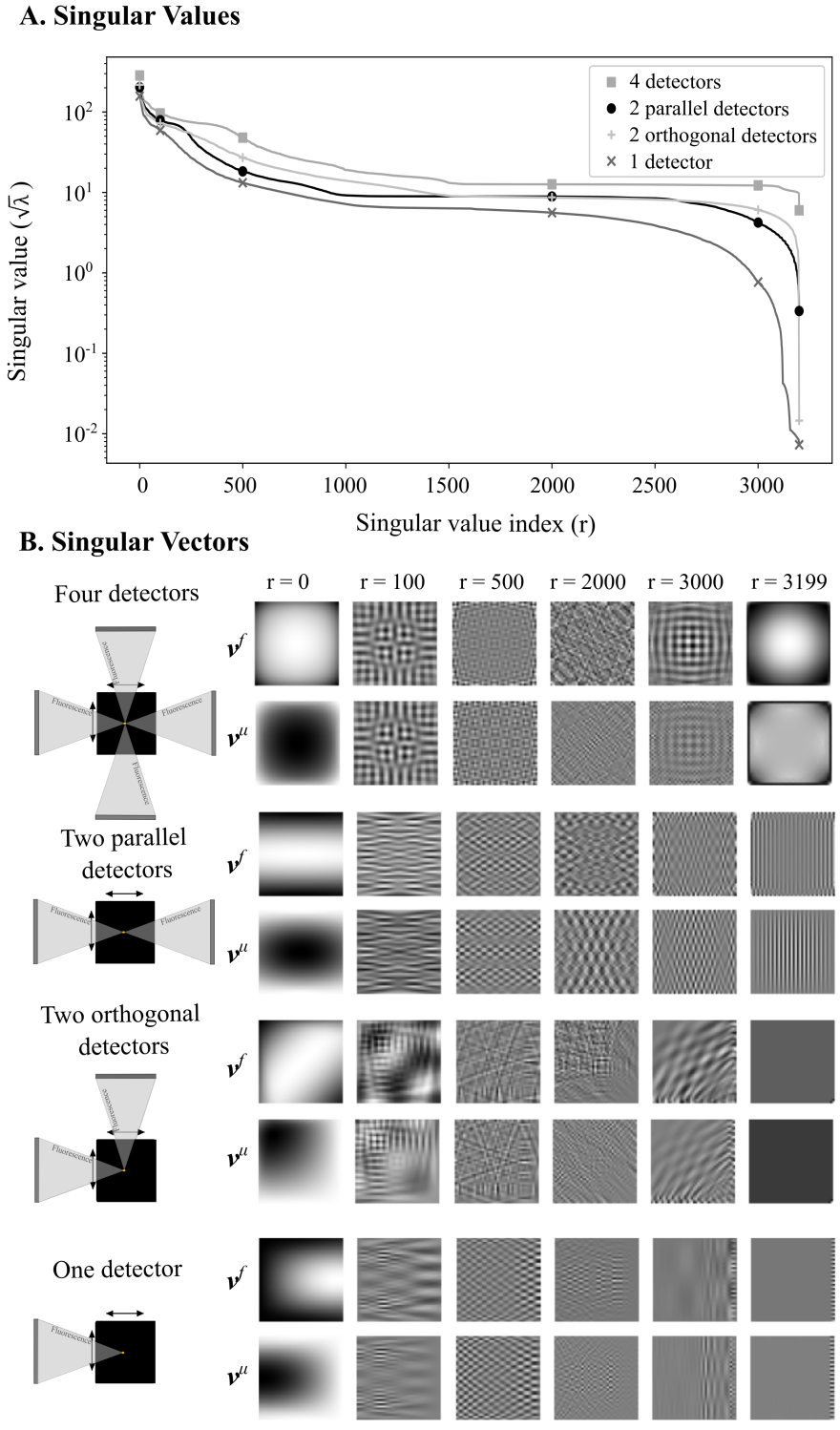

Figure 3.7: Singular value decomposition for various detector arrangements. A) Singular value spectra for the four detector geometries, with sampled singular values indicated with markers, and B) metal and attenuation portions of singular vectors associated with sampled singular values, with schematics of their associated detector geometries. ©2024 IEEE

3.3.2 FIM

Figure 3.8 displays eigenvalue spectra from Fisher information matrices associated with the four detector geometries. This figure also contains a sample of eigenvectors associated with the marked eigenvalues.

The eigenvalue spectra in Fig. 3.8 appear with step-like behavior. For descriptive purposes, we can separate these eigenvalues into three bins: first, "large" eigenvalues are around or above 10^{10} in value. "Moderate" eigenvalues are categorized to be between 10^4 and 10^7, and "small" eigenvalues are below 10^1. For all detector geometries, the eigenvectors corresponding to large eigenvalues appear as one or a few metal pixels and attenuation map "fans" spanning from the selected metal pixel(s) to the detector(s). For a given detector geometry, the subset of metal eigenvectors corresponding to large eigenvalues span the set of all pixels that have low amounts of metal. Similarly, eigenvectors corresponding to moderate eigenvalues also appear as one, two, or a few metal pixels and the corresponding attenuation fans. However this set of metal vectors span the set of pixels containing *dense* metal. Finally, eigenvectors corresponding to small eigenvalues appear as complex patterns and spatial frequencies across object space. Generally, as eigenvalue decreases, the spatial frequency of the associated vector increases. The metal portion of the eigenvector is always bounded by the region in object space containing dense metal. However, different detector geometries resulted in vectors with different patterns in object space:

Four detectors

The metal vector associated with the smallest eigenvalue displays pixels containing dense metal. This vector is coupled with an attenuation vector containing pixels in the four corners of the object. As eigenvalue increases, more complex spatial frequencies in multiple directions appear in the metal and attenuation eigenvectors.

Two parallel detectors

The attenuation spatial frequency associated with the smallest eigenvalue is along the x-axis.

Two orthogonal detectors

The spatial frequency pattern in the attenuation map seen for two parallel detectors is not present for two orthogonal detectors; pixels far from the two detectors are illuminated in vectors corresponding to small eigenvalues.

One detector

In both the attenuation and metal map, high spatial frequencies normal to and far from the one-sided detector are associated with small eigenvalues.

3.3.3 Numerical simulations

Figure 3.9 displays the joint metal and attenuation reconstructions resulting from various detector geometries, alongside the true metal and attenuation maps. Figure 3.10 displays NRMSE values associated with metal maps, attenuation maps, and attenuation factor maps (not shown). As seen in Fig. 3.9, voxels far from one detector are underestimated in the metal map, resulting in an underestimation in the attenuation map in these distant regions, and an overestimation in the pixels close the detector. There is also a slice of the one-detector attenuation map, appearing as a dark vertical band in Fig. 3.9 that was not probed by fluorescence emissions with the use of one detector and is severely underestimated. Likewise, pixels far from the two orthogonal detectors are also underestimated, but compared to the reconstruction from one detector, have improved spatial resolution in the x-axis. In the attenuation map for two parallel detectors, we see blurring in the x-axis. However, compared to two orthogonal detectors, two parallel detectors offers better qualitative performance in

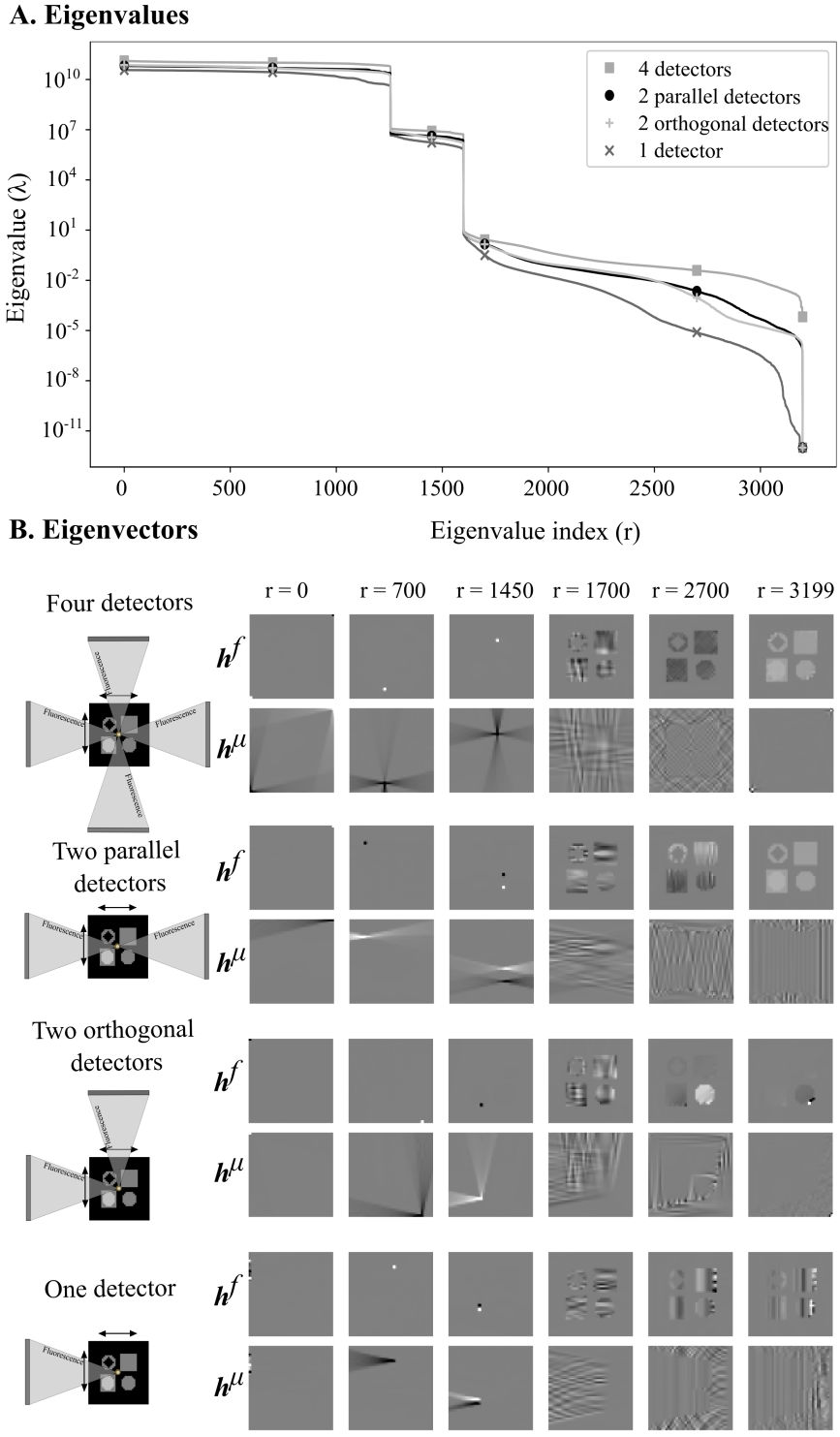

Figure 3.8: Fisher information matrix eigenanalysis for various detector arrangements. A) Eigenvalue spectra for the four detector geometries, with sampled eigenvalues indicated with markers, and B) metal and attenuation portions of eigenvectors associated with sampled eigenvalues, with schematics of their associated detector geometries. ©2024 IEEE

the attenuation factor map reconstructions, as seen in Fig. 3.9, and has lower NRMSE values associated with attenuation and metal map reconstructions. Four detectors offers the most accurate metal and attenuation map reconstruction, qualitatively (as seen in Fig. 3.9) and quantitatively (as shown in Fig. 3.10). The anisotropic blurring observed in the two-parallel-detector case in Fig. 3.9 is also observed quantitatively in Fig. 3.11. The use of either two parallel detectors or one detector results in decreased spatial resolution along the x-axis, evident through substantially increased σ values. Differences in y-axis resolution between all detector arrangements were less pronounced than differences seen in the x-axis.

3.4 Discussion and Conclusions

SVD analysis reveals which vectors are well preserved in imaging, which vectors might be difficult to recover, and any null space present. SVD did not reveal a null space for these discrete-to-discrete models. The lack of null space is not surprising, given that the number of observations, NM, is much larger than the number of unknown object pixels, $2N$. In a more realistic continuous-to-discrete model, there would certainly be a null space. However, especially for the case of one-detector and two-orthogonal-detector geometries, the lowest 500 singular values trend downward two orders of magnitude indicating ill-conditioning and difficulty recovering some object vectors. The singular vectors corresponding to these low values for a one-detector geometry were groupings of high spatial-frequency metal pixels coupled with attenuation pixels, both far from the detector. These results indicate that metal and attenuation pixels far from the detector are least preserved in imaging, and distant high spatial frequencies may be difficult to reconstruct. Similarly, vectors corresponding to the lowest singular values for two orthogonal detectors display metal and attenuation pixels far from the two detectors, indicating that these pixels may be lost in imaging, or difficult to reconstruct. XFET does not probe all areas of an object equally: the frequency at which x-ray fluorescence will pass through various regions of the object strongly depends

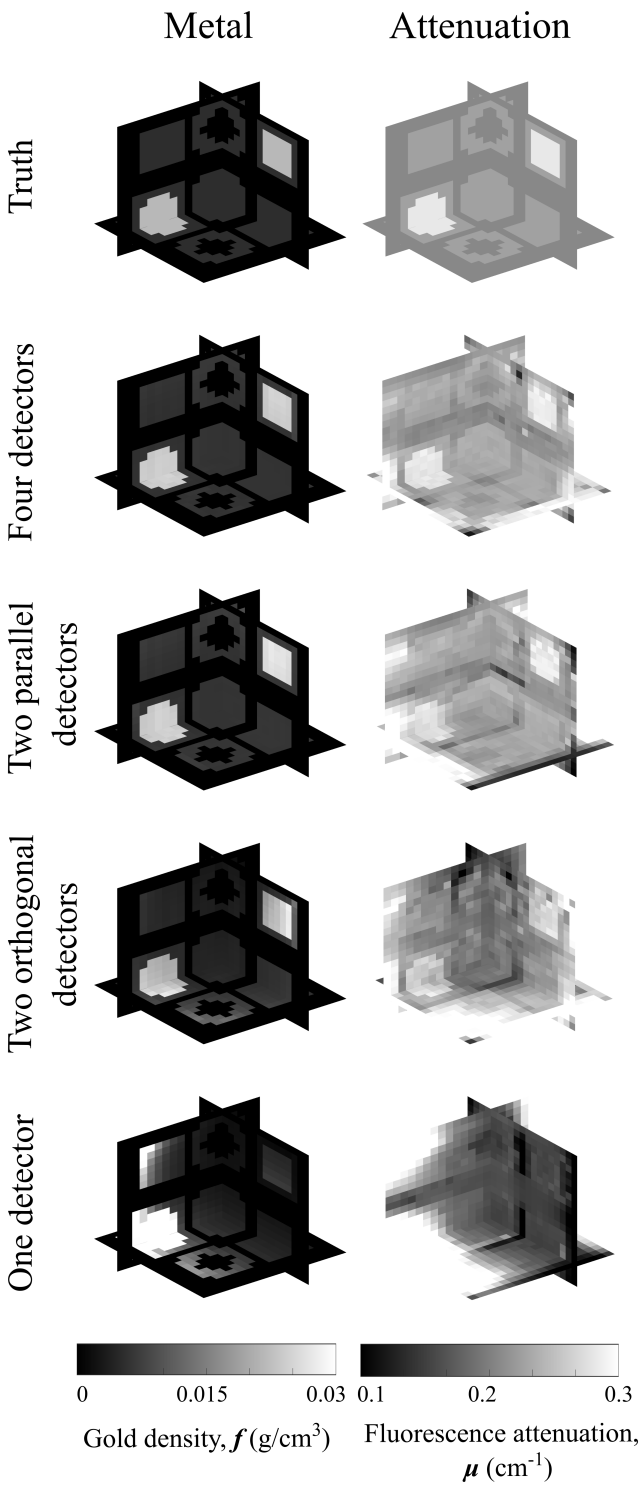

Figure 3.9: Gold map and attenuation map reconstructions for various detector geometries. ©2024 IEEE

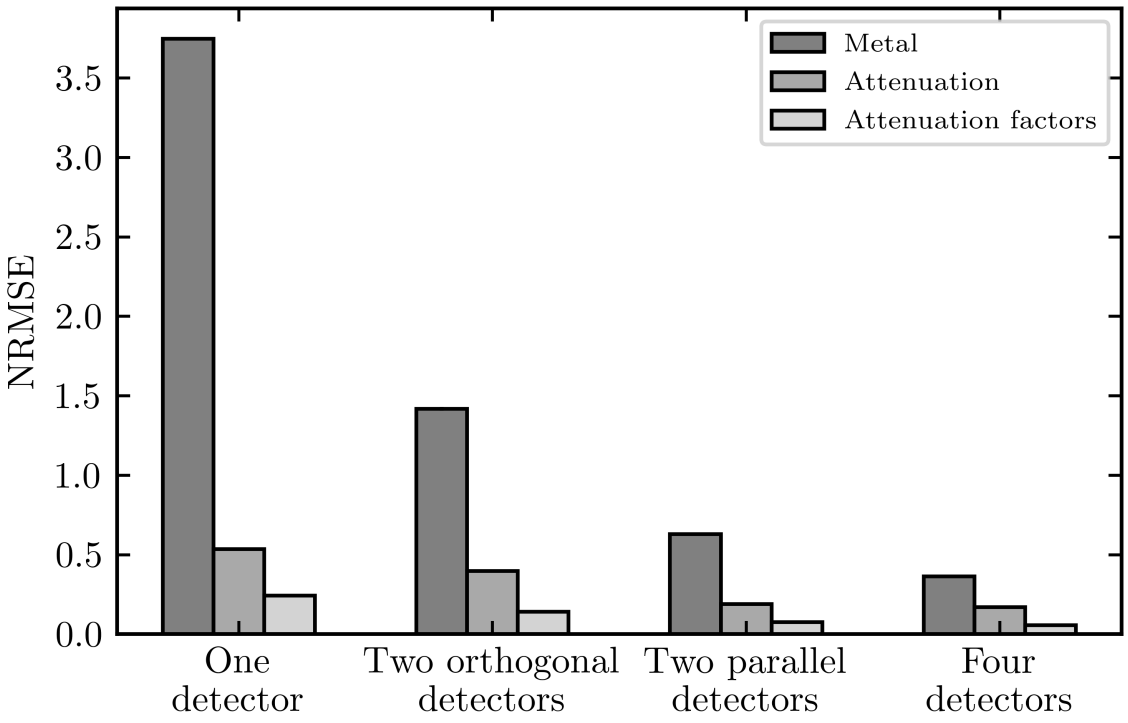

Figure 3.10: Normalized root mean square errors resulting from joint reconstructions with various detector geometries. Error bars, showing the standard deviation of NRMSE values resulting from 5 reconstructions from data with different noise realizations, are present but too small to be visible.

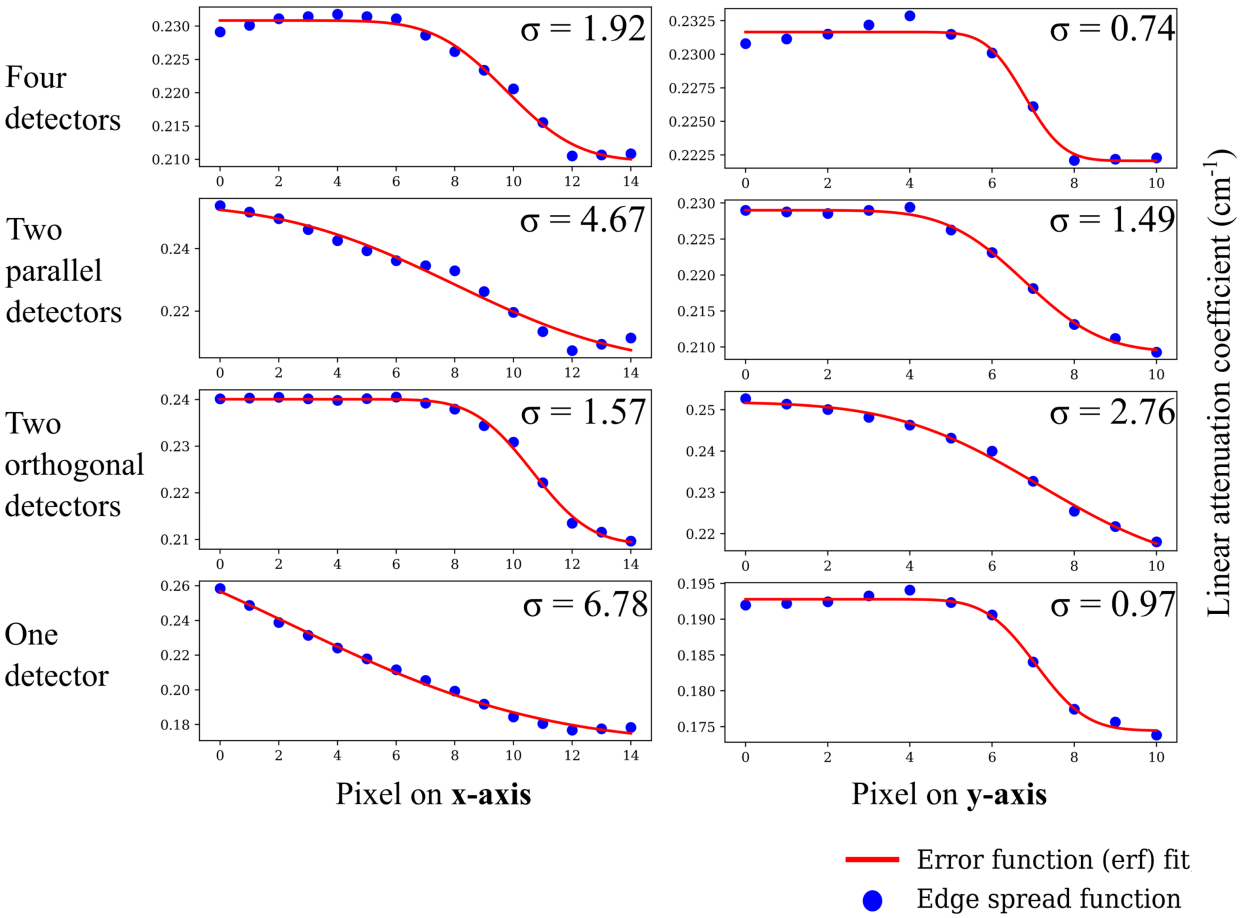

Figure 3.11: Attenuation map spatial resolution measurements, including edge spread function in x (left) and y (right) dimension, and error function fit. Greater sigma values indicate greater blurring and decreased spatial resolution. ©2024 IEEE

on the object's spatial distribution of metal. Distant metal pixels, which suffer from highly attenuated fluorescence emission, are coupled to their attenuation pixel counterparts, which suffer from infrequent fluorescent probing. Therefore, distant pixels are expected to be poorly preserved in imaging.

The two-parallel and four-detector geometries had the largest singular values. Within the two-parallel-detector geometry, the vector most difficult to recover was a high spatial frequency in the attenuation map oriented along the x-axis. The four-detector geometry results in the singular value spectrum with the smallest condition number, indicating that this geometry has the best-conditioned inverse. Surprisingly, the vectors associated with the lowest four-detector singular value display fairly uniform metal and attenuation maps. However, these vectors display high-frequency pixel patterns in the four corners of the object that cannot be seen easily.

For all detector geometries, singular vectors corresponding to large singular values appear as broad uniform areas across object space, indicating that low spatial frequencies, usually equidistant from the detectors, are well preserved in imaging.

In the above SVD analysis, a sufficiently small q'_{ij} would amplify noise in the transformed data that might overpower the small differences considered in the SVD spectra. However, a small q'_{ij} would usually result from the pencil beam being attenuated to a degree that reaches the limit of our ability to see any further in the object. In the present case, q'_{ij} factors were large due to the magnitude of the beam intensity, I_0, and therefore this factor did not amplify noise in the transformed data.

In this chapter, the Fisher information matrices were ill-conditioned, with condition numbers greater than 10^{15} for all detector arrangements. Therefore, inversion of the FIM was not reliable and the Cramer-Rao lower bound was not computed. However the eigenanalysis of the FIM provided insight into the information content of data given by various pixel and detector arrangements, and was consistent with the results of SVD analysis.

The FIM eigenvalue spectra contain notable step-like behavior; in Sec. 3.3.2, we separated eigenvalues into "large", "moderate" and "small" bins to aid in the discussion of these steps. For all detector geometries, metal FIM eigenvectors associated with large and moderate eigenvalues appeared as a pixel basis, with some vectors having two or a few illuminated pixels. These metal vectors were accompanied by attenuation "fans" spanning out from the emission pixel to the detector(s). This pattern mimics the 2D XFET imaging process that illuminates one pixel at a time, where fluorescence emitted from this pixel probes only a fan-shaped portion of the attenuation map that lies between that emission pixel and the detector(s). The difference between the vectors associated with "large" and "moderate" eigenvalues is displayed in Fig. 3.12: the set of vectors associated with large values spans the set of pixels containing low density metal, while the vector set associated with moderate values spans the set of pixels containing dense metal, suggesting low density metal pixels can be estimated with more precision. This counter-intuitive result could be due to the Poisson nature of the collected photons: low-metal pixels produce fewer photon counts with a lower variance associated with the measurement.

Eigenvectors corresponding to "small" eigenvalues appear as intricate patterns and spatial frequencies across object space. Because this region of the eigenvalue spectra declines by several orders of magnitude, this result informs about the limits of spatial resolution of our imaging system. As previously mentioned, when eigenvalue increases within this region, spatial frequency of the corresponding vector decreases, indicating that low spatial frequencies can be estimated with lower uncertainty than high spatial frequencies. The orientation of these frequencies depends on the detector geometry: when using two parallel detectors, the vector associated with the most variance in the estimation task appears as a high spatial frequency oriented along the x-axis. The use of one detector shows a similar spatial-frequency pattern in its lowest-value eigenvector, with a concentration of activity in pixels far from the detector. This one-dimensional spatial frequency pattern disappears in the lowest-value

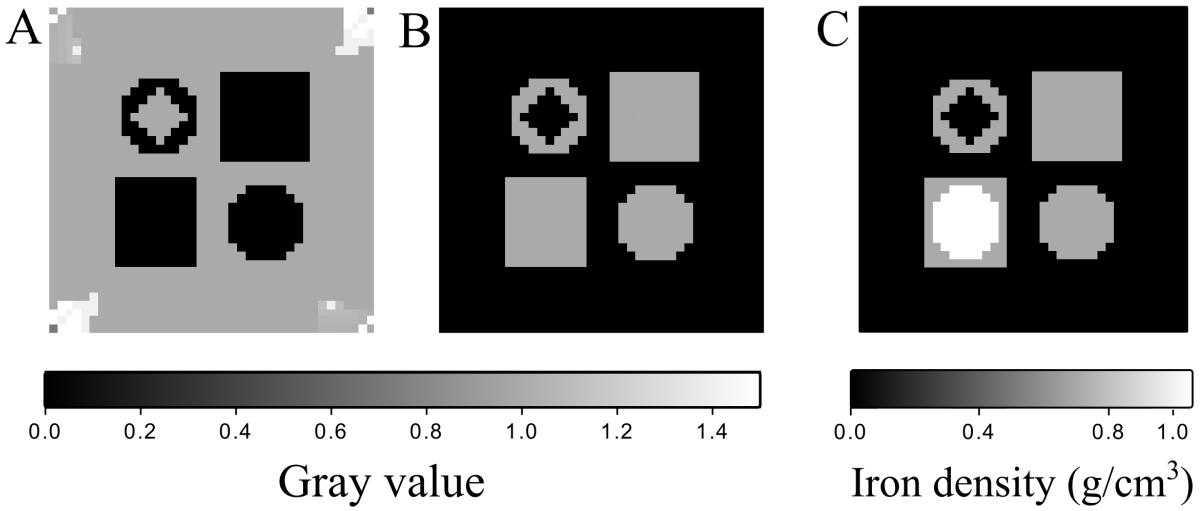

Figure 3.12: Sum of the absolute value of all FIM eigenvectors associated with A) large eigenvalues, and B) moderate eigenvalues, for the four-detector geometry. C) True iron object used for FIM analysis, displaying iron density per pixel. Large-eigenvalue eigenvectors span the set of pixels containing low density metal, while the moderate-eigenvalue eigenvectors span the set of pixels containing dense metal.

vectors for two-orthogonal and four-detector geometries. These results suggest that the use of orthogonal detectors results in spatial frequencies along the x-axis that can be estimated with more precision.

Image reconstructions in Fig. 3.9 and NRMSEs in Fig. 3.10 provide information about image reconstruction accuracy for various detector arrangements. First, in the one-detector geometry, voxels far from the detector are underestimated in both the attenuation and metal map. These distant voxels are not easily recovered. The vertical slice of the attenuation map that is not probed by fluorescence is underestimated and reveals the importance of placing detectors such that the entire object is probed. Voxels far from the two orthogonal detectors are also not easily recovered, and Fig. 3.9 shows the metal density map is underestimated in these distant regions. However, ESFs in Fig. 3.11 reveal that this detector arrangement offers substantially improved attenuation spatial resolution in the x-axis. Alternatively, the use of two parallel detectors results in attenuation maps that are blurred along the x-axis,

confirming the difficulty in recovering high spatial frequencies in this dimension.

The measurements in Fig. 3.11 are object-specific and their absolute values are not proven to be general properties of the studied arrangements. Object differences may account for the rotation variance in resolution for the 4-detector arrangement. However, relative resolution differences along one axis between detector arrangements are not due to object differences. Resolution differences in the x-axis were substantially more pronounced than in the y-axis and were consistent with the qualitative observations seen in Fig. 3.9.

Regardless of attenuation spatial resolution, the use of two parallel detectors offers better quantitative accuracy in the metal, attenuation, and attenuation factor map reconstructions compared to the use of two orthogonal detectors. Attenuation map accuracy is desirable but not required; attenuation maps are nuisance parameters serving mainly as critical pieces of information needed to reconstruct accurate metal density maps. Because two parallel detectors outperform two orthogonal detectors in the attenuation factor map accuracy, we also see a subsequent improvement of metal map accuracy, qualitatively and quantitatively. Two parallel detectors offer similar qualitative and quantitative performance to the use of four detectors in the task of metal map reconstruction.

Unsurprisingly, four detectors offer the best overall performance qualitatively and quantitatively, partially due to increased isotropic spatial resolution. However in a preclinical or clinical context where the use of four detectors is not feasible, two parallel detectors offer similar performance in reconstructing accurate metal maps despite the loss of x-axis spatial resolution in the attenuation map.

The four-detector arrangement has naturally twice the sensitivity of a two-detector arrangement: for a constant radiation dose level, doubling the number of detectors doubles the number of detected fluorescent x-rays. The question arises of how much the increased signal-to-noise (SNR) ratio associated with four detectors improves the image reconstruction accuracy. To explore the possibly confounding effect of SNR, we performed additional sim-

ulations at varying beam intensities (SNRs) using four-detector and two-parallel-detector geometries. The resulting NRMSEs are reported in Fig. 3.13. Note that NRMSEs are plotted against total number of detected photons such that for a given number of detected photons, the two-detector arrangement implicitly has twice the beam intensity as the four-detector arrangement. Across the range of SNRs in Fig. 3.13, four detectors offers lower NRMSEs than two parallel detectors. This degree of error improvement is slight for the attenuation map but larger for the metal map. Trends in Fig. 3.13 suggest that for greater detected photon counts, image reconstruction accuracy plateaus as NRMSE becomes dominated by bias contribution. In this regime, the differences in image reconstruction accuracy between detector arrangements is not due to differences in SNR. The growing NRMSEs at lower counts suggest that with more noise-dominated data, image reconstruction accuracy will decline. This decline is consistent with the expected result of FIM eigendecomposition: the FIM eigenvalue spectra scale with detected counts, as would the variance components of the NRMSEs in a less bias-dominant regime.

Limitations of this chapter include the use of a monochromatic beam for 3D data simulations and the lack of consideration of scatter. As discussed in Chapter 2, low-energy monochromatic beams have been used for XFCT in benchtop settings [123], and we have previously performed XFET imaging with monochromatic synchrotron radiation [122]. The purpose of this optimization study was to understand how the placement of detectors impacted image reconstruction accuracy and image quality; the findings will translate to the case where a polychromatic beam is considered. Nevertheless, polychromatic beams at energies necessary to cause K-fluorescence in gold and iron will be considered in our future work. Second, despite the use of energy-sensitive detectors and slit collimators, our preliminary studies have still shown scatter in our system to be non-negligible. Because scatter will contaminate all photon measurements relatively equally, it will likely impact global but not relative image reconstruction accuracy. Therefore, we expect the conclusions drawn from

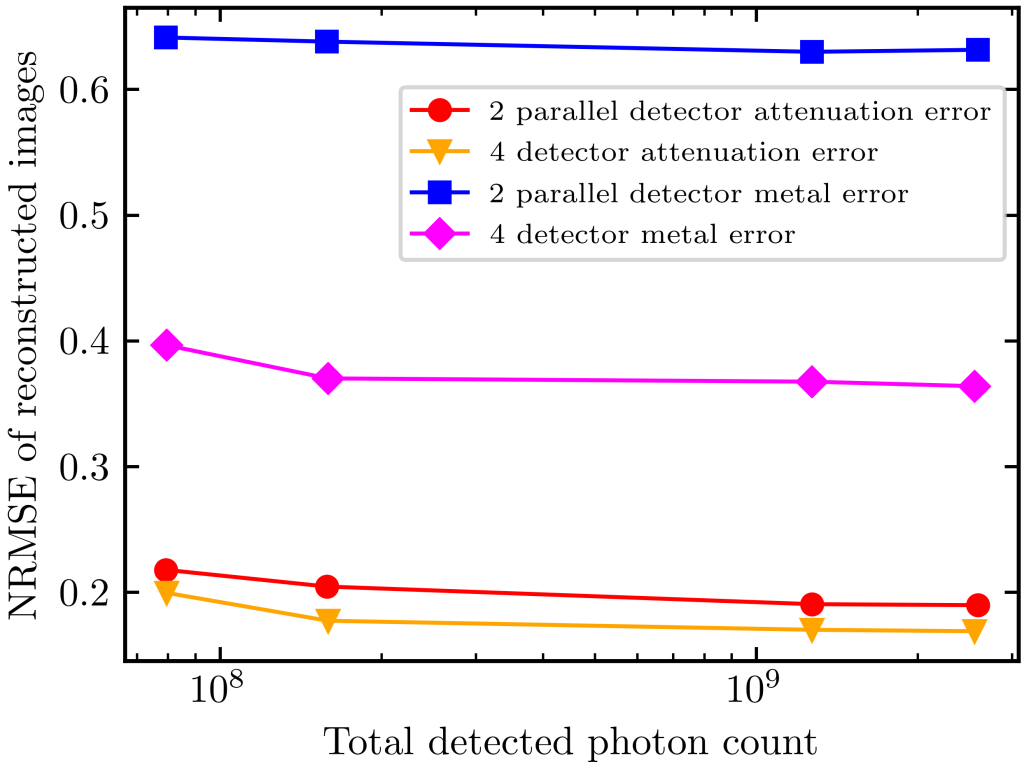

Figure 3.13: NRMSE values resulting from joint reconstructions at varying detected photon counts. ©2024 IEEE

this study, namely the impact of detector arrangement on relative image reconstruction accuracy and spatial resolution, to hold true even in the presence of scatter. Future studies will include modeling scatter with Monte Carlo simulations to validate the results of this chapter. Finally, we acknowledge that both the FIM investigation and image reconstructions were object specific and may not be generalizable; this is a subject for future investigation. However, the SVD investigation was general and not object specific, and results of SVD analysis were consistent with findings from FIM and image reconstruction analysis: for example, finding that the use of two parallel detectors leads to a better conditioned inverse problem than the two orthogonal detectors, but resulted in loss of anisotropic spatial resolution.

Although the low-resolution phantom used for image reconstruction was simplistic for demonstrating a clinical scenario of nanoparticle mapping, the results of the present study have implications for future cancer treatment guidance with XFET. Most significantly, the difference in anisotropic resolution found between the various detector orientations is critical in choosing adequate detector placement in nanoparticle mapping. If high spatial resolution along one axis was necessary in future clinical contexts, the use of two carefully placed orthogonal detectors would offer the greatest spatial resolution. If the clinical task calls for mapping nanoparticles at greater depths, such as in prostate cancer, then two parallel detectors would be preferred to obtain the greatest signal and sensitivity.

Additionally, our future work will include a quantification of lowest detectable gold concentration for these various imaging geometries. While this future study will give insight into the sensitivity limits associated with the use of limited detectors, the present work was designed to examine spatial resolution and metal quantification accuracy for a fixed metal concentration. Both of these investigations are critical for XFET's translation to preclinical and clinical studies.

In summary, this chapter performed mathematical investigations into the effect of detector placement and number on image quality and performance of XFET imaging. Through

performing eigendecomposition of the FIM and SVD of the XFET linear imaging model for four distinct detector geometries, we found that the use of parallel detectors results in poorly preserved attenuation spatial frequencies along the x-axis. The use of orthogonal detectors, either two or four placed around the object, provides greater information about high spatial frequencies along this axis. Using a previously developed joint image reconstruction algorithm on a gold numerical phantom, we found that the use of two parallel detectors worsened the x-axis spatial resolution in the attenuation map, which was consistent with results from our mathematical investigations. However, despite the resulting anisotropic spatial resolution in the attenuation map, two parallel detectors still gave more accurate metal and attenuation factor maps. Because obtaining accurate metal maps is the main aim of XFET, two parallel detectors can be seen as superior to two orthogonal detectors in this task. Four detectors gave the best overall performance and image reconstruction accuracy, but performed similarly to two parallel detectors for these metrics. Most significantly, this chapter has shown that if the use of four detectors (or a full ring geometry) were not feasible in a clinical context, two parallel detectors would suffice so long as sensitivity was not a limiting factor. Therefore, this study gives insight into how metal quantification accuracy and spatial resolution is impacted by the use of a limited number of detectors: a critical investigation for the translation of XFET into preclinical contexts where detector geometry may lack flexibility.

CHAPTER 4

CONTRAST-TO-NOISE RATIO COMPARISON BETWEEN XFET AND CT

4.1 Introduction

In previous chapters, we have worked on advancing XFET towards preclinical imaging by exploring methods into image reconstruction, attenuation correction, and detector optimization. However, it is necessary to establish proof of benefit before XFET can be translated into these spaces. Specifically, a comparison to more conventional imaging modalities such as energy-integrating CT (EICT), or clinically emerging modalities such as photon-counting CT (PCCT) would demonstrate XFET's preclinical and clinical advantages.

4.1.1 XFET spectral resolution and partial field-of-view imaging

As discussed in previous chapters, XFET utilizes slit or pinhole apertures coupled to spatial- and energy-resolving detectors. Most recently, benchtop XFET has utilized High Energy X-ray Imaging Technology (HEXITEC) CdTe detectors [124]. These detectors count and assign energies to detected fluorescence photons with an improved full energy spectrum resolution of 1 keV at an energy relevant to this chapter [157]. High spectral resolution is necessary for fluorescence imaging to separate the fluorescence signal from Compton scatter contamination; the 1 keV energy resolution also allows XFET to simultaneously distinguish among many different metals of interest, each of which have distinct fluorescence energies. These metals may be distinguishable with state-of-the-art photon-counting CT, but may appear identical on a conventional, energy-integrating CT. XFET's mechanism of direct imaging also allows for partial field-of-view (FOV) or region-of-interest (ROI) imaging, making it potentially more dose-efficient than conventional XFCT which typically requires a nearly full sinogram acquisition to view the same region [158].

4.1.2 Previous comparisons of XFCT to CT

Previous studies have compared XFCT to CT in the task of achieving high contrast in metal regions and, under some conditions, have shown that XFCT outperforms CT in this task. Some studies have used variations of XFCT that incorporate a cone beam with a flat-panel photon-counting detector and pinhole collimation. One group demonstrated the feasibility of such geometry by imaging Gd solutions with concentrations as low as 2 mg/mL [114] and showed that their system outperformed CT in producing greater contrast-to-noise ratios (CNR) of Gd inserts and achieving lower Gd detection limits [119]. Another study that used a similar XFCT system to map GNPs in vivo demonstrated enhanced sensitivity and specificity of GNP detection compared to CT [95]. Other groups have compared conventional XFCT to K-edge CT both analytically and in simulation [107, 159]. These studies have consistently found that XFCT produced greater CNRs than K-edge CT at GNP concentrations below 0.4% by weight [107, 159]. It remains to be seen how the sensitivity between CT and XFET compares under various gold concentrations and imaging conditions.

XFET's primary limitation is imaging depth. This limitation arises not only from the depth of its pencil beam penetration in tissue, but also from the attenuation of the induced fluorescence x-rays. This limitation is also present and potentially more limiting in XFCT; due to its full sinogram requirement, the fluorescent signal may extinguish during certain portions of the object rotation and sinogram collection [160]. Both XFCT and XFET are limited to applications in either preclinical studies or superficial clinical studies. However, because XFET signal diminishes with increasing beam depth, it is important to quantify the depth conditions under which XFET will be outperformed by CT.

4.1.3 Chapter summary

In this chapter[1], we provide the first comparison of XFET and CT, and we characterize the conditions under which XFET outperforms CT, considering both energy-integrating and photon-counting detectors. We use Monte Carlo and raytracing simulations to compare the three imaging modalities for two phantoms. A Mouse Whole-Body (MOBY) digital phantom [162] containing various gold concentrations in different tissues, was used to demonstrate the feasibility of XFET in a preclinical context. Another numerical phantom was designed to test the effect of beam depth and gold concentration on CNR and to quantify the detection limit of XFET. XFET's ability to image partial FOVs is also demonstrated. The results of this study inform about the depth and sensitivity limits of XFET compared to other photon-counting and conventional imaging modalities and guide discussion about potential clinical and preclinical applications of XFET.

4.2 Methods

We compared the performance of simulated XFET and CT in the task of detecting regions of low concentrations of gold nanoparticles. Two phantoms were used: (1) a realistic digital mouse phantom (MOBY) containing gold in the kidneys, a hind leg tumor, and various other organs; and (2) a cylindrical soft tissue phantom containing spheres of varying gold concentrations. XFET and CT simulations were designed to be approximately dose-matched and comparable in physical scale, as described in the following sections.

4.2.1 XFET scanner design and Monte Carlo parameters

Figure 1.2 displays XFET's mechanism of direct imaging. A collimated x-ray source illuminates a line within the phantom. Provided that the x-ray pencil beam contains x-rays with

1. This chapter is based in part on a study reported in [161].

energies above the K-edge of the metal of interest, metal atoms along the line of illumination interact with those x-rays primarily through the photoelectric effect and subsequently emit x-ray fluorescence. X-ray fluorescence photons that are emitted from a point on the line are directly detected by the pixelated, energy-sensitive detector plane after passing through a slit aperture of width w. As the phantom is rastered through the stationary pencil beam, a metal map is formed directly without need for tomographic image reconstruction.

Despite the simplified XFET diagram in Fig. 1.2, the XFET imaging system used in this chapter was approximately modeled after our benchtop system, which uses a full-ring detector geometry [124]. This XFET geometry, shown in Fig. 4.1, positions the x-ray pencil beam perpendicularly to six hexagonally arranged Pb slit apertures sitting in front of the detectors.

All XFET simulations in this study were performed with TOPAS, a Geant4 wrapper Monte Carlo software [163], using a physics package suitable for medical applications, `g4em-standard_opt3`. Phantoms placed at the isocenter were rastered horizontally and vertically through a two-dimensional 120 kVp polychromatic pencil beam with no angular divergence. Each phantom was rastered through the beam at horizontal and vertical increments of choice; this resolution choice varied with computational allowances for each phantom as specified below. To decrease computation time, only the portion of the spectrum above 65.263 keV was simulated. Because only energies above the K-edge of gold will contribute to fluorescence production, using this limited spectrum still scored all relevant photons for image formation, including gold K_{α_1} fluorescent emissions at 68.8 keV as well as scatter in the neighboring energy bins. This reduced the computational burden significantly by simulating only $\sim$15% of the counts that would otherwise be used with the full spectrum model.

Lead apertures were placed at a distance $d_1 = 83$ mm from the isocenter in a hexagonal pattern, as shown in Fig. 4.1. Apertures were 1 mm thick, which allowed for only $\sim$1%

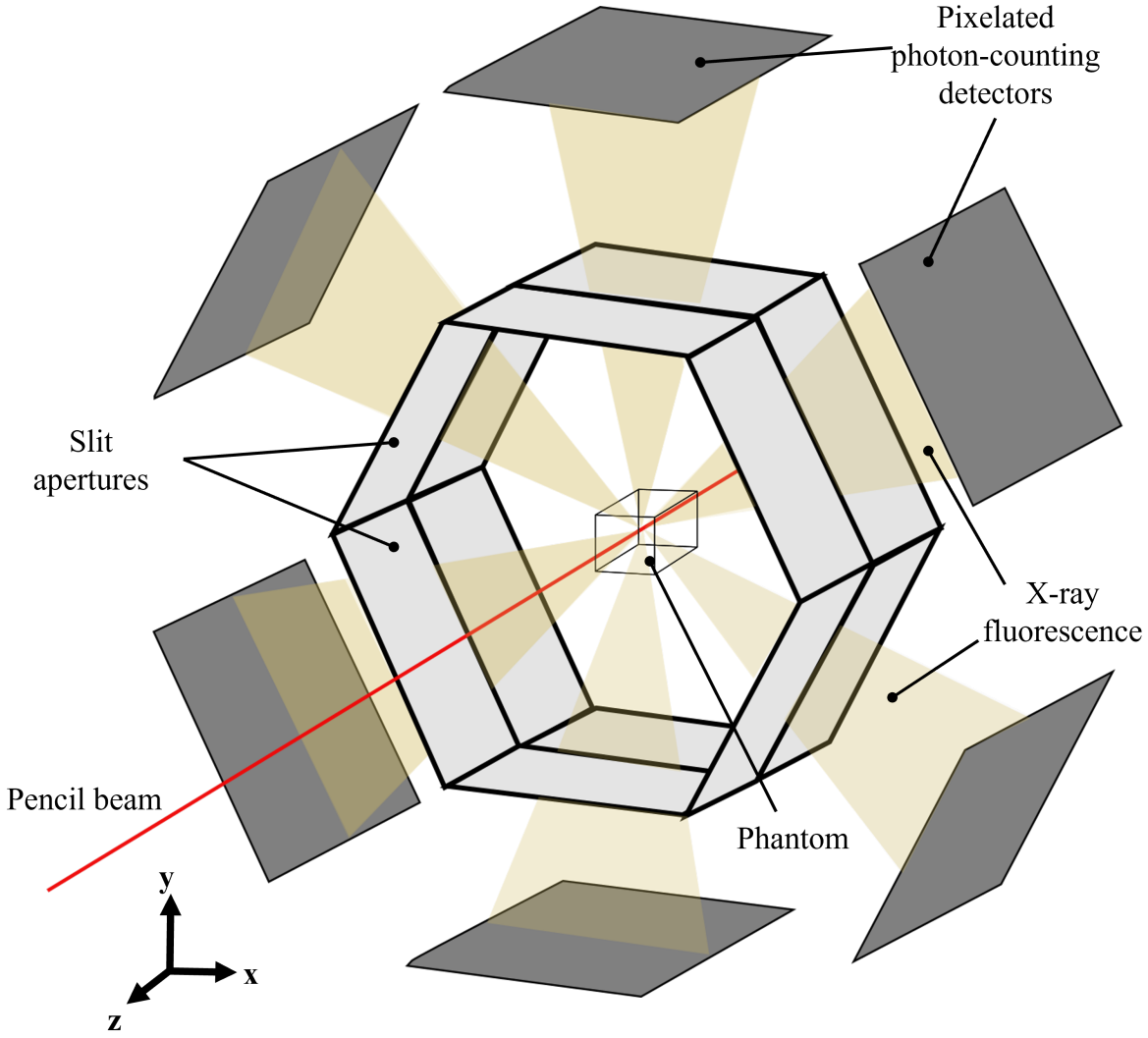

Figure 4.1: Illustration of XFET imaging geometry used in this chapter, with six hexagonal slit-detector combinations (not to scale).

photon penetration at the fluorescent energy of interest and contained slits of width $w = 0.5$ mm positioned at $z = 0$ mm.

Each lead aperture was placed between the isocenter and a detector at a distance $d_1 + d_2 = 166$ mm from the isocenter. There were six detector planes also arranged hexagonally in a full-ring geometry. Each detector plane had dimensions 92 mm $\times$ 120 mm and was divided into 46 $\times$ 120 spatial bins (pixels), such that the width of each detector column was 1 mm and each row was 2 mm. Each aperture plane was equidistant from its corresponding detector and the isocenter ($d_1 = d_2$). This geometry, coupled with the slit width of 0.5 mm, allowed for the 1:1 mapping of detector pixel z-width to the 1 mm axial resolution of the object. The spectral information offered by XFET's detectors allowed for scoring of x-ray fluorescence and scattered photons in 1 keV energy bins. We used 100% counting efficiency in XFET simulations for a standardized comparison to idealized CT, discussed further in Sec. 4.2.2.

Images were formed by summing photon counts in the appropriate energy bin across all detector rows for each object voxel. Because XFET is a direct imaging modality, no image reconstruction was needed nor applied. XFET axial resolution, originally 1 mm, was rebinned to 2 mm for increased contrast with some loss of spatial resolution. The spectral information of the detected counts was used for Compton scatter background subtraction. The energy bin containing gold K_{α_1} fluorescence counts also contains contamination from Compton scatter at the same energy. Therefore, the Compton scatter background was removed by first finding the sum of detected counts in the two adjacent energy bins to the fluorescent energy. These counts were averaged to find the Compton scatter background image, smoothed across the object plane with a Gaussian kernel with $\sigma = 1$ pixel and then subtracted from the image to reveal an image consisting of, in principle, only fluorescence photons.

4.2.2 CT scanner design

Fan-beam CT simulations were completed in Python using Siddon's raytracing algorithm [154], with fan-beam filtered backprojection (FFBP) reconstruction. CT simulations were designed to be approximately dose- and scale-matched to XFET simulations; both modalities are well-suited for imaging mouse-sized objects.

The CT scanner geometry was approximately modeled after previous microCT systems [164, 165, 166, 167, 168]. Geometric parameters included a 100-mm source-to-isocenter distance (SID), 200-mm source-to-detector distance (SDD), 1024 detector channels, and channel detector width (h) equaling the resolution of the discretized phantom. Instead of a flat-panel detector used for some microCT systems, we used a curved detector shown in Fig. 4.2 (not to scale), with a comparable 19.37 degree fan angle (γ_{fan}). We acquired 438 projection views over a 219° rotation (equal to $180^\circ + 2\gamma_{fan}$, the minimum rotation required for complete angular data) [169].

We simulated both EICT and PCCT detector schemes. The EICT simulation used an energy-weighted compound Poisson noise model, and the PCCT simulation used a direct Poisson noise model. Perfect counting efficiency was used to provide a matched comparison to XFET simulations. Similarly, the CT source was the complete 120 kVp x-ray spectra that was effectively used for XFET simulations. The CT simulations were highly idealized in that they did not include scatter contamination or electronic noise.

To form an image, we first simulated fan-beam CT images of multiple sequential slices of each discretized phantom, equivalent to a 2-mm slice. We summed photon counts axially over all detector rows to form an image of the 2-mm slice of the object, resulting in images that matched the XFET axial slice width. FFBP with a general sinc window filter was used to reconstruct images with a desired spatial resolution [169]. A fourth-degree polynomial beam-hardening correction was applied to alleviate cupping artifacts [169].

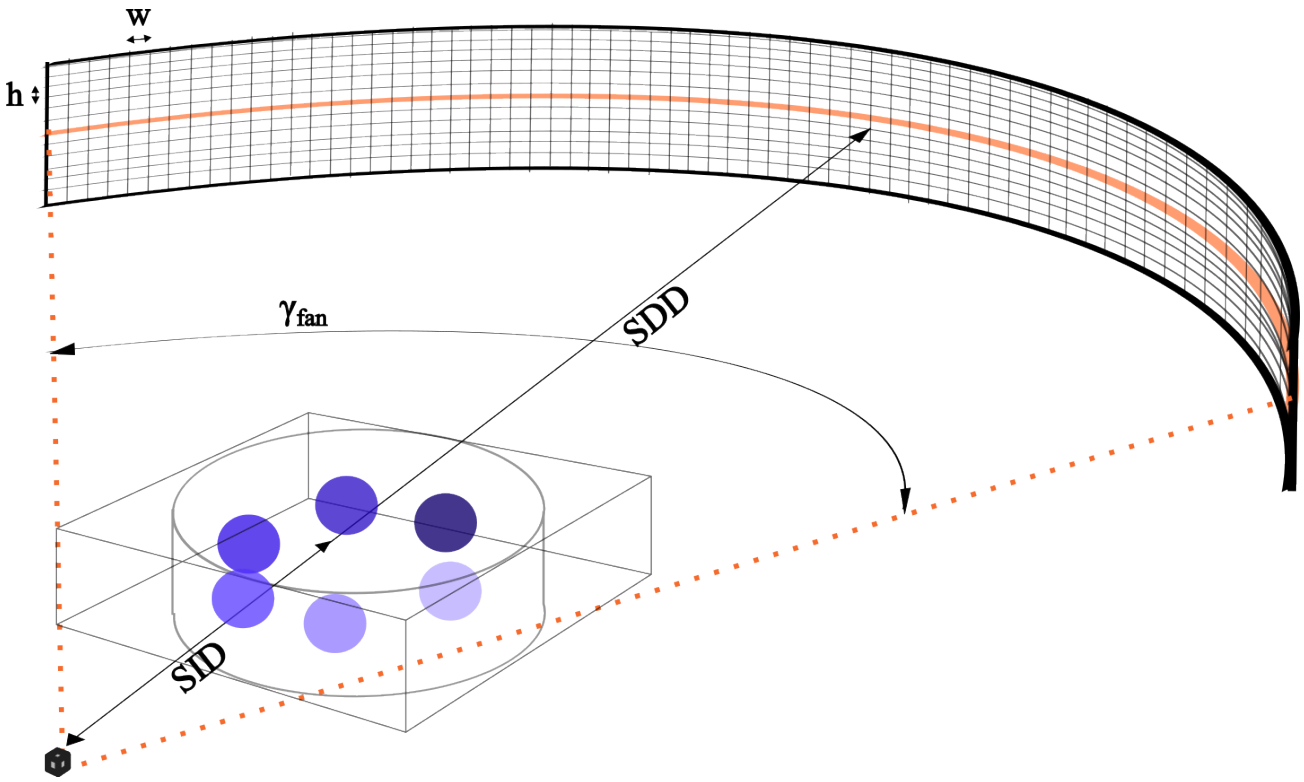

Figure 4.2: CT geometry used in the present work, with one fan-beam detector slice highlighted. Axial, fan-beam CT simulations were completed for multiple slices of numerical phantoms (not to scale).

4.2.3 Phantom simulations

The XFET, PCCT, and EICT simulations were performed for the two phantoms described below to compare CNRs and to quantify the detection limit of gold under varied imaging conditions.

MOBY phantom

The phantom used in this simulation was a discretized numerical mouse phantom, MOBY, displayed in Fig. 4.3 [162]. This phantom consisted of various of ICRP tissues, including soft tissue, cortical bone, skeletal muscle, brain tissue, and adipose tissue. Gold nanoparticles at various concentrations were placed in the phantom: 4% by weight in the kidneys; 0.75% by weight in the spleen, lung, heart, and spherical hind leg tumor; and 0.12% by weight in the liver.

XFET imaging of MOBY was designed to test a realistic object in a preclinical setting. XFET simulations were performed as described in Sec. 4.2.1, with MOBY placed tail-first into the pencil beam. MOBY was rastered in 1-mm horizontal and vertical increments through the beam. An equivalent of 1.25×10^8 histories were used at each pencil beam position. MOBY XFET images, which were the sum of all detector counts as described above, had 1-mm x- and y- resolution and 2-mm axial resolution.

Two 2-mm axial slices of MOBY were scanned with PCCT and EICT: one slice containing the kidneys and another containing the hind-leg tumor. CT images were reconstructed with 1-mm x- and y-resolution to match XFET resolution. The CT simulations were approximately dose matched to XFET, as both simulations delivered effectively 1.25×10^8 histories to a central point with area $(1\text{ mm})^2$.

In both XFET and CT images, square regions of interest (ROI) were placed around the kidneys, hind leg tumor, and background abdominal tissue, as shown in Figure 4.4. We extracted the average signal from the gold-containing ROIs, C_{Au}, as well as from the

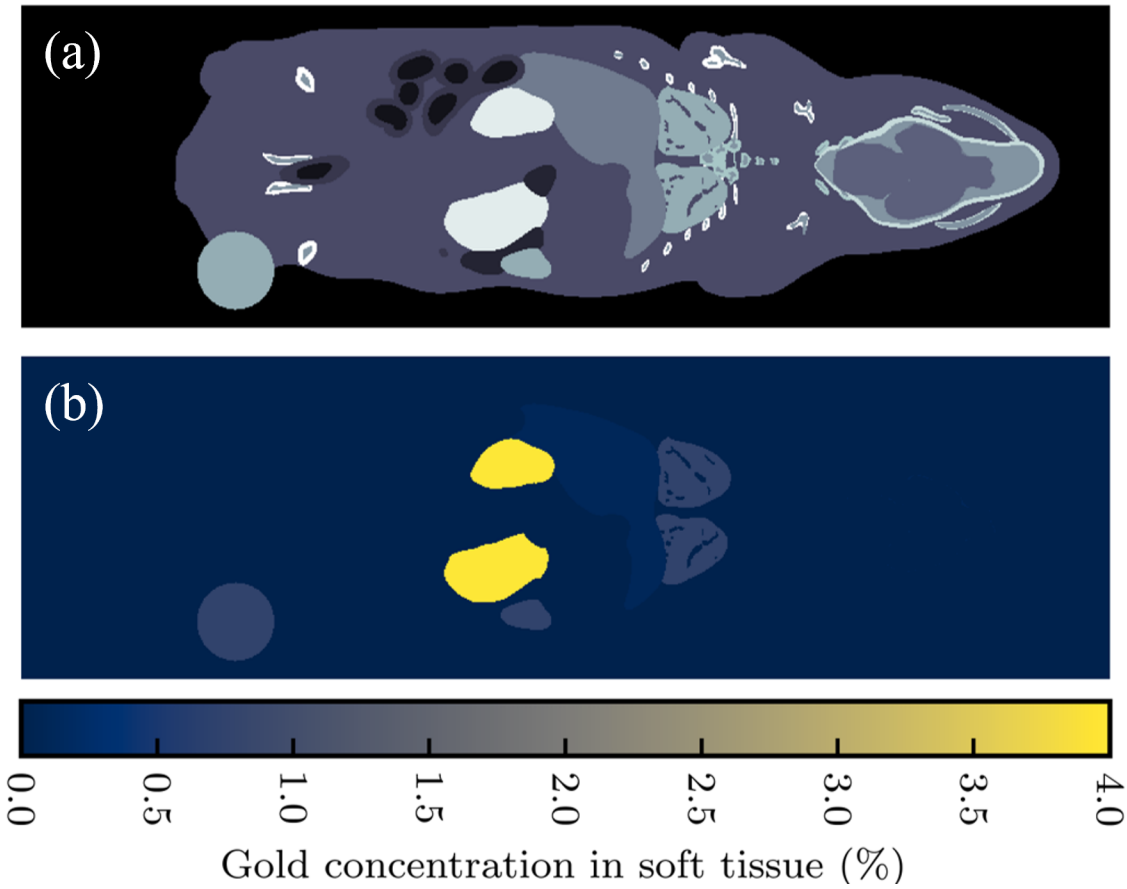

Figure 4.3: Numerical MOBY mouse phantom: (a) anatomical map; (b) map of gold concentrations in specific organs.

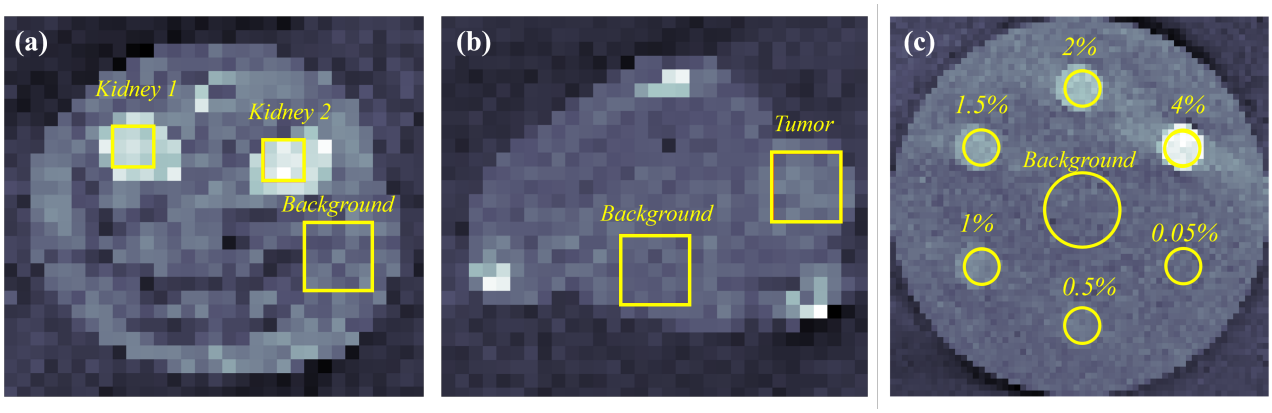

Figure 4.4: CT images demonstrating ROI placement for: (a) the MOBY kidney slice; (b) the MOBY tumor slice; (c) the contrast-depth phantom. Within the MOBY phantom, the square ROIs were placed in background regions, the hind leg tumor, and over each of two kidneys. In the contrast-depth phantom, the circular ROIs were placed over each gold sphere, and in the background region. Displayed ROIs were used for CNR calculations in both XFET and CT images.

background ROIs without gold, C_{bkg}. CNRs were computed for each kidney and the hind leg tumor with

$$CNR = \frac{C_{Au} - C_{bkg}}{\sigma_{bkg}}, \tag{4.1}$$

where σ_{bkg} is the standard deviation of the counts in the background ROI. CNRs were compared between EICT, PCCT, and XFET images. The Rose criterion, which defines CNR = 4 as the lower limit of signal detection [121], was used to qualify detectability of the organs of interest.

Contrast-depth phantom

While MOBY mimicked a realistic preclinical imaging task, a contrast-depth phantom, shown in Figure 4.5, was designed to quantify the conditions under which CT outperforms XFET. Imaging this phantom with both CT and XFET allowed us to study CNR dependence on gold concentration and beam depth.

The cylindrical contrast-depth phantom shown in Figure 4.5 was 3.2 cm in diameter and

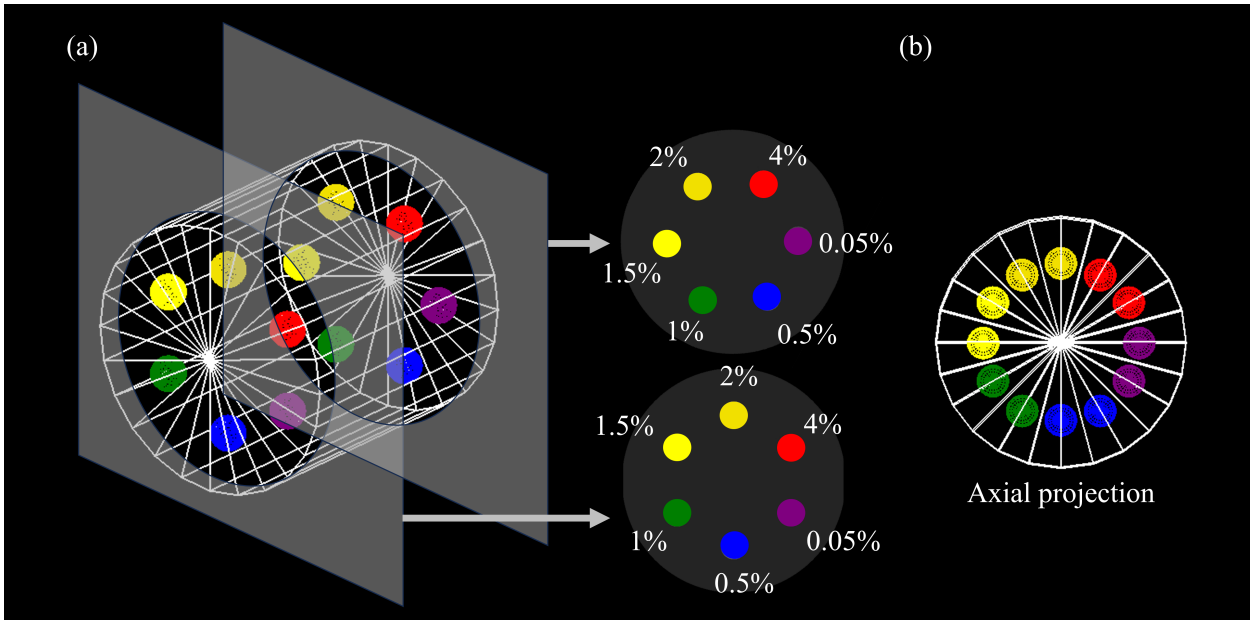

Figure 4.5: (a) Contrast-depth phantom cylindrical phantom, containing various gold concentrations in soft tissue (shown as % by weight). While only two depths are shown here for simplicity, four were simulated. (b) Axial projection view of contrast-depth phantom, demonstrating that the gold spheres do not overlap axially.

composed of ICRP soft tissue. The phantom contained 4-mm diameter spherical inserts of 4.0, 2.0, 1.5, 1.0, 0.5, and 0.05% gold concentration by weight in ICRP soft tissue. The inserts were placed on two planes of different depths relative to the XFET pencil beam, which traveled parallel to the long axis of the cylinder. This feature tested the effect of beam depth and hardening on XFET contrast performance. A total of four beam depths were tested: 3.25 mm, 28.75 mm, 54.25 mm, and 79.75 mm. The spherical inserts did not axially overlap, to ensure the pencil beam was only attenuated by soft tissue before reaching any sphere of interest.

XFET images of the contrast-depth phantom were formed using the geometry and methods described in Sec. 4.2.1, using an equivalent of 1.25×10^8 histories in each pencil beam position, and a 0.5-mm vertical and horizontal resolution. A separate simulation was performed to score total phantom dose using the complete pencil beam spectrum with 1.25×10^8 histories.

The CT simulation was performed with the geometry described in Sec. 4.2.2. In XFET, a pencil beam penetrates along the craniocaudal axis, which reduces the photon flux delivered with increasing distance and results in lower CNR with greater depth. In CT imaging, on the other hand, a fan beam penetrates perpendicular to this axis, so CNR has no axial-depth dependence. For this reason, CT images were simulated for only one sphere-containing plane of the cylindrical phantom.

To image this plane with EICT and PCCT, we considered that each slice of the discretized phantom had a width of 0.0625 mm, and aimed for a total slice width of 2 mm to match the axial resolution of XFET images. We simulated fan-beam CT data acquisitions for 32 adjacent slices of the phantom and summed over the detected photon counts for all slices to obtain our final sinogram. CT images were reconstructed to have matched resolution to XFET: 0.5 mm horizontal and vertical resolution (corresponding to a 64×64 imaging matrix). We also reconstructed higher resolution images—0.125 mm in both dimensions (corresponding to a 256×256 image matrix)—which were comparable to resolutions produced with microCT [170].

Both XFET and CT simulations were approximately dose matched: both used a beam flux intensity of 1.25×10^8 photons to a central point of area $(0.5 \text{ mm})^2$. More detail about dose matching for this phantom and for MOBY can be found in Appendix D.

To compare CNRs produced by each modality, circular ROIs were placed as shown in Figure 4.4. Background ROIs were placed in the center of each image and were larger than the gold ROIs to lower the variance of the measurements taken from these ROIs, including mean and standard deviation of counts.

Five separate images were acquired for XFET, PCCT, and EICT to provide a metric of uncertainty in CNR measurements. This effort included five distinct XFET simulations using different seeds, and five separate noise realizations for CT. The number of repeated simulations was chosen on the basis of computational constraints.

Partial-FOV imaging

Unlike PCCT and EICT, which require a full sinogram to image any ROI, XFET's novel detection scheme can perform partial FOV imaging. We demonstrate this ability here.

After imaging the contrast-depth phantom with the method described in Sec. 4.2.3, we performed an additional, partial-FOV, high-resolution XFET scan. The XFET geometry described in Sec. 4.2.1 remained constant, but this acquisition used an approximate 51-fold increase in local dose (6.41×10^9 histories per beam location) and rastered the pencil beam in 0.25-mm horizontal and vertical increments. The ROI scanned was a $(5.25\text{ mm})^2$ square centered around the spherical insert containing the lowest concentration of gold (0.05%). This concentration was chosen because it is approximately the theoretical detection limit of CT in typical acquisitions [8, 99]. Thus, this acquisition aimed to demonstrate not only partial-FOV capabilities, but also XFET's detection limit improvement with increased dose.

4.3 Results

4.3.1 MOBY phantom

Figure 4.6 shows axial slices of the MOBY phantom imaged with XFET, EICT, and PCCT. The XFET results in greater CNRs for both kidneys and the tumor when compared to either EICT or PCCT. Figure 4.7 displays a summary of kidney and tumor CNRs; XFET resulted in CNRs of 24.5, 21.6, and 3.4 for each kidney and tumor, respectively. Lower CNR values resulted from EICT (CNR = 4.4, 4.6, 1.5) and PCCT (CNR = 6.5, 7.7, 2.0). Every modality could detect both kidneys according to the Rose criterion [121]. The tumor approached this detection limit when imaged by XFET but fell well below this limit when imaged with EICT and PCCT. Across all three organs of interest, XFET provided an average CNR improvement of 315% compared to EICT and 175% compared to PCCT.

Streak artifacts are present in the XFET coronal view (not shown) and, with close in-

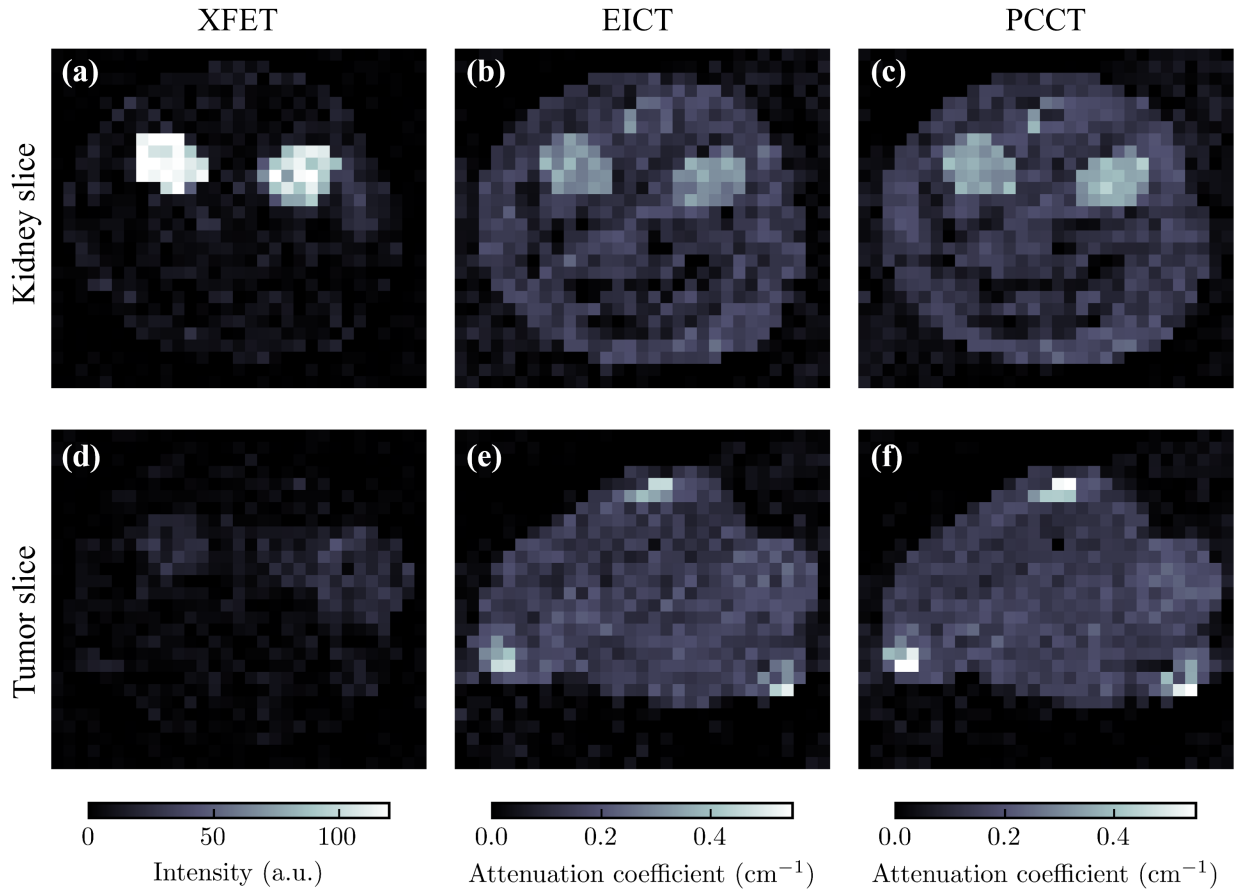

Figure 4.6: Comparison of axial slices of MOBY imaged with three modalities studied here. Kidneys appear with more contrast in the XFET image than in the EICT and PCCT images. The tumor is less visible due to decreased gold concentration. (a) XFET kidney image; (b) EICT kidney image; (c) PCCT kidney image; (d) XFET tumor image; (e) EICT tumor image; (f) PCCT tumor image.

spection, can be seen in the axial XFET slice containing the tumor as bright "shadows" of the kidneys.

4.3.2 Contrast-depth phantom

Figure 4.8 compares the CNRs obtained from the contrast-depth phantom imaged with XFET, PCCT, and EICT. The 0.5-mm- and 0.125-mm-resolution CT images produced similar results.

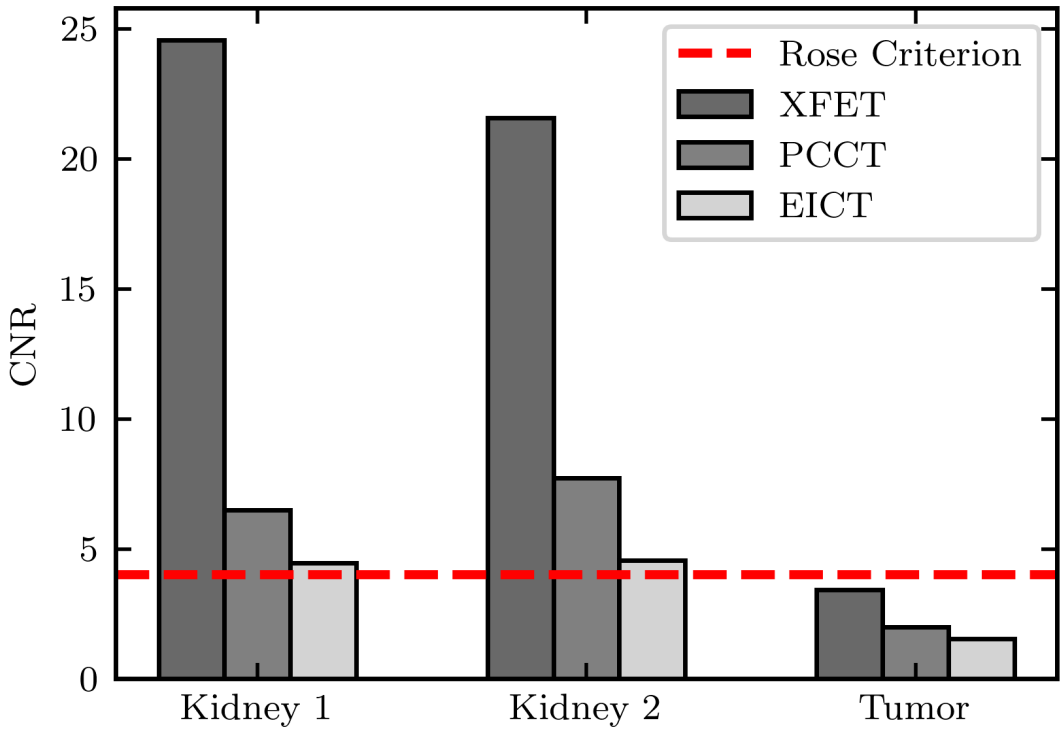

Figure 4.7: Organ CNRs for each modality. The horizontal dashed line represents the Rose criterion. Bars meeting this threshold indicate organs that would be detectable in imaging.

As shown in Fig. 4.8, CNRs are linearly related to known gold concentration in both XFET and CT acquisitions. As expected, CNR increases with increasing gold concentration and decreasing depth of XFET imaging. Superficial XFET (3.25 mm beam depth) produces the greatest CNRs across all gold concentrations. Between the XFET beam depths of 28.75 mm and 54.25 mm, PCCT produces greater CNRs than XFET. EICT produces very similar CNRs to XFET at a 54.25 mm beam depth. Finally, deep XFET (79.75 mm) produced the lowest CNRs across all gold concentrations.

Figure 4.8 also contains a horizontal line representing the threshold for the Rose criterion of detectability [121]. We extracted the intersection between the Rose criterion and XFET's linear relationship of CNR to gold concentration. These intersections, equivalent to the gold concentration detection limits, are plotted as a function of beam depth in Fig. 4.9. An

exponential fit given in Fig. 4.9 was chosen to fit the data because for a given gold concentration, the primary factor impacting CNR in XFET is beam attenuation. Extrapolating to surface imaging (depth = 0 mm), the XFET detection limit for this phantom dose (16 mGy) is 0.44% gold by weight.

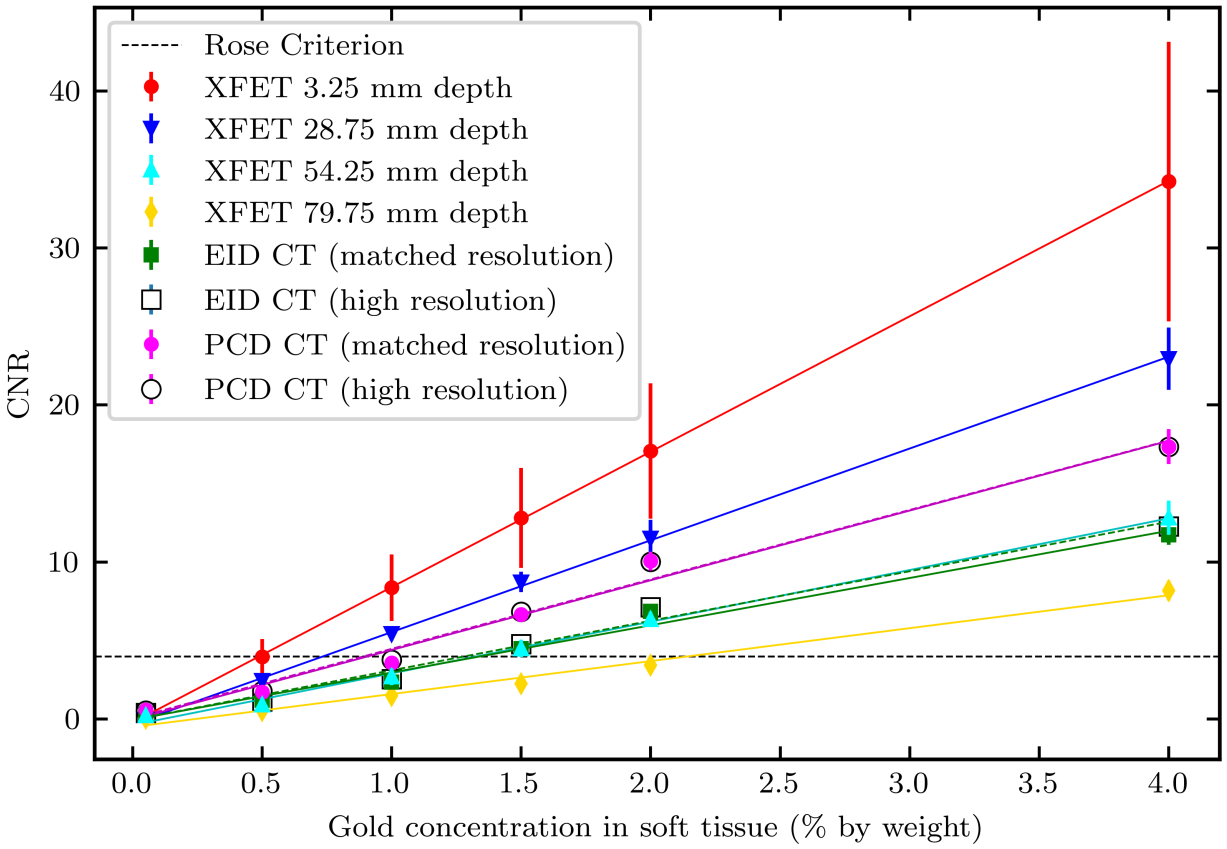

Figure 4.8: Comparison of CNRs as a function of known gold concentration with XFET and CT in the contrast-depth phantom. Note that the CT results are not depth dependent. A beam depth deeper than 28.75 mm, PCCT outperforms XFET. EICT performs similarly to XFET at a beam depth of 54.25 mm. Error bars indicate standard deviation of 5 independent noise realizations.

Figures 4.10 and 4.11 display XFET and CT images, respectively, of the contrast-depth phantom. As XFET imaging depth increases, CNR decreases, and visibility of low concen-

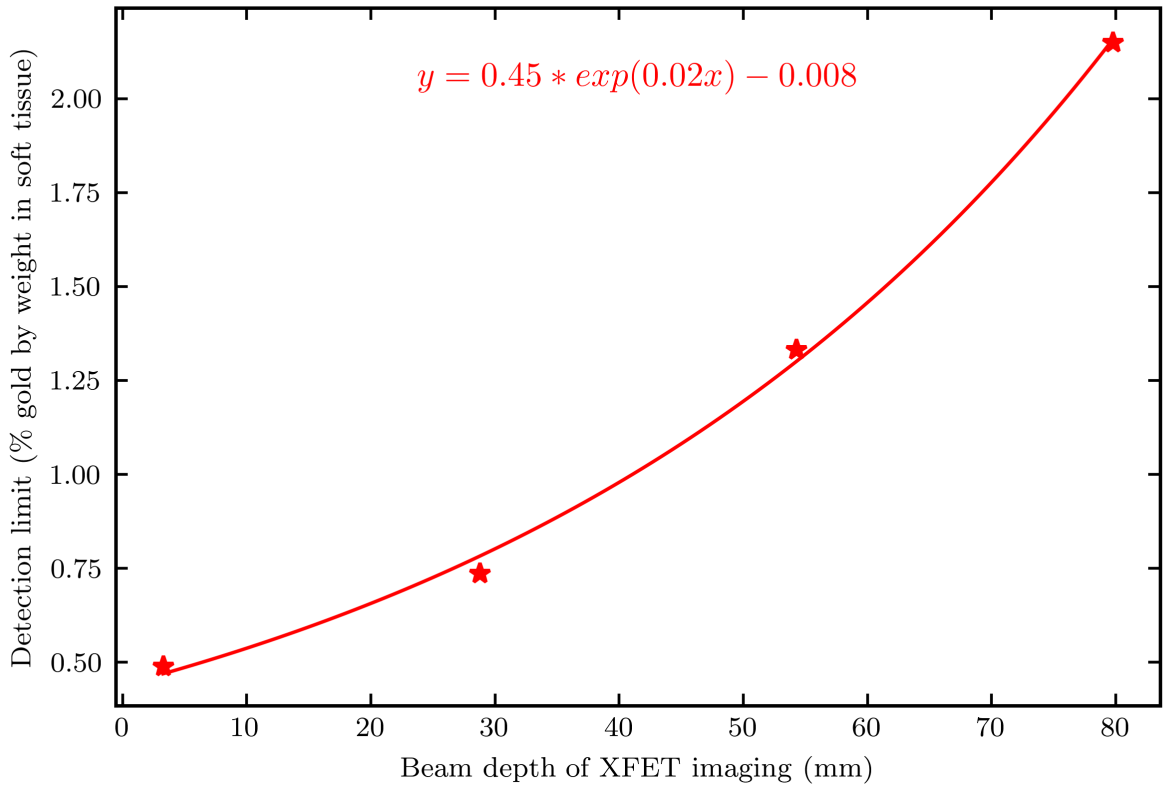

Figure 4.9: XFET detection limit, as function of imaging depth for 125 million histories (approximately 16 mGy).

trations of gold decreases or is lost. CT images, both 0.5-mm- and 0.125-mm-resolution reconstructions, display beam-hardening artifacts, most prominent as streaks between the two highest gold concentrations in each image. CT is able to clearly visualize the background soft tissue cylinder.

4.3.3 Partial-FOV imaging

Figure 4.12 displays the full-FOV contrast-depth phantom image and the partial-FOV image simulated using XFET at a beam depth of 3.25 mm. As demonstrated, the previously undetectable 0.05% gold insert is made visible with a 51-fold increase in imaging dose to this

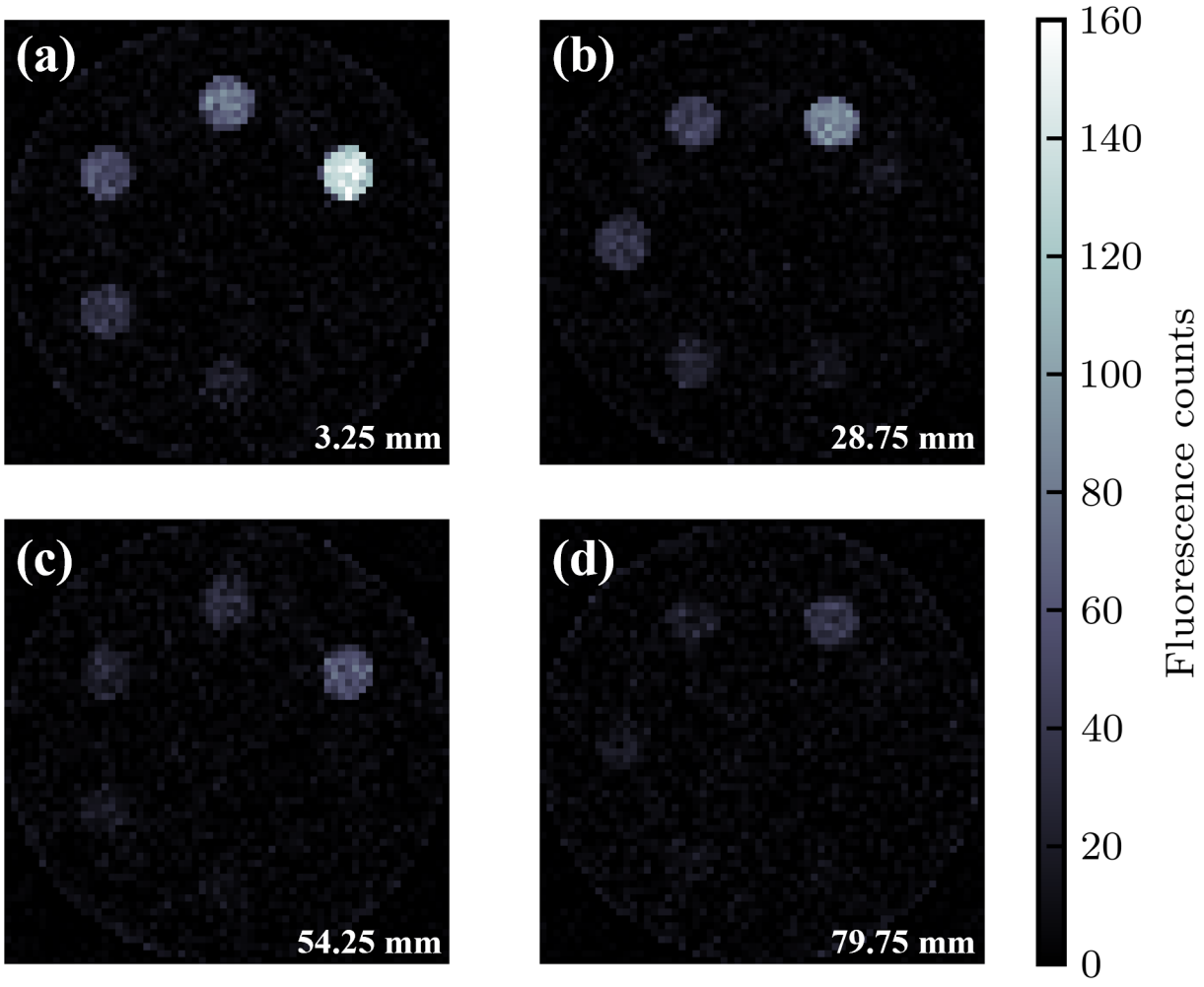

Figure 4.10: Comparison of XFET images of the contrast-depth phantom at varying depths: (a) XFET at 3.25 mm depth; (b) XFET at 28.75 mm depth; (c) XFET at 54.25 mm depth;(d) XFET at 79.75 mm depth.

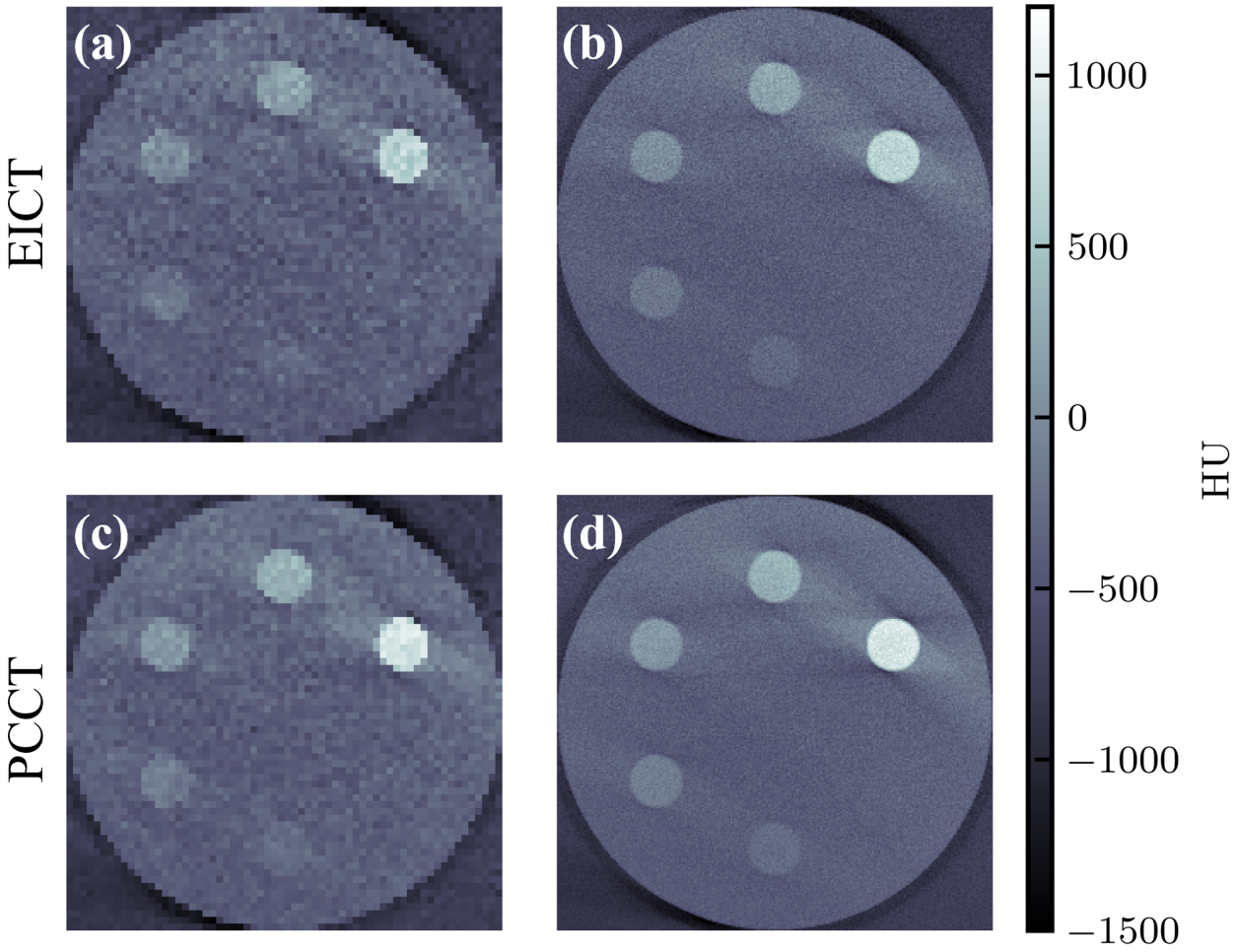

Figure 4.11: Comparison of EICT and PCCT images of the contrast-depth phantom. (a) EICT images with 64 × 64 resolution matching XFET; (b) EICT images with 256 × 256 resolution; (c) PCCT images with 64 × 64 resolution; (d) PCCT images with 256 × 256 resolution.

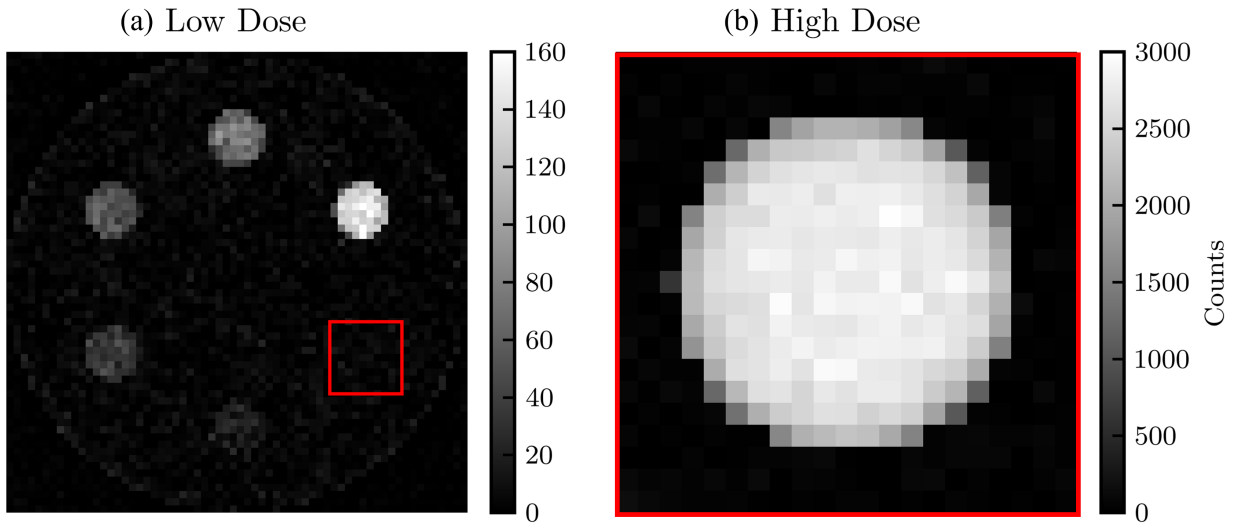

Figure 4.12: (a) Low dose XFET image with a square ROI indicating region probed in partial-FOV imaging. (b) Partial-FOV image of 0.05% gold simulated with high local dose.

ROI.

4.4 Discussion and Conclusions

XFET is characterized by a novel image acquisition scheme that utilizes pixelated, energy-sensitive, photon-counting detectors in combination with slit apertures and a pencil beam through which a phantom is rastered. Because of this geometry, XFET possesses several advantages over other imaging modalities that give it potential to be used for metal mapping in certain preclinical applications. As mentioned in Sec. 4.1, conventional EICT and PCCT that does not utilize spectral information can only distinguish between differences in attenuation. XFET stands apart from these modalities in that it can map many different metals simultaneously by measuring fluorescent energies unique to each metal. Furthermore, XFET is distinct from conventional XFCT in that it is a direct imaging modality that does not measure a sinogram: its mechanism of imaging allows for the possibility of joint estimation and partial FOV imaging. The primary aim of XFET is to provide metal quantification, high sensitivity, and *in vivo* imaging capability for preclinical applications. This chapter

demonstrates XFET's potential for these tasks. However, certain parameters such as depth and metal concentration must be considered before preclinical translation.

The two modalities studied here, XFET and CT, have different implications for image quality that may affect the metal quantification task. For example, Fig. 4.11 shows that both EICT and PCCT can suffer from beam-hardening artifacts even with a water-based correction, particularly when imaging greater metal concentrations. Although more advanced beam-hardening corrections can be applied to alleviate such streaking artifacts, these are often bone-based corrections that can require some degree of hand-tuning [169]. This may have a detrimental effect on metal quantification accuracy. XFET can also suffer from a critical streak artifact due to the combination of x-ray penetration of the lead slit apertures and imperfect background subtraction. This artifact is especially visible for illuminated lines containing high gold concentrations. The artifact only affects the axial direction but can still affect 3-D gold quantification, as seen in XFET's tumor slice in Fig. 4.6 where a bright "shadow" of the MOBY kidneys could be conflated for gold. Fortunately, this artifact will likely be eliminated with thicker lead apertures and slits with an optimized converging shape, which is implemented for benchtop XFET hardware [124].

XFET is also characterized by a resolution-signal tradeoff. In XFET, axial resolution is determined by slit width and z-width of each detector pixel. Thus in this chapter, the original 1-mm axial resolution was resampled to 2 mm and matched to CT axial slice width, which worsened the axial resolution but increased the signal and gold visibility. In benchtop preclinical applications, this tradeoff must be considered, and the imaging parameters can be tailored to meet study requirements. XFET horizontal and vertical resolution, however, are determined by beam spread and rastering. While improving XFET signal through resampling the axial resolution, we maintained a high x- and y-resolution by rastering the phantoms through the beam in small steps, as low as 0.25 mm for the contrast-depth phantom. This characteristic of XFET—the partial independence of axial imaging from horizontal

and vertical imaging—is also what allows for partial FOV imaging and probing small regions of interest.

CNRs obtained with XFET are dependent on both beam depth and metal concentration, whereas those obtained with CT are only dependent on metal concentration. Therefore, there is a threshold imaging depth below which XFET outperforms CT. We found that this depth is between 28.75 mm and 54.25 mm for both PCCT and EICT for the parameters simulated here. Specifically, PCCT outperforms XFET at ∼54.25 mm depth, while EICT provides similar performance to XFET at this depth. At more superficial depths, XFET outperforms both CT detection systems. XFET's advantage holds for preclinical imaging where small animal sizes fall below this depth threshold; thus, XFET provides higher contrast for the MOBY tumor and kidneys, as summarized in Fig. 4.7. For a given superficial depth, it is not surprising that XFET outperforms both EICT and PCCT. Unlike CT, an anatomical imaging modality, XFET is a functional imaging modality: it images metal in regions with a mechanism similar to other emission tomography systems that detect radioactive decay. It is therefore expected that without beam attenuation limiting the initial pencil beam photon flux, XFET can detect low concentrations of metal with very high contrast.

PCCT unsurprisingly outperforms EICT due to the relative upweighting of lower energy x-rays. No electronic noise was simulated here, but in real detection systems, EICT will suffer from electronic noise effects whereas the PCCT detection scheme will not. This difference will increase the disparity of contrast performance between the two systems. Spectral photon-counting CT (SPCCT) utilizes spectral information to perform material differentiation and K-edge imaging [171]. However, SPCCT is usually characterized by a limited number of spectral bins [172] and utilize CdTe or Si detectors with energy resolutions ranging from 3.5 keV to 10 keV [173]. In contrast, the CdTe HEXITEC detectors used in XFET are characterized by a high spectral resolution (1 keV) that is required for fluorescence imaging [157]. This energy resolution, in combination with XFET's direct detection of fluorescence

without image reconstruction, allows for the differentiation between many different metals with no theoretical loss of CNR. XFET is also characterized by a low photon detection rate, which makes XFET imaging slow, but eliminates the detrimental effects of pulse pile up that reduces signal, reduces dose efficiency, and distorts material differentiation in photon-counting CT [173, 174, 175]. The combination of XFET's detectors with its fluorescence rate and novel acquisition scheme enables improved metal imaging relative to PCCT.

For all imaging modalities, the relationships between CNR and gold concentration are linear and do not overlap, indicating that for a fixed depth the order of modality performance was not dependent on gold concentration. This linearity was expected due to the linear relationship between gold concentration and fluorescence emission in XFET and the approximate linear relationship between gold concentration and attenuation coefficient in CT. This linearity also indicates that XFET is capable of quantitative metal imaging even without image reconstruction for simple objects. However, image reconstruction for attenuation correction may prove useful in realistic metal quantification tasks where gold regions are at varying radial depths or the object has spatially varying attenuation. The image reconstruction algorithm that we have previously developed will be implemented in future work to address this need [149]. We expect this image reconstruction to improve XFET's image uniformity and reduce the contrast dependence on depth.

XFET signal is also dose dependent: for a N-factor dose increase, one expects the CNR to increase by a factor of $\sqrt{N}$. For ideal CT systems neglecting pulse pile-up effects, we expect the relationship between ideal CT and XFET CNRs to be preserved with dose because both CNRs would increase by the same factor for both modalities. However pulse pile-up reduces dose efficiency in PCCT and realistic PCCT CNR would increase at a slower rate depending on the count rate capabilities of the detector at high fluence rates [173]. Because XFET is characterized by a low photon detection rate, it does not suffer the effects of pulse pile-up and therefore CNR is expected to increase as expected with dose. This dose dependence is

demonstrated in this work: the 0.05% gold sphere was originally not visible in Fig. 4.10, which used 1.25×10^8 histories but became very visible in the partial-FOV image, Fig. 4.12, which used a 51-fold increase in local dose (16 mGy $\times$ 51 = 81.6 cGy). This demonstration also highlighted a useful function unique to XFET but not CT nor conventional XFCT: XFET allows for whole FOV imaging followed by partial FOV imaging for a ROI, with excess dose only delivered to the ROI. This capability follows from XFET's direct imaging of a non-rotating object without sinogram acquisition. Imaging with a similar sequence would be especially beneficial for examining organs of interest in preclinical imaging. While benchtop XFET may take on the order of an hour to acquire a full image [124], slow imaging times can be improved over conventional XFCT when utilizing this partial-FOV capability.

Aside from the partial-FOV image, most results of this chapter are specific to the relatively low dose used in this study. This total dose to the contrast-depth phantom was scored by TOPAS as approximately 16 mGy and therefore is conducive to *in vivo* imaging. For this dose, the XFET detection limit varies with beam depth according to the exponential equation in Fig. 4.9. For surface imaging (depth = 0 mm), the detection limit would be approximately 0.44% gold by weight. Taking dose into account by finding the dose-detection limit product (7.04 %-mGy), the XFET sensitivity reported here outperforms conventional XFCT according to previous reports [95, 115] and performs similarly to XFCT with optimized backscatter- or full-ring-detector geometry [107, 109]. XFET's detection limit can be further improved by using a filtered or monochromatic beam, optimizing slit hardware, or increasing the dose, especially to small ROIs.

The detection limit and dose reported here are sufficient for some preclinical imaging tasks, such as guiding metal-mediated radiation therapy [17, 30]. Because XFET outperforms CT for superficial imaging, XFET would be preferable for mapping metal nanoparticles used in the treatment of skin disease or superficial tumors [10, 90, 91]. Its partial-FOV imaging capability allows for *in vivo* biodistribution imaging of metal nanoparticles for the

development of metal-based drugs. However, there are some limitations of this chapter that warrant further study before XFET's sensitivity and detection limits are finalized.

One limitation of this study was the use of 100% detector counting efficiency. Perfect photon counting was chosen to obtain a standardized comparison of CT and XFET. Real detectors would likely result in slightly lower CNRs for both modalities. CdTe detectors used in CT imaging may suffer from reduced counting efficiency due to pulse pile-up effects. XFET, on the other hand, is characterized by a low fluorescence detection rate and therefore its detectors would not experience detrimental pulse pile up. Furthermore, the 1-mm thick CdTe HEXITEC detectors are expected to absorb 96% of gold's fluorescence emissions at ∼69 keV: similar to the perfect counting efficiency modeled here. This CNR decrease could be further overcome in XFET with hardware optimization or utilization of higher dose partial-FOV imaging. Second, this study did not incorporate scatter in CT simulations, resulting in highly idealized CT images. Scatter contamination of real data would result in lower CT CNR, so XFET is likely to outperform CT at even greater depths than shown here. Metrics for CNR that incorporate ROI variance may be less favorable to XFET, which may balance XFET's advantage. However the CNR definition used here is a more commonly reported metric in literature and is often used when determining detection limits based on the Rose criterion [107, 124]. We also expect CNR results to depend on insert size, which was not studied here: large inserts could potentially self-attenuate in XFET [107]. The 4-mm diameter gold spherical inserts were chosen to be similar in size to the kidneys and tumor of the MOBY phantom: realistically sized ROIs for preclinical imaging. Finally, we did not use spectral information offered by SPCCT to perform material decomposition in this chapter. Like XFET, SPCCT can distinguish between many different metals but it has been shown that its detection limit for gold does not vary significantly from conventional CT [100]. With the scope of this chapter encompassing detection limits and sensitivity differences between modalities, the use of non-weighted SPCCT may not offer additional relevant information

beyond the PCCT detection system presented here. Regardless, modeling and comparing SPCCT will be performed in future work.

The performance differences between CT and XFET may also depend on source specifications such as energy spectrum, maximum kVp, and filtering. For example, monoenergetic beams above gold's K-edge are much more dose-efficient in XFET imaging because every incident photon has the potential to induce fluorescence emissions. Understanding the effect of source specification on performance differences between the modalities is an area of future investigation.

Before XFET can be translated to preclinical work, the metal of interest must be considered. Different atomic number metals have varying photoelectric cross sections, fluorescent yields, and energy of x-ray fluorescent emissions that may impact the contrast seen in XFET as well as CT, which will produce varying results. For example, iodine is sometimes difficult to detect with spectral PCCT due to low numbers of photons around its K-edge energy (33.2 keV) [100, 171, 176], while fluorescent photons around this energy are easily induced and measured with XFET [124]. Although gold was used here due to its significance in novel therapies, our group has also shown that XFET using a multi-pinhole aperture and HEXITEC detectors has resulted in significantly improved detection limits for Gd (0.01%) compared to studies that utilize a similar dose ($\sim$3.26 Gy) [124]. Exploring other metals is another area of future direction and a critical investigation before preclinical translation.

This chapter provides the first comparison of XFET and CT for detecting low concentrations of gold in soft tissue and characterizes the conditions under which XFET outperforms EICT and PCCT. Using both Monte Carlo XFET and analytical fan-beam CT simulations to image a realistic whole-body mouse phantom, we show that XFET provides greater CNRs than CT for 4% Au in the kidneys and 0.75% Au in a hind leg tumor. Performing these simulations with a contrast-depth phantom, we show that XFET outperforms CT for superficial imaging depths (< 28.75 mm) for gold concentrations above 0.5%. XFET's surface detection

limit was quantified as 0.44% for an average phantom dose of 16 mGy compatible with *in vivo* imaging. Finally, XFET's ability to image partial FOVs is demonstrated and the 0.05% Au is easily detected with an estimated dose of approximately 81.6 cGy to the small ROI. Thus, this chapter demonstrates a proof of XFET's benefit for imaging low concentrations of gold at superficial depths in preclinical imaging tasks.

CHAPTER 5

CONCLUSIONS AND FUTURE DIRECTIONS

5.1 Summary of presented work

In this work, we have seen that XFET offers a promising tool for imaging low concentrations of metal in small objects, and possesses advantages over other, more conventional metal-mapping modalities such as XFCT. XFET is a direct imaging modality, in that it induces and directly detects x-ray fluorescence emissions from metals without need for noise-amplifying image reconstruction. With this characteristic comes the ability to image small regions of interest without the full sinogram that fundamentally limits the depth of imaging in XFCT. These characteristics, combined with state-of-the-art hardware, give XFET the sensitivity and imaging depth improvements necessary to map metals *in vivo* for emerging cancer therapies and preclinical drug biodistribution studies. Herein, we have improved upon XFET's ability for trace metal mapping, explored its limitations, and demonstrated its capabilities against other metal-mapping modalities.

In Chapter 2, we developed and demonstrated an XFET image reconstruction algorithm that uses emission data alone to jointly estimate the metal map and attenuation map needed for correction. This novel algorithm alternates between updating the attenuation map with a separable paraboloidal surrogates algorithm, and updating the metal density map with a closed-form solution. We performed joint image reconstruction using simulated XFET data of small objects containing low concentrations of gold and iron. Our method not only led to promisingly accurate metal and attenuation maps, but also outperformed a more conventional approach that used a conjugate gradient method based on a linearized forward model. We successfully extended our image reconstruction technique to the case of an unknown beam attenuation map, demonstrating an accurate joint estimation from emission data alone without any prior attenuation knowledge. Thus, this chapter added to XFET's

advantages: in simultaneously estimating the attenuation map, one avoids the need for an additional, radiation-dose-delivering transmission scan that would otherwise be needed for attenuation correction.

In Chapter 3, we explored the implications on image quality associated with detector placement in XFET. To investigate the effect of detector placement on joint estimation, we used two main mathematical tools: eigendecomposition of the Fisher information matrix and singular value decomposition of the linearized imaging model. We reported eigenvectors and singular vectors, along with their associated eigen- and singular values to better understand which vectors have high information content and are preserved in imaging. We combine this mathematical investigation with image reconstructions of metal and attenuation maps using the algorithm developed in Chapter 2. We found that aside from an optimal full-ring geometry, two parallel detectors provided the greatest metal and attenuation map accuracy but at the cost of reduced isotropic spatial resolution in the attenuation map. This chapter informed about implications of detector placement for imaging tasks where flexibility in this placement is required, or for tasks where a full-ring geometry is not feasible.

Finally, in Chapter 4, we demonstrated XFET's capabilities compared to CT for certain imaging applications. We compared Monte Carlo XFET simulations to highly idealized, fan-beam CT simulations. These data were collected for two phantoms: the first was a numerical whole-body mouse phantom, containing organ gold nanoparticle concentrations that realistically mimicked a preclinical scenario, and the second was a cylindrical soft tissue phantom containing a range of gold concentrations (0.05% to 4% by weight) at varying depths. By imaging these phantoms with dose-matched XFET and CT simulations, we showed that for superficial depths (< 3 cm), XFET outperforms CT in imaging gold concentrations down to 0.5%. For the dose used in this chapter, which is conducive to preclinical studies, we found that XFET's detection limit was 0.44% for superficial imaging, but also acknowledge that XFET can be further optimized to lower that limit. We also demonstrated XFET's

unique ability to image partial fields, and with additional probing and dose, detected 0.05% gold. This chapter quantified XFET's detection limit for *in vivo* dose levels, demonstrated XFET's partial field imaging capabilities, and showed that it outperforms CT for superficial imaging. Thus, this chapter demonstrated XFET's promise for preclinical metal mapping, and contained discussion around the advantages and limitations of XFET for more informed translation into preclinical use.

In Chapter 1, we have summarized some previous XFCT studies with regards to their detection limits, imaging doses, and preclinical applicability. We propose that the results of this dissertation serve as a reference to XFET's capabilities in these areas. However, the results of this dissertation have primarily improved XFET's current capabilities and demonstrated its potential for *in vivo* preclinical imaging. This dissertation also provides the information necessary to predict XFET's ability to map therapeutic metal particles for informed development, safer treatment, and fewer side effects of clinical cancer therapies.

5.2 Proposed future directions

Prior to translation to preclinical or clinical use, there are several areas that require further investigation. Completion of these investigations will offer additional understanding of XFET's potential for metal mapping in clinical scenarios, and potentially offer novel image reconstruction methods for related emission tomography systems.

5.2.1 Slit aperture angular optimization

As seen in Table 1.1, many groups have found that positioning detectors in backscatter geometries aids in reducing Compton scatter contamination of the signal, and therefore increasing sensitivity. It remains to be seen if a backscatter geometry—specifically, positioning the slit at a backscatter angle—would benefit XFET, or if the resulting geometric efficiency reduction would outweigh the potential sensitivity improvements. There could exist an an-

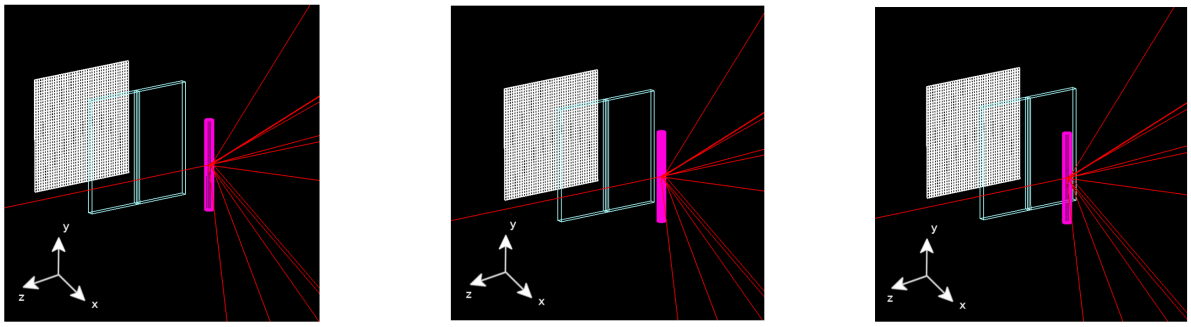

Figure 5.1: Summary of preliminary study optimizing angular slit position. The slit was positioned in a backscatter (left), central (center), or forward scatter (right) position. Figure: Tabitha Welch.

gle at which there is an optimal ratio of geometric efficiency to scatter contamination. Our group's preliminary investigation into this matter used TOPAS Monte Carlo software to measure XFET data from a rod consisting of 0.5% Au in soft tissue. This rod was positioned at three axial locations relative to the slit, as shown in Fig. 5.1. These positions were equivalent to three distinct slit positions: forward scatter, backscatter, and a central position. This preliminary study revealed that the central position had the greatest ratio of geometric efficiency to Compton scatter contamination: the central position offered the greatest sensitivity.

Because only two off-center rod positions were measured, a natural extension of this optimization study would involve continuously moving the rod along the axial (z) direction, measuring counts at many slit angles, and utilizing Geant4's ability to track counts from certain processes to discern between measured Compton and fluorescence photons. We suggest that a plausible result to this study would be that a slight backscatter slit angle—one not as extreme as used preliminarily—might offer greater sensitivity over the central position. This optimization could offer even greater sensitivity advantages to XFET.

5.2.2 Implementing joint image reconstruction for data acquired with a polychromatic beam

The work presented in Chapter 2 assumed a monochromatic beam that efficiently generated fluorescence emissions from gold and iron atoms. However, most benchtop XFET and XFCT systems will utilize a polychromatic x-ray beam as the incident source. Thus, it is critical to extend forward and inverse models to the polychromatic case. In this subsection, we provide the polychromatic forward and inverse models, but propose that implementing this image reconstruction method for the Monte Carlo dataset be an area of future work. Previously, we have used a discrete forward model,

$$p_{ij} = \frac{(d_1 + d_2)}{R_{ij}^3} I_0 A_0 D_0 d_0 s t f_i \exp\Big(- \sum_k L_{ijk} \mu_k^{(E_F)} \Big) \exp\Big(- \sum_k L'_{ik} \mu_k^{(E_B)} \Big), \tag{5.1}$$

which was for a monochromatic pencil beam of energy E_B. We will now consider the case of a polychromatic beam. We will first work out the case of known attenuation maps at the beam energies, and discuss how we will correct for this attenuation. We will then consider the case of unknown attenuation at the beam energies.

Consider a polychromatic pencil beam incident on a metal-containing object. This pencil beam will have initial beam flux as a function of energy, $I_0(E)$ ($\mathrm{cm}^{-2}\mathrm{s}^{-1}\mathrm{keV}^{-1}$). This beam will contain many energies; intensities of each will be attenuated by an unknown attenuation map of the object at that energy, $\mu(E)$.

We can write the photon intensity at a point in the object, I_1, as a function of energy,

$$I_1(E) = I_0(E) \exp\Big(- \sum_k L'_k \mu_k(E) \Big), \tag{5.2}$$

where k indexes the attenuation map, and L' represents pathlengths through object voxels. At this point, we have not considered fluorescence attenuation, only beam attenuation.

Now, one can represent the number of K-fluorescent photons created at this point (I_2) as the sum of the beam photons (I_1) above the K-edge of the metal at that point, multiplied with various physical factors including metal density f at that point, beam lag time t, probability that photons of a given energy will interact with the K-shell, and fluorescence yield (all contained in term $s(E)$, which depends on photon energy). Note that all fluorescent photons are monoenergetic:

$$\begin{aligned} I_2 &= \int_{E=E_{K_{edge}}}^{E_{max}} \frac{d_1+d_2}{R^3} A_0 D_0 d_0 t f s(E) I_1(E) dE \\ &= \frac{d_1+d_2}{R^3} A_0 D_0 d_0 t f \int_{E=E_{K_{edge}}}^{E_{max}} s(E) I_0(E) \exp\Big(-\sum_k L'_k \mu_k(E) \Big) dE. \end{aligned} \tag{5.3}$$

Alternatively, I_2 can be discretely modeled as

$$I_2 = \frac{d_1+d_2}{R^3} A_0 D_0 d_0 t f \sum_{E=E_{K_{edge}}}^{E_{max}} s_E I_{0E} \exp\Big(-\sum_k L'_k \mu_k^{(E)} \Big) \Delta E, \tag{5.4}$$

where E is indexing energy. All other terms in (5.4) are explained in previous chapters. The sum occurs over bounds from the K-edge of the metal producing fluorescence to the maximum energy of the beam, since only those photons that are above the K-edge of the metal will contribute to the production of fluorescent photons.

Finally, the number of fluorescent photons measured at the detector point (p) is I_2 multiplied by the attenuation factor at the energy E_F of the fluorescent photons,

$$p_{ij} = \frac{d_1+d_2}{R_{ij}^3} A_0 D_0 d_0 t f_i \exp\Big(-\sum_k L_{ijk} \mu_k^{(E_F)} \Big) \sum_{E=E_{K_{edge}}}^{E_{max}} s_E I_{0E} \exp\Big(-\sum_k L'_{ik} \mu_k^{(E)} \Big) \Delta E. \tag{5.5}$$

Here, we add an index for object voxel (i) and detector pixel (j) as we have done previously.

With knowledge of priors (s_E and μ_E) and the beam spectrum (I_{0E}), one can define a known term,

$$q''' = \frac{d_1 + d_2}{R_{ij}^3} A_0 D_0 d_0 t \sum_{E=E_{K_{edge}}}^{E_{max}} s_E I_{0E} \exp\Big(- \sum_k L'_{ik} \mu_k^{(E)} \Big) \Delta E. \tag{5.6}$$

Then, (5.5) becomes

$$p_{ij} = q''' f_i \exp\Big(- \sum_k L_{ijk} \mu_k^{(E_F)} \Big), \tag{5.7}$$

and our alternating algorithm developed in Chapter 2 can be easily applied.

The problem becomes more complex without prior knowledge of μ_E. In this case, it appears that there are many unknowns. Fortunately however, there exists an approximate linear relationships between the attenuation maps at every beam energy and the attenuation map at the fluorescent energy, for various concentrations of a single metal in a background material. This effectively expresses many unknowns as one unknown. The linear relationships are shown in Fig. 5.2. The coefficients of these linear fits (slopes and y-intercepts, or b_E and a_E respectively) are known priors, obtained from NIST datasets.

For a given beam energy E, the attenuation map at E can be expressed as

$$\mu_k^{(E)} \approx b_E \mu_k^{(E_F)} + a_E. \tag{5.8}$$

Therefore, (5.6) becomes

$$q''' = \frac{d_1 + d_2}{R_{ij}^3} A_0 D_0 d_0 t \sum_{E=E_{K_{edge}}}^{E_{max}} s_E I_{0E} \exp\Big(- \sum_k L'_{ik} \big(b_E \mu_k^{(E_F)} + a_E \big) \Big) \Delta E \tag{5.9}$$

for unknown beam attenuation maps. Equation 5.9 contains only one unknown, $\mu_k^{(E_F)}$.

To perform image reconstruction, one can apply our previous alternating algorithm to (5.7), using (5.9) everywhere that q''' appears.

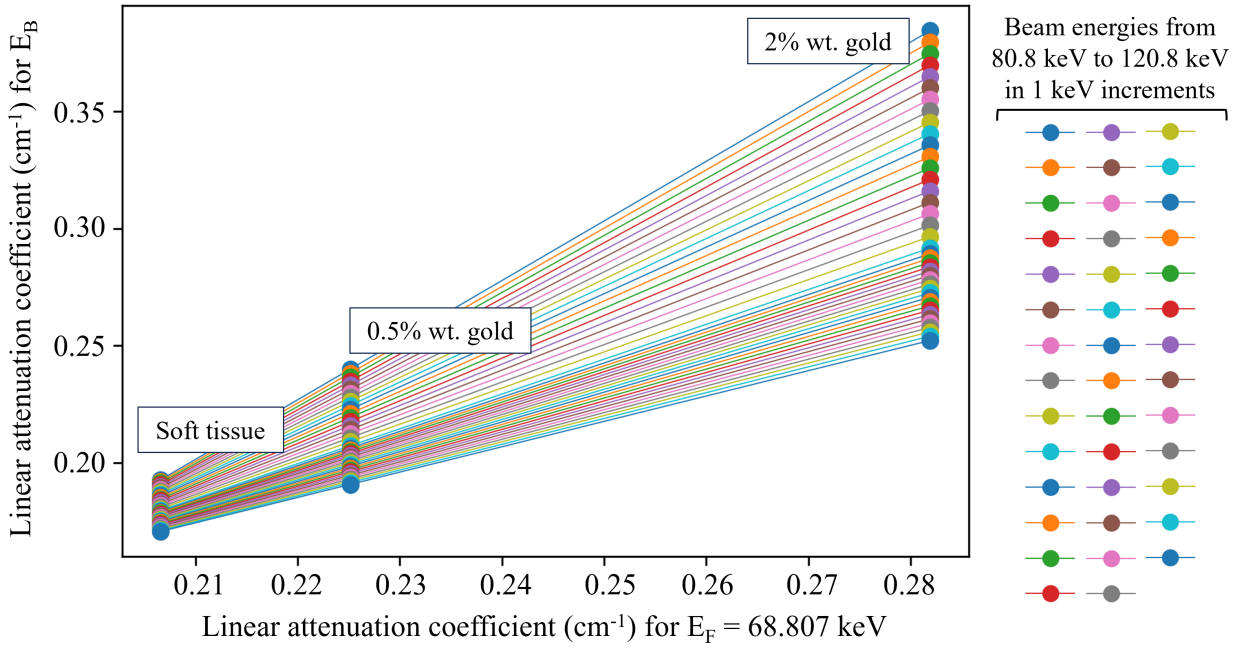

Figure 5.2: Relationship between linear attenuation coefficients at fluorescent energy and beam energies for concentrations of gold in soft tissue.

5.2.3 Extension to benchtop XFET data

A natural progression of the work proposed in Chapter 4 would be the repetition of that study with data acquired with benchtop XFET and small animal CT systems. Although the Monte Carlo XFET simulations in Chapter 4 were as realistic as possible, the CT simulations were highly idealized and did not incorporate scatter. Collecting real data would offer an even more realistic comparison between the two modalities, and the measurement of CT scatter would likely result in XFET's outperformance at even greater depths than those resulting from Chapter 4. For an optimized benchtop XFET acquisition, we suggest implementing the polychromatic inverse algorithm proposed in Section 5.2.2.

5.2.4 Time-of-flight PET joint image reconstruction

Since the development of time-of flight (TOF) PET and especially in the last few years, there has been significant effort put into achieving the "10-ps frontier" in temporal resolution [177], with some skeptics [178]. In 2021, there was one demonstration of TOF PET detectors with 32 picosecond temporal resolution, corresponding to a spatial precision of 4.8 mm [179]. This technique was based on detecting prompt Cerenkov photons combined with a convolutional neural network. This apparent breakthrough, which allows for the direct detection of tracer with 5 mm precision without image reconstruction, allows for improvements in joint activity/attenuation estimation. With this novel development, there is now opportunity to improve joint activity/attenuation estimation for this "reconstruction-free" TOF PET.

There is significant overlap between the direct imaging of reconstruction-free TOF PET and XFET. Both detect monochromatic emissions: 511 keV γ photons in the case of PET annihilation events, and x-ray fluorescence emissions in XFET. Both are direct imaging modalities, or can be construed as such. Direct imaging is critical: because individual emission locations are known, emissions themselves can be used to estimate the attenuation map that photons pass through. Therefore, it is straightforward to apply our joint XFET image reconstruction algorithm developed in Chapter 2 to this high-temporal-resolution TOF PET system.

A TOF PET dataset can be organized in a "list" format, where for each coincidence detection event, there is associated information about the spatial coordinates of the two involved detectors and the timing difference between the detection events at those detectors. For a given coincidence event, with ultra-fast temporal resolution, this allows for the calculation of emission location, within some uncertainty determined by the timing resolution of the detectors. After energy filtering the data for non-annihilation events, these data can be restructured into a matrix of detected gamma photons, lexicographically indexed by emission location and spatial detector bin. A given element of this array (p_{ij}) will be a sum of

all detected photon counts by detector crystal j that originated from object pixel i. Each measurement is given discretely by

$$p_{ij} = c_{ij} a_i \exp\big(-\sum_k L_{ijk}\mu_k\big), \tag{5.10}$$

where c_{ij} is the sensitivity of the detector at j for activity in pixel i in the absence of attenuation, a_i is activity of pixel i (in counts/second), L_{ijk} is the pathlength through object pixels for emission point i, detector j, and attenuation pixel k, and μ_k is the attenuation in pixel k. Note that the above equation gives expected values for Poisson random variables. Equation 5.10 assumes that additive terms like randoms and scatter are negligible or not considered, due to an extremely tight coincidence window and energy discrimination, respectively.

Note that with this forward model, conventional full line integrals are not considered. Alternatively, we split the line integral into its two parts: one measured by each detector. Before this split, known emission locations must be found using coincidence information.

Equation 5.10 is analogous to (2.14): the effort to jointly estimate metal density and attenuation in XFET is analogous to jointly estimating activity and attenuation in TOF PET. Expressing the forward model in (5.10) allows for the direct translation of our developed image reconstruction method to this application.

To implement joint image reconstruction, one will first perform a normalization scan and acquire the number of counts expected without attenuation,

$$n_{ij} = c_{ij} a_i. \tag{5.11}$$

Measuring n_{ij} for a known activity a_i will allow for the calculation of the sensitivity matrix, c_{ij}, which must be known *a priori*. This normalization scan can be performed for one emission location by measuring an off-centered point source with no significant attenuation (in air). The resulting data can be spatially restructured to find the expected sensitivity for

all detector pixels for each emission location i.

Our alternating algorithm can then be implemented rather directly. Both the attenuation and activity update can be directly applied. Because these data are best modeled as Poisson random variables, the assumptions of the closed-form solution derivation in Appendix A still hold.

Although this inverse problem is likely ill-conditioned just as was XFET's, the accurate results of Chapter 2 give promise for this joint reconstruction method for TOF PET. Upon successful implementation of this joint reconstruction will come a novel method for obtaining the attenuation map needed for quantitative PET imaging without an additional dose-delivering CT scan.

APPENDIX A

DERIVATION OF CLOSED-FORM METAL MAP SOLUTION

For the non-linearized imaging model, the log-likelihood function is the Poisson log-likelihood associated with transmission tomography [3],

$$\mathcal{L}(\mathbf{p}\,;\,\mathbf{f},\boldsymbol{\mu}) = \sum_{i',j}\Big\{\, p_{i'j}\ln\Big[q''_{i'j}f_{i'}\exp\Big(-\sum_k L_{i'jk}\mu_k\Big)\Big] - q''_{i'j}f_{i'}\exp\Big(-\sum_k L_{i'jk}\mu_k\Big)\Big\}, \tag{A.1}$$

where i' indexes object voxels, j indexes detector pixels, $q''_{i'j}$ are elements of the vector $\boldsymbol{q''}$, which is given by (2.13), and the remaining variables in (A.1) are defined in the List of Mathematical Symbols. Taking the derivative of $\mathcal{L}$ with respect to the density map entries yields

$$\frac{\partial\mathcal{L}}{\partial f_i} = \sum_{i',j}\left[\frac{p_{i'j}}{f_{i'}} - q''_{i'j}\exp\Big(-\sum_k L_{i'jk}\mu_k\Big)\right]\frac{\partial f_{i'}}{\partial f_i}. \tag{A.2}$$

It is apparent that $\frac{\partial f_{i'}}{\partial f_i} = \delta_{i'i}$, so (A.2) becomes

$$\frac{\partial\mathcal{L}}{\partial f_i} = \sum_{j}\left[\frac{p_{ij}}{f_i} - q''_{ij}\exp\Big(-\sum_k L_{ijk}\mu_k\Big)\right]. \tag{A.3}$$

Setting (A.3) equal to zero, a closed-form solution for the density map is revealed, assuming the attenuation map is known:

$$\hat{f}_i = \frac{\sum_j p_{ij}}{\sum_j q''_{ij}\exp(-\sum_k L_{ijk}\mu_k)}. \tag{A.4}$$

(A.4) is the same as (2.16) and (2.20), which are used in the alternating approach to update the metal density map given a current guess of the attenuation map. Alternately, to

maximize the Poisson likelihood in (A.1) for a fixed density map, the SPS algorithm can be used, which is described and derived in [3] and Appendix B.

APPENDIX B

DERIVATION OF SPS ALGORITHM FOR ATTENUATION UPDATE

The derivation of the SPS algorithm follows the approach taken by Fessler [3], where it is introduced as a reconstruction algorithm for an attenuation map, μ. The derivation is based on the optimization transfer principle, which instead of directly maximizing the objective function Φ, utilizes a surrogate function ϕ for each iteration that is easier to maximize. This surrogate satisfies conditions given by Fessler [3].

Note that one uses a penalty function, R, to improve the conditioning of the noisy problem. The objective function to be maximized is therefore the *penalized-likelihood* objective function:

$$\Phi(\mu) \equiv \mathcal{L}(\mu) - \beta R(\mu). \tag{B.1}$$

This incorporation of R into Φ is known as regularization, and is weighed by a scalar roughness parameter β. For the following derivations, note that the indices are not necessarily the same as those used in Chapter 2, and are reconciled at the end of this appendix.

B.1 Forming the separable quadratic surrogate function

To form ϕ, let us first assume known measurements, $\boldsymbol{p}$, and a known metal map $\boldsymbol{f}$, which can be incorporated with other known terms, $\boldsymbol{q''}$, into $\boldsymbol{b} = \boldsymbol{q''}\boldsymbol{f}$. Note in the context of our alternating algorithm, the metal map is fixed (or "known") when updating the attenuation map with SPS.

When working with a log-likelihood function of the form $\sum_i h_i(l_i)$ with elements

$$h_i(l) = p_i \ln(b_i e^{-l_i} + r_i) - (b_i e^{-l_i} + r_i), \tag{B.2}$$

a useful surrogate function is a parabola surrogate:

$$q_i(l|l_i^{(n)}) \equiv h_i(l_i^{(n)}) + \dot{h}_i(l_i^{(n)})(l - l_i^{(n)}) - \frac{c_i^{(n)}}{2}(l - l_i^{(n)})^2, \tag{B.3}$$

where $l_i^{(n)} = [L\boldsymbol{\mu}^{(n)}]_i$, and $\dot{h}$ indicates the derivative of the log likelihood function, h. For the inverse problem presented in this chapter, the system matrix L is a matrix of elements L_{ij}, which are pathlengths through voxels (in the present case, L_{ij} is equivalent to L_{mk} that is discussed in the List of Mathematical Symbols and used in Chapter 2). Note that we assume no random counts: $\boldsymbol{r} = \mathbf{0}$. Finally, the $c_i^{(n)}$are equivalent to the terms $c_m^{(n)}$ which is defined in the List of Mathematical Symbols.

Summing over the 1-D surrogate functions in (B.3) indexed by i gives a surrogate function, Q_1 for the log likelihood function:

$$Q_1(\boldsymbol{\mu}|\boldsymbol{\mu}^{(\boldsymbol{n})}) \equiv \sum_{i=1}^{N_Y} q_i([L\boldsymbol{\mu}]_i|[L\boldsymbol{\mu}^{(n)}]_i). \tag{B.4}$$

However, to then address the difficulty in maximizing Q_1, Fessler applies a convexity trick first applied by De Pierro [180], which first expresses the following matrix-vector multiplication as

$$[L\boldsymbol{\mu}]_i = \sum_j^{N_p} \alpha_{ij}\Big[\frac{L_{ij}}{\alpha_{ij}}\big(\mu_j - \mu_j^{(n)}\big) + l_i^{(n)}\Big], \tag{B.5}$$

Where α_{ij} is chosen to be equal to $\frac{L_{ij}}{L_i}$, and $L_i = \sum_j L_{ij}$. This re-expression is incorporated into a second surrogate function, Q_2, for the previous function Q_1. This new surrogate is a separable function, where the elements are given by:

$$Q_{2,j}(\mu_j|\boldsymbol{\mu}^{(n)}) \equiv \sum_{i=1}^{N_Y} \alpha_{ij} q_i\Big(\frac{L_{ij}}{\alpha_{ij}}\big(\mu_j - \mu_j^{(n)}\big) + l_i^{(n)}|l_i^{(n)}\Big). \tag{B.6}$$

This is a natural separable surrogate function for the log likelihood function,

$$L(\boldsymbol{\mu}) \geq \sum_{j=1}^{N_p} Q_{2,j}(\mu_j|\boldsymbol{\mu}^{(n)}), \tag{B.7}$$

and is easily maximized.

The same process is repeated for the penalty function, R. The cost matrix C with elements c_{kj} can be expressed as:

$$[C\boldsymbol{\mu}]_k = \sum_{j}^{N_p} \gamma_{kj} \Big[\frac{c_{kj}}{\gamma_{kj}} \big(\mu_j - \mu_j^{(n)}\big) + [C\boldsymbol{\mu}^{(n)}]_k \Big], \tag{B.8}$$

where $\gamma_{kj} \geq 0$ and $\sum_j^{N_p} \gamma_{kj} = 1$. With the penalty function expressed as

$$R(\mu) = \sum_{k=1}^{K} w_k \frac{1}{2} \big([C\boldsymbol{\mu}]_k\big)^2, \tag{B.9}$$

and applying the same convexity trick as used before, the natural separable surrogate for R is formed with elements given as:

$$R_j(\mu_j|\boldsymbol{\mu}^{(n)}) = \sum_{k=1}^{K} \gamma_{kj} w_k \frac{1}{2} \Big(\frac{c_{kj}}{\gamma_{kj}} \big(\mu_j - \mu_j^{(n)}\big) + [C\boldsymbol{\mu}^{(n)}]_k \Big] \Big)^2. \tag{B.10}$$

The final separable quadratic surrogate function, ϕ , is formed by combining Q_2 and R as in (B.1):

$$\phi_{2,j}(\mu_j|\boldsymbol{\mu}^{(n)}) \equiv Q_{2,j}(\mu_j|\boldsymbol{\mu}^{(n)}) - \beta R_j(\mu_j|\boldsymbol{\mu}^{(n)}). \tag{B.11}$$

More detail about these surrogate derivations and convexity tricks can be found in [3] and [180].

B.2 Forming the separable paraboloidal surrogates algorithm

The optimization algorithm for μ_j simply maximizes ϕ for every j. Because ϕ is quadratic, this is performed by zeroing its derivative, which is completed below.

First, expressing (B.6) in its entirety by utilizing (B.3) and (B.5):

$$\begin{aligned} Q_{2,j}(\mu_j|\boldsymbol{\mu}^{(n)}) &= \sum_{i=1}^{N_Y} \frac{L_{ij}}{L_i}\Big(h_i(l_i^{(n)}) + \dot{h}_i(l_i^{(n)})\Big(L_i\big(\mu_j - \mu_j^{(n)}\big) + l_i^{(n)} - l_i^{(n)}\Big) \\ &\quad - \frac{c_i^{(n)}}{2}\Big(L_i\big(\mu_j - \mu_j^{(n)}\big) + l_i^{(n)} - l_i^{(n)}\Big)\Big) \\ &= \sum_{i=1}^{N_Y} \frac{L_{ij}}{L_i}\Big(h_i(l_i^{(n)}) + \dot{h}_i(l_i^{(n)})\Big(L_i\big(\mu_j - \mu_j^{(n)}\big)\Big) - \frac{c_i^{(n)}}{2}\Big(L_i\big(\mu_j - \mu_j^{(n)}\big)\Big)\Big). \end{aligned} \tag{B.12}$$

Then, the derivative of $Q_{2,j}$ is:

$$\begin{aligned} \frac{\partial}{\partial \mu_j} Q_{2,j}(\mu_j|\boldsymbol{\mu}^{(n)}) &= \sum_{i=1}^{N_Y} \frac{L_{ij}}{L_i}\Big(L_i \dot{h}_i(l_i^{(n)}) - c_i^{(n)} L_i^2\big(\mu_j - \mu_j^{(n)}\big)\Big) \\ &= \sum_{i=1}^{N_Y} \Big(L_{ij}\dot{h}_i(l_i^{(n)}) - L_{ij}L_i c_i^{(n)}\big(\mu_j - \mu_j^{(n)}\big)\Big). \end{aligned} \tag{B.13}$$

Similarly, the derivative of R_j is:

$$\frac{\partial}{\partial \mu_j} R_j(\mu_j|\boldsymbol{\mu}^{(n)}) = \sum_{k=1}^{K} c_{kj} w_k \Big(\frac{c_{kj}}{\gamma_{kj}}\big(\mu_j - \mu_j^{(n)}\big) + [C\boldsymbol{\mu}^{(n)}]_k\Big]\Big). \tag{B.14}$$

Then, zeroing the derivative with

$$\frac{\partial Q_{2,j}}{\partial \mu_j} - \beta \frac{\partial R_j}{\partial \mu_j} = 0, \tag{B.15}$$

we obtain

$$\sum_{i=1}^{N_Y}\Big(L_{ij}\dot{h}_i(l_i^{(n)}) - L_{ij}L_i c_i^{(n)}\big(\mu_j - \mu_j^{(n)}\big)\Big) - \beta\sum_{k=1}^{K} c_{kj}w_k\Big(\frac{c_{kj}}{\gamma_{kj}}\big(\mu_j - \mu_j^{(n)}\big) + [C\boldsymbol{\mu}^{(n)}]_k\Big]\Big) = 0. \tag{B.16}$$

Equation (B.16) can be reorganized as follows:

$$\begin{aligned}
\sum_{i=1}^{N_Y}\Big(L_{ij}\dot{h}_i(l_i^{(n)}) - L_{ij}L_i c_i^{(n)}\big(\mu_j - \mu_j^{(n)}\big)\Big) &= \beta\sum_{k=1}^{K} c_{kj}w_k\Big(\frac{c_{kj}}{\gamma_{kj}}\big(\mu_j - \mu_j^{(n)}\big) + [C\boldsymbol{\mu}^{(n)}]_k\Big]\Big) \\
\Big(\sum_{i=1}^{N_Y} L_{ij}L_i c_i^{(n)} + \beta\sum_{k=1}^{K} c_{kj}w_k\frac{c_{kj}}{\gamma_{kj}}\Big)\big(\mu_j - \mu_j^{(n)}\big) &= \sum_{i=1}^{N_Y} L_{ij}\dot{h}_i(l_i^{(n)}) - \beta\sum_{k=1}^{K} c_{kj}w_k[C\boldsymbol{\mu}^{(n)}]_k\Big] \\
\big(\mu_j - \mu_j^{(n)}\big) &= \frac{\sum_{i=1}^{N_Y} L_{ij}\dot{h}_i(l_i^{(n)}) - \beta\sum_{k=1}^{K} c_{kj}w_k[C\boldsymbol{\mu}^{(n)}]_k\Big]}{\Big(\sum_{i=1}^{N_Y} L_{ij}L_i c_i^{(n)} + \beta\sum_{k=1}^{K} c_{kj}w_k\frac{c_{kj}}{\gamma_{kj}}\Big)}.
\end{aligned} \tag{B.17}$$

Finally, solving for the attenuation map, μ_j, (which yields the attenuation map at the latest $(n+1)^{th}$ iteration, $\mu_j^{(n+1)}$), one obtains the separable paraboloidal surrogates algorithm update,

$$\mu_j^{(n+1)} = \mu_j^{(n)} + \frac{\sum_{i=1}^{N_Y} L_{ij}\dot{h}_i(l_i^{(n)}) - \beta\sum_{k=1}^{K} c_{kj}w_k[C\boldsymbol{\mu}^{(n)}]_k}{\sum_{i=1}^{N_Y} L_{ij}L_i c_i^{(n)} + \beta\sum_{k=1}^{K} c_{kj}w_k\frac{c_{kj}}{\gamma_{kj}}}. \tag{B.18}$$

There are a few notation changes applied to (B.18) to obtain (2.19). First, the indices in (B.18) are interchanged to form (2.19): in Chapter 2, we use m for i, k for j, and r for k. Second, the derivative of the likelihood function, $\dot{h}_i$, in our case is given by $\dot{h}_m = q''_m f_m e^{-l_m^{(n)}} - p_m$, which is responsible for the expansion of the numerator in (2.19). Non-negativity is applied as a physical constraint. Last, the second term on the denominator of (B.18) can be re-written as follows with Fessler's choice of $\gamma_{kj} = |c_{kj}|/c_k$:

$$\sum_{k=1}^{K} c_{kj}w_k\frac{c_{kj}}{\gamma_{kj}} = \sum_{k=1}^{K}\frac{c_{kj}^2 w_k}{\gamma_{kj}} = \sum_{k=1}^{K}|c_{kj}|c_k w_k. \tag{B.19}$$

Thus, with these changes, (B.18) becomes (2.19).

APPENDIX C

FORMATION OF THE FISHER INFORMATION MATRIX

To form the FIM used in Chapter 3, we assume that the photon counts measured with XFET, p_{ij}, are Poisson random variables, and that the forward model follows a Poisson log likelihood function,

$$\mathcal{L}(\boldsymbol{p};\boldsymbol{f},\boldsymbol{\mu}) = \sum_{i,j}\Big\{ p_{ij}\ \ln\Big[q''_{ij}f_i\ \exp\Big(-\sum_k L_{ijk}\mu_k\Big)\Big] - q''_{ij}f_i\ \exp\Big(-\sum_k L_{ijk}\mu_k\Big)\Big\}. \quad \text{(C.1)}$$

We can begin to take gradients of this likelihood function with respect to the density map and attenuation map to construct the FIM. The gradient with respect to the density map, f_m, is

$$\begin{aligned}\frac{\partial\mathcal{L}}{\partial f_m} &= \sum_i\sum_j\left[\frac{p_{ij}\,q''_{ij}\ \exp\Big(-\sum_k L_{ijk}\mu_k\Big)\frac{\partial f_i}{\partial f_m}}{q''_{ij}f_i\ \exp\Big(-\sum_k L_{ijk}\mu_k\Big)} - q''_{ij}\exp\Big(-\sum_k L_{ijk}\mu_k\Big)\frac{\partial f_i}{\partial f_m}\right]\\ &= \sum_j\left[\frac{p_{mj}}{f_m} - q''_{mj}\exp\Big(-\sum_k L_{mjk}\mu_k\Big)\right]. \end{aligned} \quad \text{(C.2)}$$

Similarly, the gradient of $\mathcal{L}$ with respect to the attenuation map is

$$\begin{aligned}\frac{\partial\mathcal{L}}{\partial\mu_m} &= \sum_i\sum_j\frac{\partial}{\partial\mu_m}\left(\ p_{ij}\ \ln\Big[q''_{ij}f_i\ \exp\Big(-\sum_k L_{ijk}\mu_k\Big)\Big] -\ q''_{ij}f_i\ \exp\Big(-\sum_k L_{ijk}\mu_k\Big)\right)\\ &= \sum_i\sum_j\left(p_{ij}\frac{q''_{ij}f_i\ \exp\Big(-\sum_k L_{ijk}\mu_k\Big)\frac{\partial}{\partial\mu_m}\Big(-\sum_k L_{ijk}\mu_k\Big)}{q''_{ij}f_i\ \exp\Big(-\sum_k L_{ijk}\mu_k\Big)}\right.\\ &\qquad\left. -\ q''_{ij}f_i\exp\Big(-\sum_k L_{ijk}\mu_k\Big)\frac{\partial}{\partial\mu_m}\Big(-\sum_k L_{ijk}\mu_k\Big)\right)\\ &= \sum_i\sum_j\left(-p_{ij}L_{ijm} + q''_{ij}f_i\exp\Big(-\sum_k L_{ijk}\mu_k\Big)L_{ijm}\right). \end{aligned} \quad \text{(C.3)}$$

The Hessian is a block matrix,

$$H = \begin{pmatrix} H_{ff} & H_{f\mu} \\ H_{f\mu}^T & H_{\mu\mu} \end{pmatrix}, \tag{C.4}$$

where the blocks are second-derivative matrices with elements given by

$$[H_{ff}]_{nm} = \frac{\partial^2 \mathcal{L}}{\partial f_n \partial f_m}, \tag{C.5}$$

$$[H_{\mu\mu}]_{nm} = \frac{\partial^2 \mathcal{L}}{\partial \mu_n \partial \mu_m}, \tag{C.6}$$

and

$$[H_{f\mu}]_{nm} = \frac{\partial^2 \mathcal{L}}{\partial f_n \partial \mu_m}. \tag{C.7}$$

The second derivative of the likelihood function with respect to the density map is

$$\begin{aligned} \frac{\partial^2 \mathcal{L}}{\partial f_n \partial f_m} &= \sum_j \left[-\frac{p_{mj}}{f_m^2} \frac{\partial f_m}{\partial f_n} \right] \\ &= \sum_j \left[-\frac{p_{mj}}{f_m^2} \delta_{mn} \right], \end{aligned} \tag{C.8}$$

where the δ_{mn} indicates that this block of the Hessian is a diagonal matrix. The cross derivative is

$$\begin{aligned} \frac{\partial^2 \mathcal{L}}{\partial f_n \partial \mu_m} &= \sum_i \sum_j \left[\delta_{in}\, q''_{ij} \exp\Big(-\sum_k L_{ijk}\mu_k \Big) L_{ijm} \right] \\ &= \sum_j \left(q''_{nj}\, \exp\Big(-\sum_k L_{njk}\mu_k \Big) L_{njm} \right). \end{aligned} \tag{C.9}$$

Setting the mean photon measurements $\bar{p}_{ij} = q''_{ij} f_i \exp(-\sum_k L_{ijk}\mu_k)$, we can rewrite (C.9) as

$$\frac{\partial^2 \mathcal{L}}{\partial f_n \partial \mu_m} = \sum_j \frac{\bar{p}_{nj}}{f_n} L_{njm}. \tag{C.10}$$

Finally, the second derivative of the likelihood function with respect to attenuation map is

$$\begin{aligned}\frac{\partial^2 \mathcal{L}}{\partial \mu_n \partial \mu_m} &= \sum_i \sum_j \left(- q''_{ij} f_i \exp\Big(- \sum_k L_{ijk}\mu_k \Big) L_{ijn} L_{ijm} \right) \\ &= \sum_i \sum_j -\bar{p}_{ij} L_{ijn} L_{ijm}. \end{aligned} \tag{C.11}$$

The Fisher information matrix, F, is given by the expectation of the negative Hessian matrix, which is a block matrix for joint problems similar to this one [137]:

$$F = E\{-H\} = \begin{pmatrix} E\{-H_{ff}\} & E\{-H_{f\mu}\} \\ E\{-H_{f\mu}^T\} & E\{-H_{\mu\mu}\} \end{pmatrix}, \tag{C.12}$$

which gives

$$F = \begin{pmatrix} \sum_j \frac{\bar{p}_{mj}}{f_m^2} \delta_{mn} & -\sum_j \frac{\bar{p}_{nj}}{f_n} L_{njm} \\ -\sum_j \frac{\bar{p}_{mj}}{f_m} L_{mjn} & \sum_i \sum_j \bar{p}_{ij} L_{ijn} L_{ijm} \end{pmatrix}. \tag{C.13}$$

APPENDIX D

XFET AND CT DOSE MATCHING

In the XFET simulations of Chapter 4, a fixed number of photons, I_b, was delivered in each beam location. The cross-sectional area of each beam location, A_0, was determined by the horizontal and vertical resolution targets, with A_0 equal to $(0.5 \text{ mm})^2$ for the contrast-depth phantom and $(1 \text{ mm})^2$ for MOBY. The larger area for MOBY was chosen due to computational constraints of voxelized phantoms. To approximately dose-match the CT simulations, we aimed to deliver I_b photons to an area A_0 of the object at the SID over the course of CT imaging. Some terms below can be seen in Fig. 4.2, which displays a schematic of CT imaging.

Let us use N for the target total counts per area A_0 over all CT projection angles,

$$N = \frac{I_b}{A_0}. \tag{D.1}$$

In our fan-beam CT simulations, the height of a detector element, h, was set equal to the width of one z-slice of the phantom. The width of one detector element, w, can be projected onto the isocenter, where it will have width w_{iso}.

The arc length of the complete fan beam at the SDD, w_{fan}, is given by

$$w_{fan} = \gamma_{fan} SDD, \tag{D.2}$$

where γ_{fan} is the fan angle. The width of one detector element is w_{fan} divided by the number of detector channels, $N_{channels}$:

$$w = \frac{w_{fan}}{N_{channels}} = \frac{\gamma_{fan} SDD}{N_{channels}}. \tag{D.3}$$

Now, we can find the value of w_{iso} given (D.3) and rules of similar triangles:

$$\begin{aligned} w_{iso} &= w\frac{SID}{SDD} \\ &= \frac{\gamma_{fan} SDD}{N_{channels}} \frac{SID}{SDD} \\ &= \frac{\gamma_{fan} SID}{N_{channels}}. \end{aligned} \tag{D.4}$$

Finally, we can calculate how many photons need to be delivered to one detector channel for one projection angle: I_{proj}. This is the target counts per area (N), multiplied by the area of one detector element projected onto the isocenter ($h \times w_{iso}$) and divided by the number of projection angles N_{proj}:

$$I_{proj} = \frac{N}{N_{proj}}(h \times w_{iso}). \tag{D.5}$$

Thus, to approximately dose match our CT simulations to XFET in Chapter 4, we used I_{proj} number photons delivered to each detector channel for each projection angle. XFET simulations used an effective $I_b = 1.25 \times 10^8$; therefore, CT simulations used $I_{proj} = 2356$ for the contrast-depth phantom and $I_{proj} = 1177$ for the MOBY phantom (the difference results from the differences in phantom resolution and target XFET resolution).

REFERENCES

[1] J. H. Hubbell and S. M. Seltzer, "Tables of x-ray mass attenuation coefficients and mass energy-absorption coefficients (version 1.4)," [Online] Available: http://physics.nist.gov/xaamdi, 2004, National Institute of Standards and Technology, Gaithersburg, MD.

[2] F. H. Attix, *Introduction to radiological physics and radiation dosimetry.* John Wiley & Sons, Inc., 1986.

[3] J. A. Fessler, "Statistical image reconstruction methods for transmission tomography," in *Handbook of Medical Imaging, Volume 2*, M. Sonka and J. M. Fitzpatrick, Eds. Washington, USA: SPIE Press, 2000, ch. 1, pp. 1–70.

[4] X. Duan, C. He, S. J. Kron, and W. Lin, "Nanoparticle formulations of cisplatin for cancer therapy," *Wiley Interdiscip Rev Nanomed Nanobiotechnol*, vol. 8, no. 5, pp. 776–791, 2016.

[5] S. A. Gulec, G. Mesoloras, W. A. Dezarn, P. McNeillie, and A. S. Kennedy, "Safety and efficacy of Y-90 microsphere treatment in patients with primary and metastatic liver cancer: The tumor selectivity of the treatment as a function of tumor to liver flow ratio," *J Transl Med*, vol. 5, no. 15, 2007.

[6] L. Faggioni and M. Gabelloni, "Iodine concentration and optimization in computed tomography angiography: Current issues," *Invest Radiol*, vol. 51, no. 12, pp. 816–822, 2016.

[7] M. R. K. Ali, Y. Wu, and M. A. El-Sayed, "Gold-nanoparticle-assisted plasmonic photothermal therapy advances toward clinical application," *J Phys Chem C*, vol. 123, no. 25, pp. 15 375–15 393, 2019.

[8] J. F. Dorsey, L. Sun, D. Y. Joh, A. Witztum, A. A. Zaki, G. D. Kao, M. Alonso-Basanta, S. Avery, A. Tsourkas, and S. M. Hahn, "Gold nanoparticles in radiation research: potential applications for imaging and radiosensitization," *Transl Cancer Res*, vol. 2, no. 4, pp. 280–291, 2013.

[9] S. Her, D. A. Jaffray, and C. Allen, "Gold nanoparticles for applications in cancer radiotherapy: Mechanisms and recent advancements," *Adv Drug Deliv Rev*, vol. 109, pp. 84–101, 2017.

[10] M. Yamada, M. Foote, and T. W. Prow, "Therapeutic gold, silver, and platinum nanoparticles," *Wiley Interdiscip Rev Nanomed Nanobiotechnol*, vol. 7, no. 3, pp. 428–445, 2015.

[11] W. N. Rahman, N. Bishara, T. Ackerly, C. F. He, P. Jackson, C. Wong, R. Davidson, and M. Geso, "Enhancement of radiation effects by gold nanoparticles for superficial radiation therapy," *Nanomed*, vol. 5, no. 2, pp. 136–142, 2009.

[12] A. A. Borran, A. Aghanejad, A. Farajollahi, J. Barar, and Y. Omidi, "Gold nanoparticles for radiosensitizing and imaging of cancer cells," *Radiat Phys Chem*, vol. 152, pp. 137–144, 2018.

[13] C. He and J. C. L. Chow, "Gold nanoparticle DNA damage in radiotherapy: A monte carlo study," *AIMS Bioeng*, vol. 3, no. 3, pp. 352–361, 2016.

[14] T. Kong, J. Zeng, X. Wang, X. Yang, J. Yang, S. McQuarrie, A. McEwan, W. Roa, J. Chen, and J. Z. Xing, "Enhancement of radiation cytotoxicity in breast-cancer cells by localized attachment of gold nanoparticles," *Small*, vol. 4, no. 9, pp. 1537–1543, 2008.

[15] D. M. Herold, I. J. Das, C. C. Stobbe, R. V. Iyer, and J. D. Chapman, "Gold microspheres: a selective technique for producing biologically effective dose enhancement," *Int J Radiat Biol*, vol. 76, no. 10, pp. 1357–1364, 2000.

[16] J. F. Hainfeld, F. A. Dilmanian, D. N. Slatkin, and H. M. Smilowitz, "Radiotherapy enhancement with gold nanoparticles," *J Pharm Pharmacol*, vol. 60, no. 8, pp. 977–985, 2008.

[17] S. H. Cho, "Estimation of tumour dose enhancement due to gold nanoparticles during typical radiation treatments: A preliminary monte carlo study," *Phys Med Biol*, vol. 50, no. 15, pp. N163–N173, 2005.

[18] K. T. Butterworth, S. J. McMahon, L. E. Taggart, and K. M. Prise, "Radiosensitization by gold nanoparticles: effective at megavoltage energies and potential role of oxidative stress," *Transl Cancer Res*, vol. 2, no. 4, pp. 269–279, 2013.

[19] S. Jain, J. A. Coulter, A. R. Hounsell, K. T. Butterworth, S. J. McMahon, W. B. Hyland, M. F. Muir, G. R. Dickson, K. M. Prise, F. J. Currell, J. M. O'Sullivan, and D. G. Hirst, "Cell-specific radiosensitization by gold nanoparticles at megavoltage radiation energies," *Int J Radiat Oncol Biol Phys*, vol. 79, no. 2, pp. 531–539, 2011.

[20] R. I. Berbeco, H. Korideck, W. Ngwa, R. Kumar, J. Patel, S. Sridhar, S. Johnson, B. D. Price, A. Kimmelman, and G. M. Makrigiorgos, "DNA damage enhancement from gold nanoparticles for clinical mv photon beams," *Radiat Res*, vol. 178, no. 6, pp. 604–608, 2012.

[21] Y. Pan, A. Leifert, D. Ruau, S. Neuss, J. Bornemann, G. Schmid, W. Brandau, U. Simon, and W. Jahnen-Dechent, "Gold nanoparticles of diameter 1.4 nm trigger necrosis by oxidative stress and mitochondrial damage," *Small*, vol. 5, no. 18, pp. 2067–2076, 2009.

[22] J. J. Li, D. Hartano, C.-N. Ong, B.-H. Bay, and L.-Y. L. Yung, "Autophagy and oxidative stress associated with gold nanoparticles," *Biomater*, vol. 31, no. 23, pp. 5996–6003, 2010.

[23] L. Cui, S. Her, G. R. Borst, R. G. Bristow, D. A. Jaffray, and C. Allen, "Radiosensitization by gold nanoparticles: Will they ever make it to the clinic?" *Radiother Oncol*, vol. 124, no. 3, pp. 344–356, 2017.

[24] B. Janic, F. Liu, K. R. Bobbitt, S. L. Brown, I. J. Chetty, G. Mao, B. Movsas, and N. Wen, "Cellular uptake and radio-sensitization effect of small gold nanoparticles in MCF-7 breast cancer cells," *J Nanomed Nanotechnol*, vol. 9, no. 3, p. 499, 2018.

[25] N. Ma, F.-G. Wen, X. Zhang, Y.-W. Jiang, H.-R. Jia, J.-Y. Wang, Y.-H. Li, P. Liu, N. Gu, and Z. Chen, "Shape-dependent radiosensitization effect of gold nanostructures in cancer radiotherapy: Comparison of gold nanoparticles, nanospikes, and nanorods," *ACS Appl Mater Interfaces*, vol. 9, no. 15, pp. 13 037–13 048, 2017.

[26] F. Geng, K. Song, J. Z. Xing, C. Yuan, S. Yan, Q. Yang, J. Chen, and B. Kong, "Thio-glucose bound gold nanoparticles enhance radio-cytotoxic targeting of ovarian cancer," *Nanotechnology*, vol. 22, no. 28, p. 285101, 2011.

[27] X. Zhang, J. Z. Xing, J. Chen, L. Ko, J. Amanie, S. Gulavita, N. Pervez, D. Yee, R. Moore, and W. Roa, "Enhanced radiation sensitivity in prostate cancer by gold-nanoparticles," *Clin Invest Med*, vol. 31, no. 3, pp. E160–E167, 2008.

[28] J. F. Hainfeld, D. N. Slatkin, and H. M. Smilowitz, "The use of gold nanoparticles to enhance radiotherapy in mice," *Phys Med and Biol*, vol. 49, no. 18, pp. N309–15, 2004.

[29] J. F. Hainfeld, F. A. Dilmanian, Z. Zhong, D. N. Slatkin, J. A. Kalef-Ezra, and H. M. Smilowitz, "Gold nanoparticles enhance the radiation therapy of a murine squamous cell carcinoma," *Phys Med Biol*, vol. 55, no. 11, pp. 3045–3059, 2010.

[30] J. F. Hainfeld, H. M. Smilowitz, M. J. O'Connor, F. A. Dilmanian, and D. N. Slatkin, "Gold nanoparticle imaging and radiotherapy of brain tumors in mice," *Nanomed*, vol. 8, no. 10, pp. 1601–1609, 2013.

[31] B. Janic, S. L. Brown, R. Neff, F. Liu, G. Mao, Y. Chen, L. Jackson, I. J. Chetty, B. Movsas, and N. Wen, "Therapeutic enhancement of radiation and immunomodulation by gold nanoparticles in triple negative breast cancer," *Cancer Biol Ther*, vol. 22, no. 2, pp. 124–135, 2021.

[32] F. Geng, J. Z. Xing, J. Chen, R. Yang, Y. Hao, and K. Song, "Pegylated glucose gold nanoparticles for improved in-vivo bio-distribution and enhanced radiotherapy on cervical cancer," *J Biomed Nanotechnol*, vol. 10, no. 7, pp. 1205–1216, 2014.

[33] M.-Y. Chang, A.-L. Shiau, Y.-H. Chen, C.-J. Chang, H. H.-W. Chen, and C.-L. Wu, "Increased apoptotic potential and dose-enhancing effect of gold nanoparticles in combination with single-dose clinical electron beams on tumor-bearing mice," *Cancer Sci*, vol. 99, no. 7, pp. 1479–1484, 2008.

[34] Y. Chen, J. Yang, S. Fu, and J. Wu, "Gold nanoparticles as radiosensitizers in cancer radiotherapy," *Int J Nanomedicine*, vol. 15, pp. 9407–9430, 2020.

[35] L. Strigari, V. Ferrero, G. Visona, F. Dalmasso, A. Gobbato, P. Cerello, S. Visentin, and A. Attili, "Targeted dose enhancement in radiotherapy for breast cancer using gold nanoparticles, part 2: A treatment planning study," *Med Phys*, vol. 44, no. 5, pp. 1993–2001, 2017.

[36] H. R. Baghani and S. Nasrollahi, "Efficacy of various nanoparticle types in dose enhancement during low energy x-ray IORT: A monte carlo simulation study," *Radiat Phys and Chem*, vol. 183, p. 109432, 2021.

[37] Y. Yong, X. Cheng, T. Bao, M. Zu, L. Yan, W. Yin, C. Ge, D. Wang, Z. Gu, and Y. Zhao, "Tungsten sulfide quantum dots as multifunctional nanotheranostics for in vivo dual-modal image-guided photothermal/radiotherapy synergistic therapy," *ACS Nano*, vol. 9, no. 12, pp. 12 451–12 463, 2015.

[38] P. Liu, Z. Huang, Z. Chen, R. Xu, H. Wu, F. Zang, C. Wang, and N. Gu, "Silver nanoparticles: a novel radiation sensitizer for glioma?" *Nanoscale*, vol. 5, no. 23, pp. 11 829–11 836, 2013.

[39] A. F. Bagley, E. B. Ludmir, A. Maitra, B. D. Minsky, G. L. Smith, P. Das, A. C. Koong, E. B. Holliday, C. M. Taniguchi, M. H. G. Katz, E. P. Tamm, R. A. Wolff, M. J. Overman, S. Patel, M. P. Kim, C.-W. D. Tzeng, N. Ikoma, M. S. Bhutani, and E. J. Koay, "NBTXR3, a first-in-class radioenhancer for pancreatic ductal adenocarcinoma: Report of first patient experience," *Clin and Transl Radiat Oncol*, vol. 33, pp. 66–69, 2022.

[40] L. R. Hirsch, R. J. Stafford, J. A. Bankson, S. R. Sershen, B. Rivera, R. E. Price, J. D. Hazle, N. J. Halas, and J. L. West, "Nanoshell-mediated near-infrared thermal therapy of tumors under magnetic resonance guidance," *Proc Natl Acad Sci*, vol. 100, no. 23, pp. 13 549–13 554, 2003.

[41] J. Vines, J.-H. Yoon, N.-E. Ryu, D.-J. Lim, and H. Park, "Gold nanoparticles for photothermal cancer therapy," *Front Chem*, vol. 7, no. 167, 2019.

[42] A. J. Trinidad, S. J. Hong, Q. Peng, S. J. Madsen, and H. Hirschberg, "Combined concurrent photodynamic and gold nanoshell loaded macrophage-mediated photothermal therapies: An in vitro study on squamous cell head and neck carcinoma," *Lasers Surg Med*, vol. 46, no. 4, pp. 310–318, 2014.

[43] S. Jain, D. G. Hirst, and J. M. O'Sullivan, "Gold nanoparticles as novel agents for cancer therapy," *Br J Radiol*, vol. 85, no. 1010, pp. 110–113, 2012.

[44] A. R. Rastinehad, H. Anastos, E. Wajswol, J. S. Winoker, J. P. Sfakianos, S. K. Doppalapudi, M. R. Carrick, C. J. Knauer, B. Taouli, S. C. Lewis, A. K. Tewari, J. A. Schwartz, S. E. Canfield, A. K. George, J. L. West, and N. J. Halas, "Gold nanoshell-localized photothermal ablation of prostate tumors in a clinical pilot device study," *PNAS*, vol. 116, no. 37, pp. 18 590—-18 596, 2019.

[45] R. Ahmad, J. Fu, N. He, and S. Li, "Advanced gold nanomaterials for photothermal therapy of cancer," *J Nanosci Nanotechnol*, vol. 16, no. 1, pp. 67–80, 2016.

[46] R. Weissleder, "A clearer vision for in vivo imaging," *Nat Biotechnol*, vol. 19, no. 4, pp. 316–317, 2001.

[47] J. Kim, S. Park, J. E. Lee, S. M. Jin, J. H. Lee, I. S. Lee, I. Yang, J.-S. Kim, S. K. Kim, M.-H. Cho, and T. Hyeon, "Designed fabrication of multifunctional magnetic gold nanoshells and their application to magnetic resonance imaging and photothermal therapy," *Angew Chem Int Ed Engl*, vol. 45, no. 46, pp. 7754–7758, 2006.

[48] Y. T. Lim, M. Y. Cho, J. K. Kim, S. Hwangbo, and B. H. Chung, "Plasmonic magnetic nanostructure for bimodal imaging and photonic-based therapy of cancer cells," *ChemBioChem*, vol. 8, no. 18, pp. 2204–2209, 2007.

[49] Y. Shao, C. Hao, Y. Guo, J. Song, and F. Song, "Stable hybrid nanocapsules with gold nanorods and cyanine dyes for near-infrared photothermal ablation of subcutaneous tumor," *Adv Therap*, vol. 6, no. 7, p. 2300066, 2023.

[50] W. Lu, C. Xiong, G. Zhang, Q. Huang, R. Zhang, J. Z. Zhang, and C. Li, "Targeted photothermal ablation of murine melanomas with melanocyte-stimulating hormone analog–conjugated hollow gold nanospheres," *Clin Cancer Res*, vol. 15, no. 3, pp. 876–886, 2009.

[51] H. Yuan, C. G. Khoury, C. M. Wilson, G. A. Grant, A. J. Bennett, and T. Vo-Dinh, "In vivo particle tracking and photothermal ablation using plasmon-resonant gold nanostars," *Nanomedicine*, vol. 8, no. 8, pp. 1355–1363, 2012.

[52] J. A. Schwartz, A. M. Shetty, R. E. Price, R. J. Stafford, J. C. Wang, R. K. Uthamanthil, K. Pham, R. J. McNichols, C. L. Coleman, and J. D. Payne, "Feasibility study of particle-assisted laser ablation of brain tumors in orthotopic canine model," *Cancer Res*, vol. 69, no. 4, pp. 1659–1667, 2009.

[53] M. R. K. Ali, I. M. Ibrahim, H. R. Ali, S. A. Selim, and M. A. El-Sayed, "Treatment of natural mammary gland tumors in canines and felines using gold nanorods-assisted plasmonic photothermal therapy to induce tumor apoptosis," *Int J Nanomedicine*, vol. 11, pp. 4849–4863, 2016.

[54] J. Z. Zhang, "Biomedical applications of shape-controlled plasmonic nanostructures: A case study of hollow gold nanospheres for photothermal ablation therapy of cancer," *J Phys Chem Lett*, vol. 1, no. 4, pp. 686–695, 2010.

[55] V. P. Pattani and J. W. Tunnell, "Nanoparticle-mediated photothermal therapy: a comparative study of heating for different particle types," *Lasers Surg Med*, vol. 44, no. 8, pp. 675–684, 2012.

[56] M.-R. Choi, R. Bardhan, K. J. Stanton-Maxey, S. Badve, H. Nakshatri, K. M. Stantz, N. Cao, N. J. Halas, and S. E. Clare, "Delivery of nanoparticles to brain metastases of breast cancer using a cellular trojan horse," *Cancer Nanotechnol*, vol. 3, no. 1-6, pp. 47–54, 2012.

[57] G. Zhang, Z. Wang, W. Lu, R. Zhang, Q. uang, M. Tian, L. Li, D. Liang, and C. Li, "Influence of anchoring ligands and particle size on the colloidal stability and in vivo biodistribution of polyethylene glycol-coated gold nanoparticles in tumor-xenografted mice," *Biomaterials*, vol. 30, no. 10, pp. 1928–1936, 2009.

[58] W.-S. Cho, M. Cho, J. Jeong, M. Choi, B. S. Han, H.-S. Shin, J. Hong, B. H. Chung, J. Jeong, and M.-H. Cho, "Size-dependent tissue kinetics of PEG-coated gold nanoparticles," *Toxicol Appl Pharmacol*, vol. 245, no. 1, pp. 116–123, 2010.

[59] M. Alle, G. Sharma, S.-H. Lee, and J.-C. Kim, "Next-generation engineered nanogold for multimodal cancer therapy and imaging: a clinical perspectives," *J Nanobiotechnology*, vol. 20, p. 222, 2022.

[60] Y. Yang, X. Zheng, L. Chen, X. Gong, H. Yang, X. Duan, and Y. Zhu, "Multifunctional gold nanoparticles in cancer diagnosis and treatment," *Int J Nanomedicine*, vol. 17, pp. 2041–2067, 2022.

[61] L. Shang, X. Zhou, J. Zhang, Y. Shi, and L. Zhong, "Metal nanoparticles for photodynamic therapy: A potential treatment for breast cancer," *Molecules*, vol. 26, no. 21, p. 6532, 2021.

[62] Y. Cheng, A. C. Samia, J. D. Meyers, I. Panagopoulos, B. Fei, and C. Burda, "Highly efficient drug delivery with gold nanoparticle vectors for in vivo photodynamic therapy of cancer," *J Am Chem Soc*, vol. 130, no. 32, pp. 10 643–10 647, 2008.

[63] I. Yoon, J. Z. Li, and Y. S. Shim, "Advance in photosensitizers and light delivery for photodynamic therapy," *Clin Endosc*, vol. 46, no. 1, pp. 7–23, 2013.

[64] D. M. Ozog, A. M. Rkein, S. G. Fabi, M. H. Gold, M. P. Goldman, N. J. Lowe, G. M. Martin, and G. S. Munavalli, "Photodynamic therapy: A clinical consensus guide," *Dermatol Surg*, vol. 42, no. 7, pp. 804–827, 2016.

[65] B. Cline, I. Delahunty, and J. Xie, "Nanoparticles to mediate x-ray-induced photodynamic therapy and Cherenkov radiation photodynamic therapy," *Wiley Interdiscip Rev Nanomed Nanobiotechnol*, vol. 11, no. 2, p. e1541, 2019.

[66] H. E. Townley, J. Kim, and P. J. Dobson, "In vivo demonstration of enhanced radiotherapy using rare earth doped titania nanoparticles," *Nanoscale*, vol. 4, no. 16, pp. 5042–5050, 2012.

[67] P. Liu, W. Yang, L. Shi, H. Zhang, Y. Xu, P. Wang, G. Zhang, W. R. Chen, B. Zhang, and X. Wang, "Concurrent photothermal therapy and photodynamic therapy for cutaneous squamous cell carcinoma by gold nanoclusters under a single NIR laser irradiation," *J Mater Chem B*, vol. 7, no. 44, pp. 6924–6933, 2019.

[68] L. Ma, X. Zou, and W. Chen, "A new x-ray activated nanoparticle photosensitizer for cancer treatment," *J Biomed Nanotechnol*, vol. 10, no. 8, pp. 1501–1508, 2014.

[69] X.-D. Ren, X.-Y. Hao, H.-C. Li, M.-R. Ke, B.-Y. Zheng, and J.-D. Huang, "Progress in the development of nanosensitizers for x-ray-induced photodynamic therapy," *Drug Discov Today*, vol. 23, no. 10, pp. 1791–1800, 2018.

[70] J. Liu, Y. Yang, W. Zhu, X. Yi, Z. Dong, X. Xu, M. Chen, K. Yang, G. Lu, L. Jiang, and Z. Liu, "Nanoscale metal-organic frameworks for combined photodynamic radiation therapy in cancer treatment," *Biomaterials*, vol. 97, pp. 1–9, 2016.

[71] L. He, X. Yu, and W. Li, "Recent progress and trends in x-ray-induced photodynamic therapy with low radition doses," *ACS Nano*, vol. 16, no. 12, pp. 19 691–19 721, 2022.

[72] F. S. Hosseini, N. Naghavi, and A. Sazgarnia, "A physicochemical model of x-ray induced photodynamic therapy (X-PDT) with an emphasis on tissue oxygen concentration and oxygenation," *Sci Rep*, vol. 13, no. 17882, 2023.

[73] V. Chandrakala, V. Aruna, and G. Angajala, "Review on metal nanoparticles as nanocarriers: current challenges and perspectives in drug delivery systems," *Emergent Mater*, vol. 5, no. 6, pp. 1593–1615, 2022.

[74] M. Yafout, A. Ousaid, Y. Khayati, and I. E. Otmani, "Gold nanoparticles as a drug delivery system for standard chemotherapeutics: A new lead for targeted pharmacological cancer treatments," *Sci Afr*, vol. 11, p. e00685, 2021.

[75] F.-Y. Kong, J.-W. Zhang, R.-F. Li, Z.-X. Wang, W.-J. Wang, and W. Wang, "Unique roles of gold nanoparticles in drug delivery, targeting and imaging applications," *Molecules*, vol. 22, no. 9, p. 1445, 2017.

[76] S. Siddique and J. C. L. Chow, "Gold nanoparticles for drug delivery and cancer therapy," *Appl Sci*, vol. 10, no. 11, p. 3824, 2020.

[77] K. Banerjee, V. R. Ravishankar, and M. Umashankar, "Effect of peptide-conjugated nanoparticles on cell lines," *Prog Biomater*, vol. 8, no. 1, pp. 11–21, 2019.

[78] B. S. Raghavan, S. Kondath, R. Anantanarayanan, and R. Rajaram, "Kaempferol mediated synthesis of gold nanoparticles and their cytotoxic effects on MCF-7 cancer cell line," *Process Biochem*, vol. 50, no. 11, pp. 1966–1976, 2015.

[79] G. F. Paciotti, L. Myer, D. Weinreich, D. Goia, N. Pavel, R. E. McLaughlin, and L. Tamarkin, "Colloidal gold: A novel nanoparticle vector for tumor directed drug delivery," *Drug Deliv*, vol. 11, no. 3, pp. 169–183, 2004.

[80] S. K. Libutti, G. F. Paciotti, A. A. Byrnes, H. R. A. Jr, W. E. Gannon, M. Walker, G. D. Seidel, N. Yuldasheva, and L. Tamarkin, "Phase I and pharmacokinetic studies of CYT-6091, a novel PEGylated colloidal gold-rhTNF nanomedicine," *Clin Cancer Res*, vol. 16, no. 24, pp. 6139–49, 2010.

[81] R. Zhang, F. Kiessling, T. Lammers, and R. M. Pallares, "Clinical translation of gold nanoparticles," *Drug Deliv Transl Res*, vol. 13, no. 2, pp. 378–385, 2023.

[82] A. M. Alkilany and C. J. Murphy, "Toxicity and cellular uptake of gold nanoparticles: what we have learned so far?" *J Nanopart Res*, vol. 12, no. 7, pp. 2313–2333, 2010.

[83] C. G. England, A. M. Gobin, and H. B. Frieboes, "Evaluation of uptake and distribution of gold nanoparticles in solid tumors," *Eur Phys J Plus*, vol. 130, no. 11, 2015.

[84] X.-D. Zhang, D. Wu, X. Shen, J. chen, Y.-M. Sun, P.-X. Liu, and X.-J. Liang, "Size-dependent radiosensitization of PEG-coated gold nanoparticles for cancer radiation therapy," *Biomaterials*, vol. 33, no. 27, pp. 6408–6419, 2012.

[85] S. Clement, W. Chen, A. G. Anwer, and E. M. Goldys, "Verteprofin conjugated to gold nanoparticles for fluorescent cellular bioimaging and x-ray mediated photodynamic therapy," *Microchim Acta*, vol. 184, pp. 1765–1771, 2017.

[86] J. M. Bergen, H. A. von Recum, T. T. Goodman, A. P. Massay, and S. H. Pun, "Gold nanoparticles as a versatile platform for optimizing physicochemical parameters for targeted drug delivery," *Marco-molecular Bioscience*, vol. 6, no. 7, pp. 506–516, 2006.

[87] X.-D. Zhang, D. Wu, X. Shen, P.-X. Liu, F.-Y. Fan, and S.-J. Fan, "*In vivo* renal clearance, biodistribution, toxicity of gold nanoclusters," *Biomaterials*, vol. 33, no. 18, pp. 4628–4638, 2012.

[88] S. Lal, S. E. Clare, and N. J. Halas, "Nanoshell-enabled photothermal cancer therapy: Impending clinical impact," *Acc Chem Res*, vol. 41, no. 12, pp. 1842–1851, 2008.

[89] S. Fraga, A. Brandao, M. E. Soares, T. Morais, J. A. Duarte, L. Pereira, L. Soares, C. Neves, E. Pereira, M. de Lourdes Bastos, and H. Carmo, "Short- and long-term distribution and toxicity of gold nanoparticles in the rat after a single-dose intravenous administration," *Nanomedicine*, vol. 10, no. 8, pp. 1757–1766, 2014.

[90] Y. Chen and X. Feng, "Gold nanoparticles for skin drug delivery," *Int J Pharm*, vol. 625, p. 122122, 2022.

[91] M. A. Safwat, G. M. Soliman, D. Sayed, and M. A. Attia, "Fluorouracil-loaded gold nanoparticles for the treatment of skin cancer: Development, in vitro characterization, and in vivo evaluation in a mouse skin cancer xenograft model," *Mol Pharm*, vol. 15, no. 6, pp. 2194–2205, 2018.

[92] N. Khlebtsov and L. Dykmana, "Biodistribution and toxicity of engineered gold nanoparticles: A review of in vitro and in vivo studies," *Chem Soc Rev*, vol. 40, no. 3, pp. 1647–1671, 2011.

[93] J. F. Hainfeld, M. J. O'Connor, P. Lin, L. Qian, D. N. Slatkin, and H. M. Smilowitz, "Infrared-transparent gold nanoparticles converted by tumors to infrared absorbers cure tumors in mice by photothermal therapy," *PLoS One*, vol. 9, no. 2, p. e88414, 2014.

[94] W. G. Connor, E. W. Gerner, R. C. Miller, and M. L. Boone, "Prospects for hyperthermia in human cancer therapy. part II: implications of biological and physical data for applications of hyperthermia to man," *Radiology*, vol. 123, no. 2, pp. 497–503, 1977.

[95] N. Manohar, F. J. Reynoso, P. Diagaradjane, S. Krishnan, and S. H. Cho, "Quantitative imaging of gold nanoparticle distribution in a tumor-bearing mouse using benchtop x-ray fluorescence computed tomography," *Sci Rep*, vol. 6, no. 1, pp. 1–10, 2016.

[96] T. Niidome, M. Yamagata, Y. Okamoto, Y. Akiyama, H. Takahashi, T. Kawano, Y. Katayama, and Y. Niidome, "PEG-modified gold nanorods with a stealth character for in vivo applications," *Journal of Controlled Release*, vol. 114, no. 3, pp. 343–347, 2006.

[97] Y. Wu, M. R. K. Ali, K. Chen, N. Fang, and M. A. El-Sayed, "Gold nanoparticles in biological optical imaging," *Nano Today*, vol. 24, pp. 120–140, 2019.

[98] L. V. Wang and S. Hu, "Photoacoustic tomography: In vivo imaging from organelles to organs," *Science*, vol. 335, no. 6075, pp. 1458–1462, 2012.

[99] J. F. Hainfeld, M. J. O'Connor, F. A. Dilmanian, D. N. Slatkin, D. J. Adams, and H. M. Smilowitz, "Micro-CT enables microlocalisation and quantification of Her2-targeted gold nanoparticles within tumour regions," *Br J Radiol*, vol. 84, no. 1002, pp. 526–533, 2011.

[100] D. P. Cormode, S. Si-Mohamed, D. Bar-Ness, M. Sigovan, P. C. Naha, J. Balegamire, F. Lavenne, P. Coulon, E. Roessl, M. Bartels, M. Rokni, I. Blevis, L. Boussel, and P. Douek, "Multicolor spectral photon-counting computed tomography: in vivo dual contrast imaging with a high count rate scanner," *Sci Rep*, vol. 7, no. 4784, 2017.

[101] S.-K. Cheong, B. L. Jones, A. K. Siddiqi, F. Liu, N. Manohar, and S. H. Cho, "X-ray fluorescence computed tomography (XFCT) imaging of gold nanoparticle-loaded objects using 110 kVp x-rays," *Phys Med Biol*, vol. 55, no. 3, pp. 647–662, 2010.

[102] Y. Kuang, G. Pratx, M. Bazalova, J. Qian, B. Meng, and L. Xing, "Development of XFCT imaging strategy for monitoring the spatial distribution of platinum-based chemodrugs: Instrumentation and phantom validation," *Med Phys*, vol. 40, no. 3, p. 030701, 2013.

[103] Y. Kuang, G. Pratx, M. Bazalova, B. Meng, J. Qian, and L. Xing, "First demonstration of multiplexed X-ray fluorescence computed tomography (XFCT) imaging," *IEEE Trans Med maging*, vol. 32, no. 2, pp. 262–267, 2013.

[104] T. Sasaya, N. Sunaguchi, T-Thet-Lwin, K. Hyodo, T. Zeniya, T. Takeda, and T. Yuasa, "Dual-energy fluorescent x-ray computed tomography system with a pinhole design: Use of K-edge discontinuity for scatter correction," *Sci Rep*, vol. 7, no. 44143, 2017.

[105] B. Deng, G. Du, G. Zhou, Y. Wang, Y. Ren, R. Chen, P. Sun, H. Xie, and T. Xiao, "3D elemental sensitive imaging by full-field XFCT," *Analyst*, vol. 140, no. 10, pp. 3521–3525, 2015.

[106] T. Takeda, Q. Yu, T. Yashiro, T. Yuasa, Y. Hasegawa, Y. Itai, and T. Akatsuka, "Human thyroid specimen imaging by fluorescent x-ray computed tomography with synchrotron radiation," *Proc SPIE*, vol. 3772, pp. 258–267, 1999.

[107] M. Bazalova, Y. Kuang, G. Pratx, and L. Xing, "Investigation of X-ray fluorescence computed tomography (XFCT) and K-edge imaging," *IEEE Trans Med Imaging*, vol. 31, no. 8, pp. 1620–7, 2012.

[108] L. J. Meng, N. Li, and P. J. La Rivière, "X-ray fluorescence emission tomography (XFET) with novel imaging geometries – a Monte Carlo study," *IEEE Trans Nucl Sci*, vol. 58, no. 6, pp. 3359–3369, 2011.

[109] M. Ahmad, M. Bazalova-Carter, R. Fahrig, and L. Xing, "Optimized detector angular configuration increases the sensitivity of x-ray fluorescence computed tomography (XFCT)," *IEEE Trans Med Imaging*, vol. 34, no. 5, pp. 1140–1147, 2015.

[110] C. A. S. Dunning and M. Bazalova-Carter, "Optimization of a table-top x-ray fluorescence computed tomography (XFCT) system," *Phys Med Biol*, vol. 63, no. 23, p. 235013, 2018.

[111] B. L. Jones and S. H. Cho, "The feasibility of polychromatic cone-beam x-ray fluorescence computed tomography (XFCT imaging of gold nanoparticle-loaded objects: a Monte Carlo study," *Phys Med Biol*, vol. 56, no. 12, pp. 3719–3730, 2011.

[112] B. L. Jones, N. Manohar, F. Reynoso, A. Karellas, and S. H. Cho, "Experimental demonstration of benchtop x-ray fluorescence computed tomography (XFCT) of gold nanoparticle-loaded objects using lead- and tin-filtered polychromatic cone-beams," *Phys Med Biol*, vol. 57, no. 23, pp. N457–N467, 2012.

[113] N. Manohar, F. J. Reynoso, and S. H. Cho, "Technical note: A benchtop cone-beam x-ray fluorescence computed tomography (XFCT) system with a high-power x-ray source and transmission CT imaging capability," *Med Phys*, vol. 45, no. 10, pp. 4652–4659, 2018.

[114] L. Li, S. Zhang, W. Zhang, and H. Lu, "Full-field *in vivo* imaging of nanoparticles using benchtop cone-beam XFCT system with pixelated photon counting detector," *Phys Med Biol*, vol. 68, no. 3, 2023.

[115] C. A. S. Dunning and M. Bazalova-Carter, "Sheet beam x-ray fluorescence computed tomography (XFCT) imaging of gold nanoparticles," *Med Phys*, vol. 45, no. 6, pp. 2572–2582, 2018.

[116] S. Jung, W. Sung, and S.-J. Ye, "Pinhole X-ray fluorescence imaging of gadolinium and gold nanoparticles using polychromatic X-rays: a Monte Carlo study," *Int J Nanomedicine*, vol. 12, pp. 5805–5817, 2017.

[117] L. Deng, B. Wei, P. He, Y. Zhang, and P. Feng, "A Geant4-based Monte Carlo study of a benchtop multi-pinhole X-ray fluorescence computed tomography imaging," *Int J Nanomedicine*, vol. 13, pp. 7207–7216, 2018.

[118] N. Manohar, F. J. Reynoso, and S. H. Cho, "Experimental demonstration of direct L-shell x-ray fluorescence imaging of gold nanoparticles using a benchtop x-ray source," *Med Phys*, vol. 40, no. 8, p. 080702, 2013.

[119] S. Zhang, L. Li, J. Chen, Z. Chen, W. Zhang, and H. Lu, "Quantitative imaging of Gd nanoparticles in mice using benchtop cone-beam X-ray fluorescence computed tomography system," *Int J Mol Sci*, vol. 20, no. 9, p. 2315, 2019.

[120] M. Ahmad, M. Bazalova, L. Xiang, and L. Xing, "Order of magnitude sensitivity increase in x-ray fluorescence computed tomography (XFCT) imaging with an optimized spectro-spatial detector configuration: Theory and simulation," *IEEE Trans Med Imaging*, vol. 33, no. 5, pp. 1119–1128, 2014.

[121] A. Rose, *Vision: human and electronic*. Plenum Press, New York, 1973.

[122] G. Fu, L. J. Meng, P. Eng, M. Newville, P. Vargas, and P. J. La Rivière, "Experimental demonstration of novel imaging geometries for x-ray fluorescence computed tomography," *Med Phys*, vol. 40, no. 6, p. 061903, 2013.

[123] A. Groll, J. George, P. Vargas, P. J. La Rivière, and L. J. Meng, "Element mapping in organic samples utilizing a benchtop x-ray fluorescence emission tomography (XFET) system," *IEEE Trans Nucl Sci*, vol. 62, no. 5, pp. 2310–2317, 2015.

[124] S. Mandot, E. M. Zannoni, L. Cai, X. Nie, P. J. La Rivière, M. D. Wilson, and L. J. Meng, "A high-sensitivity benchtop x-ray fluorescence emission tomography (XFET) system with a full-ring of x-ray imaging-spectrometers and a compound-eye collimation aperture," *IEEE Trans Med Imaging*, 2024.

[125] P. J. La Rivière, "Approximate analytic reconstruction in x-ray fluorescence computed tomography," *Phys Med Biol*, vol. 49, no. 11, pp. 2391–2405, 2004.

[126] Z. W. Di, S. Leyffer, and S. M. Wild, "Optimization-based approach for joint x-ray fluorescence and transmission tomographic inversion," *SIAM J Imaging Sci*, vol. 9, no. 1, pp. 1–23, 2016.

[127] C. G. Schroer, "Reconstructing x-ray fluorescence microtomograms," *Appl Phys Lett*, vol. 79, no. 12, pp. 1912–1914, 2001.

[128] B. Golosio, A. Simionovici, A. Somogyi, L. Lemelle, M. Chukalina, and A. Brunetti, "Internal elemental microanalysis combining x-ray fluorescence, compton and transmission tomography," *J Appl Phys*, vol. 94, no. 1, pp. 145–156, 2003.

[129] P. J. La Rivière and P. A. Vargas, "Monotonic penalized-likelihood image reconstruction for x-ray fluorescence computed tomography," *IEEE Trans Med Imaging*, vol. 25, no. 9, pp. 1117–1129, 2006.

[130] P. J. La Rivière, D. M. Billmire, P. Vargas, M. Rivers, and S. R. Sutton, "Penalized-likelihood image reconstruction for x-ray fluorescence computed tomography," *Optical Engineering*, vol. 45, no. 7, p. 077005, 2006.

[131] P. J. La Rivière and P. Vargas, "Alternating update penalized-likelihood image reconstruction for x-ray fluorescence computed tomography," *Proc SPIE*, vol. 6318, p. 63180Z, 2006.

[132] J. Shi, B. Granger, K. Xu, and Y. Yang, "Quantitative x-ray fluorescence imaging of gold nanoparticles using joint L1 and total variation regularized reconstruction," *Quant Imaging Med Surg*, vol. 10, no. 1, pp. 184–196, 2020.

[133] M. Defrise, A. Rezaei, and J. Nuyts, "Time-of-flight PET data determine the attenuation sinogram up to a constant," *Phys Med Biol*, vol. 57, no. 4, pp. 885–899, 2012.

[134] A. V. Bronnikov, "Approximate reconstruction of attenuation map in SPECT imaging," *IEEE Trans Nucl Sci*, vol. 42, no. 5, pp. 1483–1488, 1995.

[135] Y. Censor, D. E. Gustafson, A. Lent, and H. Tuy, "A new approach to the emission computerized tomography problem: simultaneous calculation of attenuation and activity coefficients," *IEEE Trans Nucl Sci*, vol. NS-26, no. 2, pp. 2775–2779, 1979.

[136] J. Nuyts, P. Dupont, S. Stroobants, R. Benninck, L. Mortelmans, and P. Suetens, "Simultaneous maximum a posteriori reconstruction of attenuation and activity distributions from emission sinograms," *IEEE Trans Med Imaging*, vol. 18, no. 5, pp. 393–403, 1999.

[137] A. Rezaei, M. Defrise, G. Bal, C. Michel, M. Conti, C. Watson, and J. Nuyts, "Simultaneous reconstruction of activity and attenuation in time-of-flight PET," *IEEE Trans Med Imaging*, vol. 31, no. 12, pp. 2375–2382, 2012.

[138] F. Natterer, "Determination of tissue attenuation in emission tomography of optically dense media," *Inverse Probl*, vol. 9, no. 6, pp. 731–736, 1993.

[139] A. Welch, R. Clack, F. Natterer, and G. T. Gullberg, "Toward accurate attenuation correction in SPECT without transmission measurements," *IEEE Trans Med Imaging*, vol. 16, no. 5, pp. 532–541, 1997.

[140] Y. Yan and G. L. Zeng, "Attenuation map estimation with SPECT emission data only," *Int J Imaging Syst Technol*, vol. 19, no. 3, pp. 271–276, 2009.

[141] E. X. Miqueles and A. R. D. Pierro, "Iterative reconstruction in x-ray fluorescence tomography based on Radon inversion," *IEEE Trans Med Imaging*, vol. 30, no. 2, pp. 438–450, 2011.

[142] Y. Berker, F. Keissling, and V. Schulz, "Scattered PET data for attenuation-map reconstruction in PET/MRI," *Med Phys*, vol. 41, no. 10, p. 102502, 2014.

[143] L. Brusaferri, A. Bousse, E. C. Emond, R. Brown, Y.-J. Tsai, D. Atkinson, S. Ourselin, C. C. Watson, B. F. Hutton, S. Arridge, and K. Theilemans, "Joint activity and attenuation reconstruction from multiple energy window data with photopeak scatter re-estimation in non-TOF 3-D PET," *IEEE Trans Radiat Plasma Med Sci*, vol. 4, no. 4, pp. 410–421, 2020.

[144] S. Ahn, L. Cheng, D. D. Shanbhag, H. Qian, S. S. Kaushik, F. P. Jansen, and F. Wiesinger, "Joint estimation of activity and attenuation for PET using pragmatic MR-based prior: application to clinical TOF PET/MR whole-body data for FDG and non-FDG tracers," *Phys Med Biol*, vol. 63, no. 4, pp. 1–16, 2018.

[145] V. Y. Panin, M. Aykac, and M. E. Casey, "Simultaneous reconstruction of emission activity and attenuation coefficient distribution from TOF data, acquired with external transmission source," *Phys Med Biol*, vol. 58, no. 11, pp. 3649–3669, 2013.

[146] M. J. Berger, J. H. Hubbell, S. M. Seltzer, J. Chang, J. S. Coursey, R. Sukumar, D. S. Zucker, and K. Olsen, "XCOM: Photon cross section database (version 1.5)," http://physics.nist.gov/xcom, 2010, National Institute of Standards and Technology.

[147] J. H. Hubbell, "Photon cross sections, attenuation coefficients, and energy absorption coefficients from 10 keV to 100 GeV," 1969, National Standard Reference Data System.

[148] A. Thompson, D. Attwood, E. Gullikson, M. Howells, K.-J. Kim, J. Kirz, J. Kortright, I. Lindau, Y. Liu, P. Pianetta, A. Robinson, J. Scofield, J. Underwood, G. Williams, and H. Winick, "X-ray data booklet (third edition)," 2009, Center for X-Ray Optics and Advanced Light Source, Lawrence Berkeley National Laboratory.

[149] H. DeBrosse, T. Chandler, L. J. Meng, and P. La Rivière, "Joint estimation of metal density and attenuation maps with pencil beam XFET," *IEEE Trans Radiat Plasma Med Sci*, vol. 7, no. 2, pp. 191–202, 2023.

[150] T. B. Neilsen, D. F. V. Komen, M. K. Transtrum, M. B. Allen, and D. P. Knobles, "Optimal experimental design for machine learning using the Fisher information," *Proc Meet Acoust*, vol. 35, no. 1, 2018.

[151] S. Nordebo, R. Bayford, B. Bengtsson, A. Fhager, M. Gustafsson, R. Hashemzadeh, B. Nilsson, T. Rylander, and R. Sjoden, "An adjoint field approach to Fisher information-based sensitivity analysis in electrical impedence tomography," *Inverse Probl*, vol. 26, no. 12, p. 125008, 2010.

[152] M. D. Collins and L. Fishman, "Efficient navigation of parameter landscapes," *J Acoust Soc Am*, vol. 98, no. 3, pp. 1637–1644, 1995.

[153] T. B. Neilsen, "An iterative implementation of rotated coordinates for inverse problems," *J Acoust Soc Am*, vol. 113, no. 5, pp. 2574–2586, 2003.

[154] R. L. Siddon, "Fast calculation of the exact radiological path for a three-dimensional CT array," *Med Phys*, vol. 12, no. 2, pp. 252–255, 1985.

[155] P. J. La Rivière, "Penalized-likelihood sinogram smoothing for low-dose CT," *Med Phys*, vol. 32, no. 6, pp. 1676–1683, 2005.

[156] H. DeBrosse, L. J. Meng, and P. La Rivière, "Effect of detector placement on joint estimation in x-ray fluorescence emission tomography," *IEEE Trans Radiat Plasma Med Sci*, vol. 8, no. 1, pp. 21–32, 2024.

[157] M. C. Veale, P. Sellar, M. Wilson, and E. Liotti, "HEXITEC: A high-energy X-ray spectroscopic imaging detector for synchrotron applications," *Synchrotoron Radiat News*, vol. 31, no. 6, pp. 28–32, 2018.

[158] P. J. La Rivière, P. A. Vargas, D. Xia, and X. Pan, "Region of interest imaging in x-ray fluorescence computed tomography," *IEEE Trans Nucl Sci*, vol. 57, pp. 234–241, 2010.

[159] P. Feng, W.Cong, B. Wei, and G. Wang, "Analytic comparison between X-ray fluorescence CT and K-edge CT," *IEEE Trans Biomed Eng*, vol. 61, no. 3, pp. 975–985, 2014.

[160] P. J. La Rivière, P. A. Vargas, M. Newville, and S. Sutton, "Reduced-scan schemes for x-ray fluorescence computed tomography," *IEEE Trans Nucl Sci*, vol. 54, pp. 1535–1542, 2007.

[161] H. DeBrosse, G. Jadick, L. J. Meng, and P. La Rivière, "Comparing x-ray fluorescence emission tomography and computed tomography: contrast-to-noise ratios in a numerical mouse phantom," *Proc SPIE*, vol. 12930, pp. 269–276, 2024.

[162] W. P. Segars and B. M. W. Tsui, "MCAT to XCAT: The evolution of 4-D computerized phantoms for imaging research," *Proc IEEE Inst Electr Electron Eng*, vol. 97, no. 12, pp. 1954–1968, 2009.

[163] J. Perl, J. Shin, B. Faddegon, and H. Paganetti, "TOPAS: an innovative proton Monte Carlo platform for research and clinical applications," *Med Phys*, vol. 39, no. 11, pp. 6818–6837, 2012.

[164] J. A. Meganck and B. Liu, "Dosimetry in micro-computed tomography: a review of the measurement methods, impacts, and characterization of the quantum GX imaging system," *Mol Imaging Biol*, vol. 19, no. 4, pp. 499–511, 2017.

[165] J. Zhao, X. Hu, J. Zou, and X. Hu, "Geometric parameters estimation and calibration in cone-beam micro-CT," *Sensors (Basel)*, vol. 15, no. 9, pp. 22 811–25, 2015.

[166] C. Badea, L. W. Hedlund, and G. A. Johnson, "Micro-CT with respiratory and cardiac gating," *Med Phys*, vol. 31, no. 12, pp. 3324–3329, 2004.

[167] C. T. Badea, S. Johnston, B. Johnson, M. Lin, L. W. Hedlund, and G. A. Johnson, "A dual micro-CT system for small animal imaging," *Proc SPIE*, vol. 6913, p. 691342, 2008.

[168] D. W. Holdsworth and M. M. Thornton, "Micro-CT in small animal and specimen imaging," *Trends Biotechnol*, vol. 20, no. 8, pp. S34–S39, 2002.

[169] J. Hsieh, *Computed tomography: principles, design, artifacts, and recent advances*. SPIE press, 2022, vol. 4.

[170] M. U. Ghani, Z. Zhou, L. Ren, Y. Li, B. Zheng, K. Yang, and H. Liu, "Investigation of spatial resolution characteristics of an in vivo micro computed tomography system," *Nucl Instrum Methods Phys Res A*, vol. 807, 2016.

[171] C. A. S. Dunning, D. Richtsmeier, P.-A. Rodesch, K. Iniewski, and M. Bazalova-Carter, "K-edge imaging in spectral photon-counting computed tomography: A benchtop system study," in *Photon Counting Computed Tomography*. Cham Springer, 2023, pp. 247–263.

[172] G. Tortora, L. Gemini, I. D'Iglio, L. Ugga, G. Spadarella, and R. Cuoloco, "Spectral photon-counting computed tomography: A review on technical principles and clinical applications," *J Imaging*, vol. 8, no. 4, p. 112, 2022.

[173] M. Danielsson, M. Persson, and M. Sjolin, "Photon-counting x-ray detectors for CT," *Phys Med Biol*, vol. 66, p. 03TR01, 2021.

[174] M. Bhattarai, S. Bache, E. Abadi, and E. Samei, "Exploration of the pulse pileup effects in a clinical CdTe-based photon-counting computed tomography," *Med Phys*, vol. 50, 2023.

[175] K. Taguchi, E. C. Frey, and X. Wang, "An analytical model of the effects of pulse pileup on the energy spectrum recorded by energy resolved photon counting x-ray detectors," *Med Phys*, vol. 37, no. 8, 2010.

[176] S. Si-Mohamed, D. Bar-Ness, M. Sigovan, V. Tatard-Leitman, D. P. Cormode, P. C. Naha, P. Coulon, L. Rascle, E. Roessl, M. Rokni, A. Altman, Y. Yagil, L. Boussel, and P. Douek, "Multicolour imaging with spectral photon-counting ct: a phantom study," *Eur Radiol Exp*, vol. 2, no. 34, 2018.

[177] P. Lecoq, C. Morel, J. O. Prior, D. Visvikis, S. Gundacker, E. Auffray, P. Križan, R. M. Turtos, D. Thers, and E. Charbon, "Roadmap toward the 10 ps time-of-flight PET challenge," *Phys Med Biol*, vol. 65, no. 21, p. 21RM01, 2020.

[178] D. R. Schaart, S. Ziegler, and H. Zaidi, "Achieving 10 ps coincidence time resolution in TOF-PET is an impossible dream," *Med Phys*, vol. 47, no. 7, pp. 2721–2724, 2020.

[179] S. I. Kwon, R. Ota, E. Berg, F. Hashimoto, K. Nakajima, I. Ogawa, Y. Tamagawa, T. Omura, T. Hasegawa, and S. R. Cherry, "Ultrafast timing enables reconstruction-free positron emission imaging," *Nat Photonics*, vol. 15, no. 12, pp. 914–918, 2021.

[180] A. Pierro, "On the relation between the ISRA and the EM algorithm for positron emission tomography," *IEEE Trans Med Imaging*, vol. 12, no. 2, pp. 328–333, 1993.

[181] Q. Fang, P. M. Meaney, and K. D. Paulsen, "Singular value analysis of the Jacobian matrix in microwave image reconstruction," *IEEE Trans Antennas Propag*, vol. 54, no. 8, pp. 2371–2380, 2006.

[182] V. Ferrero, G. Visona, F. Dalmasso, A. Gobbato, P. Cerello, L. Strigari, S. Visentin, and A. Attili, "Targeted dose enhancement in radiotherapy for breast cancer using gold nanoparticles, part 1: A radiobiological model study," *Med Phys*, vol. 44, no. 5, pp. 1983–1992, 2017.

[183] S. K. Carlson, K. L. Classic, C. E. Bender, and S. J. Russell, "Small animal absorbed radiation dose from serial micro-computed tomography imaging," *Mol Imaging Biol*, vol. 9, no. 2, pp. 78–82, 2007.

[184] H. S. Han and K. Y. Choi, "Advances in nanomaterial-mediated photothermal cancer therapies: Toward clinical applications," *Biomedicines*, vol. 9, no. 3, p. 305, 2021.

[185] W. Chen and J. Zhang, "Using nanoparticles to enable simultaneous radiation and photodynamic therapies for cancer treatment," *J Nanosci Nanotechnol*, vol. 6, no. 4, pp. 1159–1166, 2006.

[186] S. Y. Chun, K. Y. Kim, J. S. Lee, and J. A. Fessler, "Joint estimation of activity distribution and attenuation map for TOF-PET using alternating direction method of multiplier," *Proceedings of IEEE ISBI*, 2016.